

UCLA

UCLA Electronic Theses and Dissertations

Title

Multimodal sensory contributions to hippocampal spatiotemporal selectivity

Permalink

<https://escholarship.org/uc/item/94s3s84c>

Author

Willers, Bernard

Publication Date

2013

Peer reviewed|Thesis/dissertation

UNIVERSITY OF CALIFORNIA
Los Angeles

**Multimodal sensory contributions to hippocampal
spatiotemporal selectivity**

A dissertation submitted in partial satisfaction
of the requirements for the degree
Doctor of Philosophy in Physics

by

Bernard Willers

2013

© Copyright by
Bernard Willers
2013

ABSTRACT OF THE DISSERTATION

**Multimodal sensory contributions to hippocampal
spatiotemporal selectivity**

by

Bernard Willers

Doctor of Philosophy in Physics

University of California, Los Angeles, 2013

Professor Mayank Mehta, Co-chair

Professor Katsushi Arisaka, Co-chair

The hippocampal cognitive map is thought to be driven primarily by distal visual cues and self-motion cues, although other sensory cues have also been demonstrated to influence place cells. Performing controlled experiments exploring the precise role played by different sensory modalities in determining spatial representation in the hippocampus is challenging due to need to control non-specific stimuli such as scent cues and acoustic reflections.

To overcome these challenges we have developed an immersive virtual reality system for rats, in which any spatial information in these non-specific sensory cues are eliminated. The system combines full field of view visual stimuli with spatially accurate auditory stimuli to enable a variety of complex spatial tasks. To eliminate much of the subjectivity in identifying single units in extracellular recording, an improved automated spike sorting method was developed based on existing gaussian mixture approaches.

These tools were then applied to determine whether visual cues alone are sufficient for standard place cell activity in the CA1 region of the hippocampus. Single unit activity was recorded both in virtual reality, where only visual cues and non-vestibular self-motion cues provided spatial information, and in the real world using a linear track experimental paradigm.

Place cells displayed robust spatial selectivity in virtual reality, but only 20% of putative pyramidal cells were active in virtual reality, compared with 45% in the real world task. Distal visual and nonvestibular self-motion cues are thus sufficient to provide spatial selectivity, but vestibular and other sensory cues present in the real world are necessary to fully activate the place cell population. While bidirectional cells preferentially encode absolute position in the real world, they exhibited a distance coding scheme in virtual reality, suggesting that other sensory cues such as scent marks are necessary for a robust bidirectional position code.

The frequency of hippocampal theta oscillations was reduced in virtual reality, and its speed dependence abolished. Despite this, phase precession of place fields was essentially identical in the two environments. These results constrain mechanisms governing both hippocampal theta oscillations and the temporal code. Taken together, these results reveal cooperative and competitive interactions between sensory modalities for control over hippocampal spatiotemporal selectivity and theta rhythm.

The dissertation of Bernard Willers is approved.

Tom Otis

Alex Levine

Katsushi Arisaka, Committee Co-chair

Mayank Mehta, Committee Co-chair

University of California, Los Angeles

2013

TABLE OF CONTENTS

1	Introduction	1
1.1	Measuring neural activity	1
1.2	Spatial representation in the hippocampus	4
1.2.1	The hippocampus	4
1.2.2	The hippocampal rate code	5
1.2.3	The hippocampal temporal code	6
1.2.4	Sensory inputs and place fields	8
1.3	Outline	8
2	Spike sorting	10
2.1	Detection	10
2.2	Waveform extraction	13
2.3	Dimensionality reduction and feature extraction	14
2.4	Clustering	17
2.4.1	Cluster metrics	17
2.4.2	Clustering algorithms	20
2.4.3	Manual clustering	23
2.4.4	Electrode drift	26
2.5	Unit classification	27
3	Virtual reality for rats	30
3.1	Introduction	30
3.1.1	Motivation	30

3.1.2	Sensory capabilities of the rat	32
3.1.3	System requirements	35
3.2	System design	36
3.2.1	Overview	36
3.2.2	Motion tracking	37
3.2.3	Visual stimuli	38
3.2.4	Auditory stimuli	40
3.2.5	Reward checking and delivery	42
3.2.6	Control software	44
3.3	Virtual environments	45
3.3.1	Audio-visual beacon orientation	46
3.3.2	Random foraging task	46
3.3.3	Linear track	47
3.3.4	Two dimensional beacon navigation	49
3.3.5	Spatial navigation task	51
3.3.6	Foraging in spherical geometry	54
3.3.7	Strobed linear navigation	54
4	Place cells on the virtual linear track	56
4.1	Introduction	56
4.2	Methods	57
4.2.1	Real and virtual environments	57
4.2.2	Subjects and training	58
4.2.3	Surgery and electrophysiology	60
4.3	Quantifying selective activity	61

4.3.1	Rate maps	61
4.3.2	Place fields	63
4.4	Properties of the rate code	64
4.4.1	Selective hippocampal activation in VR	64
4.4.2	Stability	66
4.4.3	Spatial selectivity and information content	68
4.4.4	Directional firing	70
4.4.5	Bidirectional activity: the disto code	72
4.5	Properties of the temporal code	79
4.5.1	Reduction in theta frequency does not alter phase precession	79
4.5.2	Reduction in spiking frequency	81
4.5.3	Time dependent frequency estimation	82
4.5.4	Speed dependence of LFP theta rhythm	84
4.5.5	Speed dependent interneuron spike frequency	84
4.6	The role of passive scene rotation	87
4.6.1	Different environments hypothesis	87
4.6.2	Rotation triggered population vector analysis	89
4.6.3	Active turn control experiment	91
4.7	Same cell comparisons	93
5	Conclusion	97
5.1	Summary and discussion	97
5.2	Future work	101
	References	103

LIST OF FIGURES

1.1	A nichrome tetrode probe	3
1.2	Micro-drive design	4
2.1	Sample unfiltered extracellular recording	11
2.2	Sample filtered extracellular recording	12
2.3	Non-linear energy operator as a spike detector.	13
2.4	Sample extracellular spike waveforms	14
2.5	Sample spike peak amplitude projections	15
2.6	Eigen vectors of spike waveform covariance matrix	16
2.7	Complex spike burst	19
2.8	Sample output from automated clustering algorithm	22
2.9	PyClust software package	24
2.10	PyClust automatic boundary creation	26
2.11	Electrode drift	27
2.12	Unit classification	28
3.1	Schematic of the virtual reality system	37
3.2	Cube mapping virtual environment	39
3.3	Calculating vertex texture coordinates	40
3.4	Projection distortion and mirror system	41
3.5	Junction potential based reward checking detection	43
3.6	Random foraging task	48
3.7	Linear track task	49
3.8	Two dimensional audiovisual beacon navigation task	50

3.9	Spatial navigation task with audiovisual cues	51
3.10	Spatial navigation task with only visual or auditory cues	53
3.11	Trajectories in a spherical environment	54
4.1	The virtual linear track	57
4.2	Behavior profiles in VR and RW	58
4.3	Histology micrograph confirming tetrode positioning in CA1.	61
4.4	Reduction in active cell count without corresponding rate reduction	65
4.5	Reduction in active cell count in VR visible in cluster data	66
4.6	Stability of cells in VR and RW	67
4.7	Sample cells exhibiting clear spatially selective firing	68
4.8	Spatial information content in VR and RW place cells	70
4.9	Directionality of place field firing	71
4.10	Sample bidirectional cells in VR and RW.	72
4.11	Position and disto-coding index in VR and RW	74
4.12	Disto-temporal coding	75
4.13	Population vector analysis of bidirectional cells	77
4.14	Sample cells from the pillar control experiment.	78
4.15	Autocorrelation of hippocampal LFP	80
4.16	Sample phase precession in VR and RW	80
4.17	Quality of phase precession in VR and RW	81
4.18	Spike frequency of pyramidal and interneurons in VR and RW	83
4.19	Speed dependence of theta frequency	85
4.20	Speed dependent autocorrelation of interneuron spiking in VR and RW	86
4.21	Opposite running directions are not different environments	89

4.22	Rotation triggered population vector analysis.	90
4.23	Disto-code persists under active turning.	92
4.24	Same cell ratemaps in VR and RW exhibit chance level similarity.	94
4.25	Comparison of same cell properties in VR and RW.	95
4.26	Sample cells recorded in both VR and RW	96

ACKNOWLEDGMENTS

A subset of the results in chapter 4 are included in the following publication: P. Ravassard, A. Kees, B. Willers, D. Ho, D. A. Aharoni, J. Cushman, Z. M. Aghajan, and M. R. Mehta, “Multisensory Control of Hippocampal Spatiotemporal Selectivity”, *Science*, doi:10.1126/science.1232655, May 2013.

VITA

- 2008 MSc Theoretical Physics, University of Cape Town
- 2006 BSc(Hons) Theoretical Physics, University of Cape Town
- 2005 BSc Physics, University of Pretoria

PUBLICATIONS

P. Ravassard, A. Kees, B. Willers, D. Ho, D. A. Aharoni, J. Cushman, Z. M. Aghajan, and M. R. Mehta, “Multisensory Control of Hippocampal Spatiotemporal Selectivity”, *Science*, doi:10.1126/science.1232655, May 2013

C. Dominguez, J. Jottar, M. Loewe, and B. Willers, “Electromagnetic and Scalar Pion form factor in the Kroll-Lee-Zumino model”, *Nuclear Physics B - Proceedings Supplements*, vol. 186, pp. 141–144, Jan. 2009

C. Dominguez, M. Loewe, and B. Willers, “Scalar radius of the pion in the Kroll-Lee-Zumino renormalizable theory”, *Physical Review D*, vol. 78, Sept. 2008

C. Dominguez, J. Jottar, M. Loewe, and B. Willers, “Pion form factor in the Kroll-Lee-Zumino model”, *Physical Review D*, vol. 76, Nov. 2007

CHAPTER 1

Introduction

1.1 Measuring neural activity

A variety of techniques are available to perform functional measurements of neural activity. In humans, where techniques must by necessity be non invasive, functional magnetic resonance imaging (fMRI) is commonly employed to measure blood oxygenation in the brain. However, fMRI lacks both the spatial and temporal precision required to study neural circuits in detail.

Another popular class of techniques are based on optical imaging, typically using fluorescence microscopy with calcium indicator dyes or voltage sensing dyes. While such optical methods can successfully record activity from a large number of neurons, and enable accurate identification of neurons over multiple recording sessions, they have two key shortcomings. The first challenge is that the temporal resolution of measurements is insufficient to detect single action potentials, a problem which may be overcome in future using faster dyes and more sensitive imaging devices. The second problem faced by optical techniques is the inability to record from deep brain structures. Two-photon microscopy, the leading candidate for deep imaging using optical methods, is only feasible up to depths of several hundred micron.

For these reasons, the majority of functional studies of intact neural circuits in animal models employ electrical recording from electrodes implanted in the brain. Electrode based recording methods can be used to record either the membrane potential of individual neurons, or the extracellular activity of a small patch of neural tissue. They offer significantly better

temporal resolution than optical methods, but cannot as easily and reliably identify and record from the same cell over multiple recording sessions.

The potential difference across the cellular membrane of a neuron is typically referred to as the membrane potential. An ionic concentration gradient maintained across the member by ion channels and pumps maintain the baseline value of the membrane potential on the order of $-70mV$ [1]. When the membrane potential exceeds a threshold of around $-55mV$ a large and rapid electrical impulse, termed an action potential, is produced. Typical action potentials last roughly 1ms with an amplitude of $100mV$. These action potentials are activity propagated down the axon and trigger the release of neurotransmitters at synapses formed with other neurons. The action potentials, often simply referred to as *spikes*, are the primary output of neurons, and thus of particular interest in recordings. Methods to record the membrane potential of a neuron include sharp electrodes [2], which pierce the cell membrane, or patch clamp recordings [3] which employ micro pipettes to create a high impedance seal with a portion of the membrane. While such recordings deliver an unparalleled amount of data about the sub threshold activity of a neuron, they are difficult to perform in behaving animals, and only record the activity of single neurons.

As a result of these drawbacks, the majority of functional recordings in behaving animals are performed using electrodes inserted into the extracellular medium. The resulting potential between the electrode and a suitable ground is thus created by the combination of current sources and sinks caused by current flowing across nearby cell membranes [4]. Extracellular recordings typically contain data in distinct frequency bands. At high frequencies, typically above 300 Hz, the spiking activity of nearby neurons is detectable in the form of extracellular spikes. The lower frequency signal, typically below 300 Hz, is referred to as the local field potential (LFP). The precise nature and origin of the LFP is not clear, although it is generally considered to be representative of the synaptic inputs received by nearby neurons [4–6]. The length scale for contributions to the LFP is thought to be roughly $200 \mu\text{m}$ [7, 8].

Extracellular spikes are typically much smaller than those observed in membrane poten-



Figure 1.1: Scanning electron microscope image of a tetrode probe. Four $13 \mu\text{m}$ nichrome electrodes are twisted together and the insulation fused with a heat gun.

tial recordings. An extracellular electrode can detect spikes from neurons up to $150 \mu\text{m}$ from the electrode [9], which makes it possible to detect spiking activity from multiple neurons on a single electrode. Separating these spikes by the neuron of origin, a process referred to as spike sorting, is an important problem in extracellular recording. The basis of the technique is that different neuron types, together with different neuron-electrode geometry configurations, will produce different extracellular waveforms [10]. Neurons further away from the electrode are typically harder to isolate, and in practice single unit isolation is often only possible for neurons within $50 \mu\text{m}$ of the electrode [9, 11]. Most spike sorting is done manually, a process which is both extremely subjective and error prone [12]. A more detailed discussion of the sorting process, together with an improved algorithm for systematic sorting are presented in chapter 2.

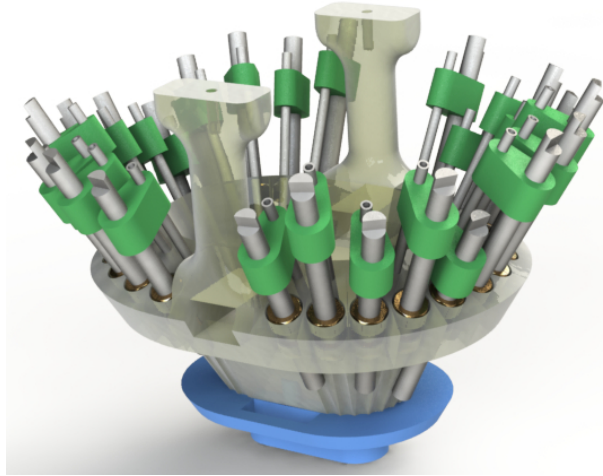


Figure 1.2: Micro-drive design with twenty two tetrode shuttles. Each tetrode is threaded through a narrow tube attached to a screw, allowing independent depth adjustment of each tetrode.

To enhance the variability in waveforms from different neurons multiple electrodes can be bundled together into a single probe. A probe configuration with four such channels, termed a *tetrode* (see figure 1.1), has been shown to significantly enhance the isolation of single units [13]. To employ such probes when recording from behaving animals, a micro-drive containing multiple individually adjustable probes is surgically fixed to the skull. Our experiments using rats use a twenty-two tetrode micro-drive (see figure 1.2) weighting approximately 25 grams.

1.2 Spatial representation in the hippocampus

1.2.1 The hippocampus

The hippocampus, a curved structure located in the medial temporal lobe, has been the subject of considerable study as a result of its role both in spatial navigation and short to long term memory consolidation.

The importance of the hippocampus to memory formation was first elucidated by an influential study by Scoville and Milner, in which they reported that surgical lesions of the

hippocampus in a human patient lead to severe anterograde amnesia [14]. The patient was unable to form new memories, but retained memories from long before the operation. This suggested that the hippocampus played a key role in the formation and consolidation of new memories. The hippocampus and the related cortical structures forming the medial temporal lobe are considered to be responsible for declarative memory [15, 16].

Single unit recordings from hippocampal neurons in rats lead to the discovery that these cells fire selectively in certain spatial regions within the environment [17]. The discovery of these cells, termed *place cells*, suggested that in addition to its role in declarative memory formation the hippocampus is an integral part of the brain's spatial processing system [18].

1.2.2 The hippocampal rate code

The discovery of place cells [17] led to the suggestion that these cells could serve as the basis for generating a cognitive map of the environment [18]. Such spatially selective firing is found in multiple subregions of the hippocampus, including CA1 and CA3 [19], and the dentate gyrus [20].

The region of space within which a place cell is active is termed a *place field*. Unlike sensory cortical areas place fields do not exhibit topographic organization [21], but the size of place fields do increase systematically along the dorsa-ventral axis of the hippocampus [22]. The instantaneous firing rates from a local population of hippocampal cells, whose place fields are distributed throughout the environment, forms an accurate representation of the rat's position [21] which is referred to as the hippocampal *rate code* [23].

Place cells have been the subject of intensive study since their discovery, and numerous interesting properties have been revealed [24]. One curious feature is that during free behavior in a two dimensional environment place cells respond only to the position of the animal. However, when the animal is constrained to run on a narrow linear track place cells exhibit firing which is both spatially and directionally selective [25]. Later experiments revealed that in a two dimensional environment with a sequential task the place cells do in fact exhibit

directional selectivity [26].

Behavioral studies have demonstrated that the hippocampus is necessary for spatial learning [27]. Consistent with this observation, place field properties demonstrated systematic changes with experience [21, 28, 29]. The changes include a backward shift in the place field center of mass, and a negatively skewed increase in firing rate [28, 29] which are predicted as a result of spike-timing dependent plasticity [30, 31]. Furthermore, populations of place cells active during track behavior exhibit sequential reactivation during slow-wave sleep [32–34], a phenomenon which is hypothesized to be involved in memory consolidation.

Besides their spatial selectivity, hippocampal firing rates have also been demonstrated to be modulated by several variables and behaviors. In particular, running speed [35–40] reward conditions and other non-spatial behaviors and stimuli [36, 41–46] all contribute to hippocampal activity. The subpopulation of cells that are active is different between different environments [21]. Subsequently, deforming the environment can cause a different set of cells to become active in a process termed *remapping* [47].

1.2.3 The hippocampal temporal code

While there are many oscillatory bands in the LFP, during active behavior the dominant activity in the LFP are large amplitude oscillations in the theta band ($\sim 8\text{Hz}$) [48]. The timing of spikes within place fields with respect to the theta rhythm has been shown to provide a temporal code for the rat’s position [25, 49] beyond the position information present in the spatial firing rate. In particular, each successive spike as the rat traverses the place field occurs at a lower phase of the theta oscillation than the previous spike, an effect referred to as *phase precession*. Data recorded across multiple runs through the place field reveals that spikes precess through a full 360° cycle over the width of the place field, but on a single run precession is often only 180° [50].

The addition of spike phase information can provide greater accuracy in position decoding based on a small number of place fields, as it provides a mechanism for encoding position

which is independent of behavioral confounds such as running speed [51, 52]. While phase precession is primarily studied using linear track experiments, it has been shown that an animal’s trajectory through a place field in a two dimensional environment can be disambiguated by the temporal code [53]. Besides greater information for spatial decoding, phase precession also produces sequential activation of adjacent place fields on the timescale of spike timing dependent plasticity [30, 31], which is believed to be important for sequence learning [54–56]. Phase precession has also been demonstrated in layer 2 grid cells in the medial entorhinal cortex [57], suggesting that its generating mechanism is broadly applicable.

The mechanisms generating phase precession have attracted considerable modeling interest, with a wide variety of models in the literature. Many of these models are based on the notion that the LFP, and theta oscillations in particular, correspond to rhythmic inhibitory input to the place cells. This idea is consistent with finding that most hippocampal interneurons provide perisomatic inhibition to pyramidal neurons [58].

While there are a number of different models for phase precession, they can be split into three categories. The first of these are oscillatory interference models [25, 59], which model the membrane potential as the combination of oscillating somatic and dendritic inputs. Within the place field, the dendritic oscillator is assumed to exhibit a speed dependent frequency increase which, when coupled with spiking activity at the peaks of the interference pattern in the membrane potential, leads to spatial phase precession. The second class of models are based on recurrent network activity [60, 61]. Precession is proposed to be the result of a sequence of associated place cells activity within each theta cycle. Due to the need for recurrent connections such models cannot explain precession in CA1, which lacks recurrent excitatory connections. The third class of models involve spatially modulated depolarization, which forms the place field, interacting with rhythmic inhibition. In the soma-dendrite interference models [62, 63] the depolarizing input is also modulated by the theta rhythm. An asymmetric ramping depolarization has also been shown to be capable of generating phase precession [29, 64–66]. Recent membrane potential recordings in mice [67] displayed such ramping excitation, consistent with observations of asymmetric spiking activity in rats [28,

29, 66].

1.2.4 Sensory inputs and place fields

The relationship between the cues in the environment and place fields has been studied in some detail, although no clear consensus has been reached on which sensory modalities are responsible for the generation of place fields. Early experiments indicated that the most important influence may be the distal visual cues in the environment. Indeed, rotating the visual cues in a cylindrical chamber causes the place fields to rotate [68].

In support of the importance of visual cues, place cells in rats which are introduced to an environment in darkness remap when the lights are turned on [69]. However, no remapping is observed if the environment is initially illuminated and the lights are then turned off. Other sensory cues such as olfactory and self motion cues must thus be capable of maintaining the rate code. This is consistent with the presence of normal place fields in blind rats [70]. The contribution of olfactory and self motion cues may explain findings that the hippocampus can respond differently to two identical visual environments [71].

It has been reported that wiping the track between trials of a linear track causes place fields to remap [72], while the fields are stable, even in darkness, if the track is not wiped down. Furthermore, the additional of proximal cues to the track increase the fraction of place cells active in both directions [73]. Lesions or chemical based deactivation of the vestibular nucleus has also been shown to disrupt place cell firing and destroy head direction selectivity [74, 75].

1.3 Outline

More than forty years after the discovery of place cells, there is still no consensus as to the sensory stimuli that govern the formation of place fields. In part this is due to the substantial difficulty in eliminating non-specific sensory cues. There is evidence to suggest that distal visual cues play a dominant role, but cells are modulated by multiple sensory modalities.

In this dissertation I will discuss the design of a virtual reality system which attempts to mitigate these problems. This virtual reality system, combined with an improved spike sorting method, is then applied to definitely answer the question of whether visual cues alone are sufficient for place cell activity in CA1.

In chapter 2 I discuss the spike sorting problem in some detail, including an overview of existing methods, followed by details of the sorting pipeline I have developed for tetrode data using a combination of existing algorithms and some post processing heuristics. Thereafter chapter 3 provides further discussion on the motivation behind virtual reality for rats. By examining the sensory capabilities of the rat we obtain a set of requirements, followed by information about the hardware design and software implementation. The work presented in this chapter is result of joint effort with Daniel Aharoni. Having established the tools to be used, chapter 4 presents the analysis of place cells recorded in highly similar real and virtual linear track environments. Details of the similarities and differences, together with the calculations done to obtain them are provided. Many of the results from this chapter appear in our publication [76]. The experiment was designed by all authors, data collection was primarily performed by Pascal Ravassard and Ashley Kees, and all analysis performed by myself. Finally, chapter 5 provides further discussion of the results obtained, directions for possible future research, and concluding remarks.

CHAPTER 2

Spike sorting

Extracellularly positioned electrodes produce recordings which typically include contributions from both the local field potential and action potentials from multiple nearby neurons. While the analysis of multi-unit activity can be worthwhile, it is clearly desirable to isolate individual cells in the recording to study the firing properties of single units. This is referred to as the spike sorting problem, and remains a field of active research.

In this chapter I will outline the general techniques used, together with details of the sorting procedure I have developed, which combines some of the existing techniques with new algorithms and software tools. We begin by considering the stages into which the spike sorting process is typically divided:

1. Detecting action potentials;
2. extracting and aligning spike waveforms;
3. dimensionality reduction and feature extraction;
4. sorting the data into clusters.

2.1 Detection

Extracellular action potentials tend to be quite small (on the order of $100\mu V$), compared to the amplitude of oscillations in the local field potential. Fortunately, these two sources typically contribute in different frequency ranges, so the first step in extracting extracellular action potentials is therefore to filter the wide band recordings.

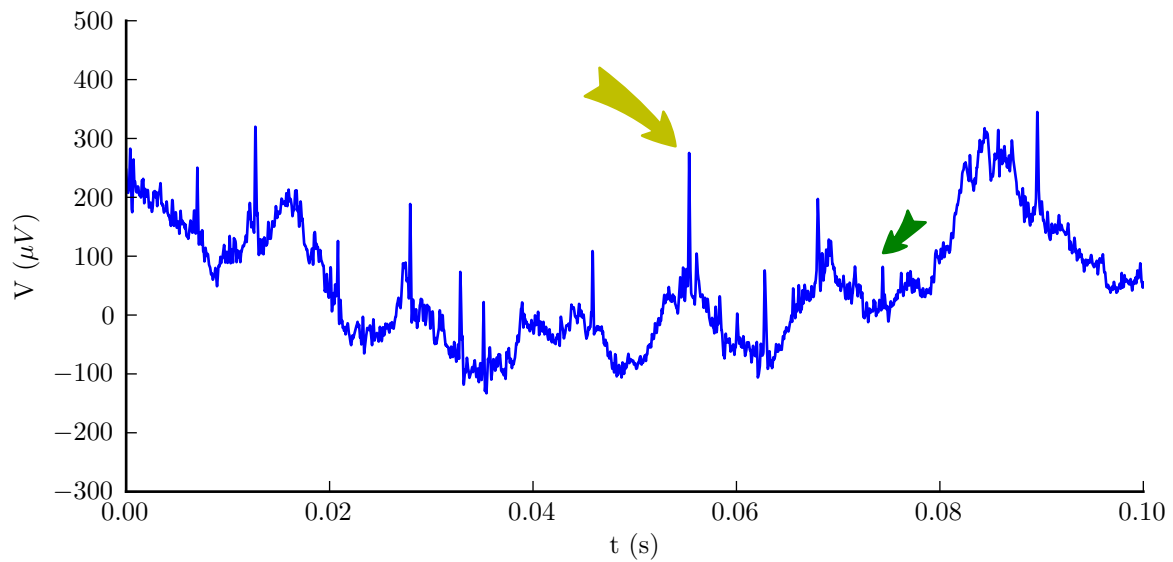


Figure 2.1: A 100ms sample of unfiltered extracellular recording. Arrows indicate spikes tracked over future figures. While intracellular spikes are positive voltage deflection, extracellular spikes are in fact negative voltage deflections. For this reason, by convention extracellular traces are inverted before plotting both here and in future figures.

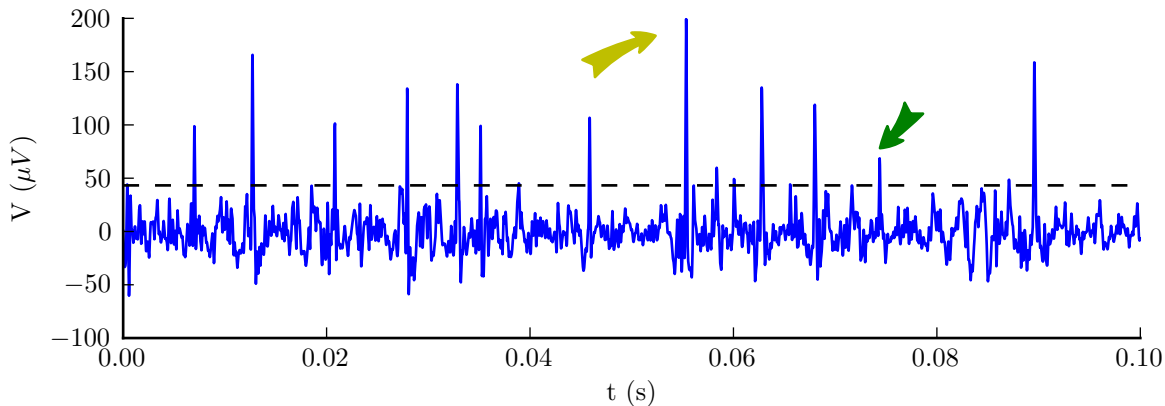


Figure 2.2: Data from figure 2.1 filtered between 300 and 6000 Hz. Dashed line indicates a 4σ detection threshold.

Typical filter ranges are 300 or 600 to 6000 Hz. Most data acquisition systems offer on-line filtering capability using finite impulse response (FIR) filters. However, such on-line (*causal*) filters introduce a phase lag which varies as a function of frequency. As a result, the resulting action potential waveforms are distorted [77, 78] in a manner which reduces accuracy of subsequent spike sorting. Off-line (*non causal*) filtering, avoids the phase lag problem by running a causal filter first forward and then backward in time over the sample. Our system employs off-line filtering using a 4th order Butterworth filter [79] with a pass band between 300 and 6000 Hz.

Once the signal has been filtered, action potentials can be detected by simple voltage thresholding. However, energy based detection methods have been shown to be more effective at reduce false positive detections [80]. We define the non-linear energy operator (NEO) as:

$$\psi[x(t)] = \left(\frac{\partial x}{\partial t}\right)^2 - \left(\frac{\partial^2 x}{\partial t^2}\right)x(t) \quad (2.1)$$

With the discrete analogue:

$$\psi_t = x_n^2 - x_{n+1}x_{n-1} \quad (2.2)$$

Through Fourier decomposition it can be shown that the value produced by this operator

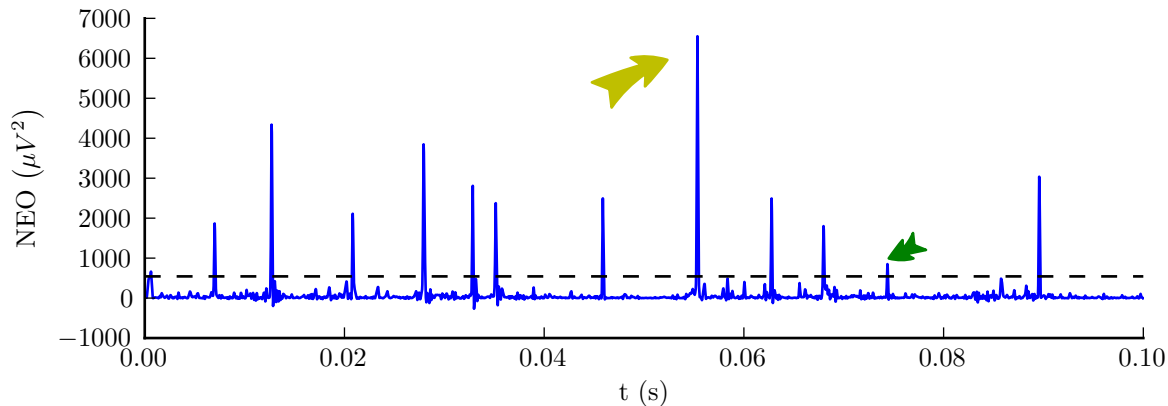


Figure 2.3: Output of the non-linear energy operator on the data in figure 2.2. Black line indicates the detection threshold. Note the improved contrast between action potentials and noise, resulting in more accurate detection.

is approximately the instantaneous power times the instantaneous frequency. Since action potentials are both large and *rapid* voltage fluctuations in the filtered signal, thresholding the NEO signal provides an excellent way of detection action potentials. A short filtered voltage trace and its NEO are depicted in figures 2.3 and 2.2.

2.2 Waveform extraction

Once spikes have been detected, and a small window of data (1.5ms in our system) is extracted on each channel around the detected event. It is important that these waveforms be properly aligned for later dimensional reduction. Typically waveforms are align using the maximum peak across recording channels, although energy based alignment mechanisms have also been shown to work well [81]. This alignment process can be improved by up-sampling the waveforms using cubic splines, performing the alignment, and then down-sampling back to the original sampling frequency [82].

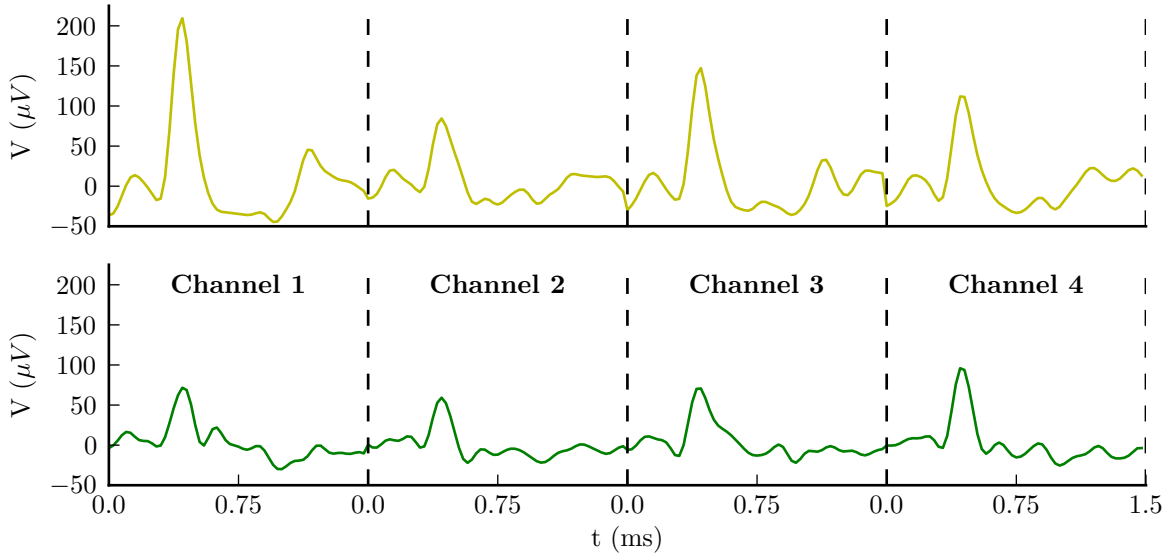


Figure 2.4: Extracted waveforms from all four channels of the tetrode probe for the spikes indicated by the arrows in figures 2.1 and 2.3.

2.3 Dimensionality reduction and feature extraction

At this stage, the dimensionality of the resulting dataset is quite large ($D = 240$ for 1.5ms waveform segments recorded at 40 kHz on the four channels of a tetrode). Much of this data is highly redundant, so there is substantial computational benefit to be had from reducing the dimensionality of the data.

We therefore seek to extract a subset of the data which is small enough to work with but still contains sufficient information identify single neurons. As discussed in section 1.1, the major advantage of recording using tetrode probes is that the same action potential can be detected on each channel, but because of the geometry of the probe the action potentials will be slightly different on each channel. Simply selecting the peak amplitude of the waveform on each of its four channels thus provides a effective way of choosing the feature set. Figure 2.5 depicts a sample of the four channel spike peaks on a well positioned tetrode.

By simply selecting the peak amplitude, however, we lose a lot of information about the shape of the waveform that can aid in classification. Principle component analysis (PCA)

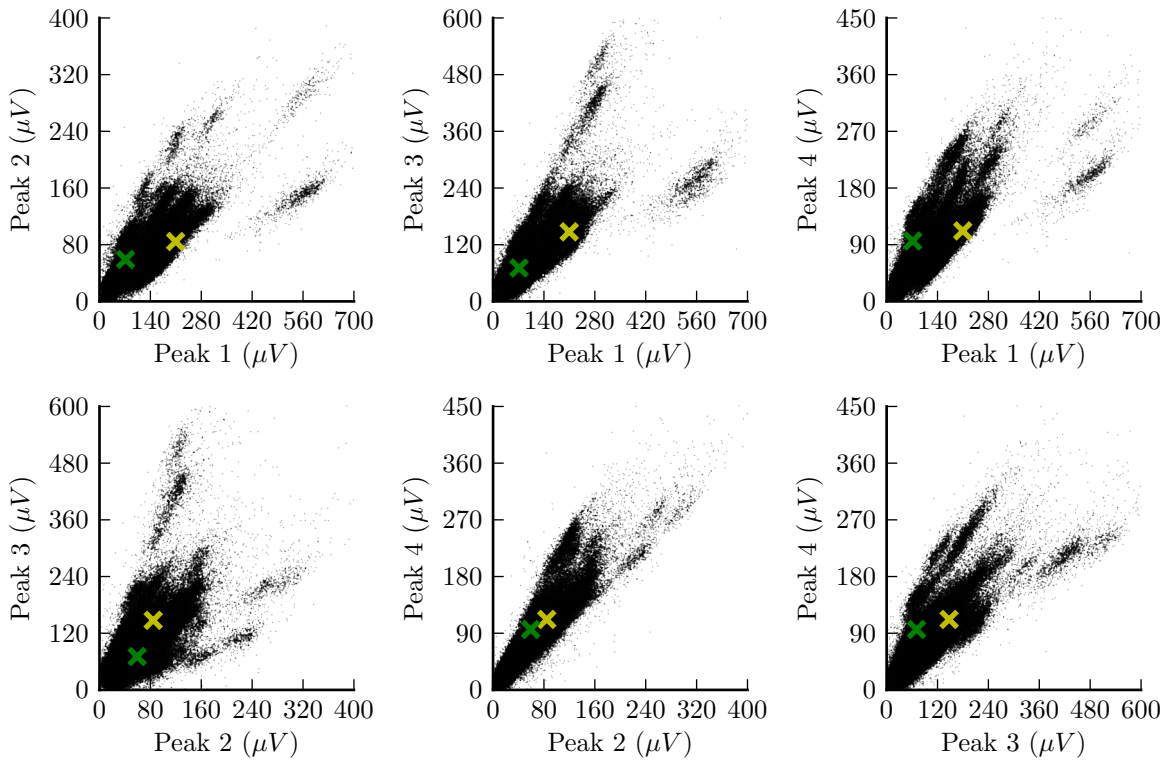


Figure 2.5: Two dimensional projections of spike peak amplitude on the four channels of the tetrode for all spikes detected during the hour of recording from which previous samples were drawn. Yellow and green arrows indicate the location of the spikes in figure 2.4

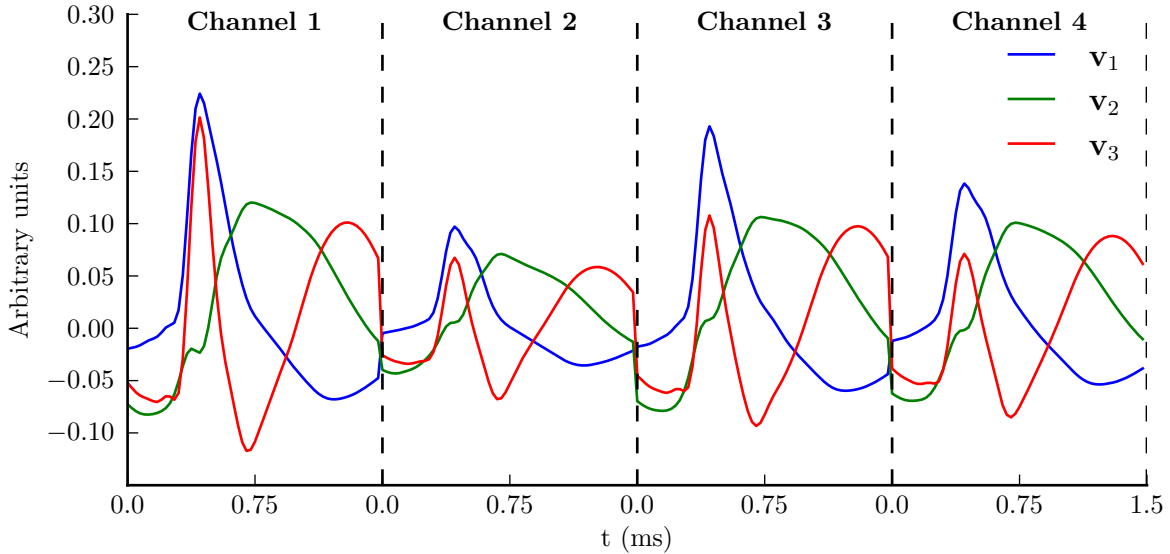


Figure 2.6: First three eigen vectors of the covariance matrix for the spike in figure 2.5. Notice that the first eigen vector mimics the shape of an extracellular spike waveform.

provides an alternative approach. Briefly, suppose the data set \mathbf{x}_i , contains N samples in D dimensions. We can estimate the covariance matrix of the data:

$$\hat{\Sigma} = \sum_i^N \mathbf{x}_i \mathbf{x}_i^T \quad (2.3)$$

and find its eigen vectors \mathbf{v}_j and eigen values λ_j such that

$$\hat{\Sigma} \mathbf{v}_j = \lambda_j \mathbf{v}_j \quad j = 1 \dots D \quad (2.4)$$

The eigen values λ_j are proportional to the fraction of the total variance in the data explained by variance along the vector \mathbf{v}_j . We can thus keep the majority of the variance in our data while reducing dimensionality (from D to M) by projecting along the M vectors \mathbf{v}_j with the largest corresponding eigen values.

$$\mathbf{y}_i = \begin{bmatrix} \mathbf{v}_1 & \dots & \mathbf{v}_M \end{bmatrix} \mathbf{x}_i \quad (2.5)$$

The first three eigen vectors of the dataset in figure 2.5 are shown in figure 2.6. While PCA is reasonably effective and fast to compute, it is fundamentally a linear transformation of the data, which limits the complexity of the structure it can extract. There is therefore a great deal of research on non-linear methods of dimensionality reduction.

Some of the proposed methods include ISOMAP [83, 84], Laplacian eigenmaps [85], and graph laplacian features [86]. While these methods are often capable of revealing interesting structure in high dimensional data, they are significantly more computationally intensive ($\mathcal{O}(n^3)$ or $\mathcal{O}(n^2 \log n)$ depending on the method) making them impractical for the datasets encountered in our experiments, which often include hundreds of thousands of data points.

Another popular approach to feature extraction is based on the discrete wavelet transform [87]. Briefly, each waveform is decomposed as a linear combination of a base ("mother") wavelet at a variety of offsets and scale factors. The coefficients generated by the wavelet transform are then used as features, with deviation from a normal distribution being used as the signal for an interesting or useful coefficient [88, 89].

2.4 Clustering

Once the spike data has been reduced to a workable dimension, the next step is to identify isolated clusters in the data. These clusters should, in theory, correspond to different neurons. This assumption is usually verified through the use of several cluster metrics, described below. In addition to single unit clusters, a typical dataset contains a dense cluster of low amplitude spikes which originate at distant neurons. These low amplitude spikes are difficult to separate into multiple sources, and are typically either discarded, or used in analysis of multi unit activity.

2.4.1 Cluster metrics

In order to separate clusters that correspond to single neurons from those that do not, as well as to assess the quality of clustering, it is useful to compute a variety of metrics that

describe the clusters. Many of these metrics have a biological motivation, whereas others are largely statistical in nature.

Arguably the most important tool in identifying single neuron clusters is the knowledge that neurons exhibit a refractory period [90]: for a small time interval following an action potential, the neuron is incapable of producing another action potential. While the exact length of the refractory period varies among cell types, it is typically around one to two milliseconds. It follows that a cluster exhibiting a large number of refractory violations (two spikes falling within the refractory period of one another) is unlikely to be a single neuron. In practice the fraction of refractory spikes is often used as a simple metric, but, it is possible to compute a better estimate of the fraction of false positive spikes in a cluster [91].

Suppose the cluster is a combination of two distinct point processes. Process A, corresponding to the ‘true’ neuron, and process B, corresponding to noise or misclassified spikes. Let N_A, N_B be the number of spikes from these processes, R be the number of refractory violations, T be the duration of the recording session, τ_r the refractory period, and τ_c the censor period of the spike detection method. Process A is subject to a refractory restriction, but process B, which we assume to be Poisson, is not. Refractory violations can therefore be of type AB or type BB .

Each spike from A creates a window of $2(\tau_r - \tau_c)$ around it during which a spike from B would generate a refractory violation. We therefore expect the number of AB violations to be:

$$R_{AB} = \frac{2(\tau_r - \tau_c)N_A N_B}{T} = \frac{2(\tau_r - \tau_c)}{T} N_B (N - N_B) \quad \text{where } N = N_A + N_B \quad (2.6)$$

Under the Poisson assumption, the time between spikes from B are exponentially distributed, so the number of BB violations is expected to be:

$$R_{BB} = (N_B - 1) \left(1 - \exp \left\{ -N_B \frac{(\tau_r - \tau_c)}{T} \right\} \right) \quad (2.7)$$

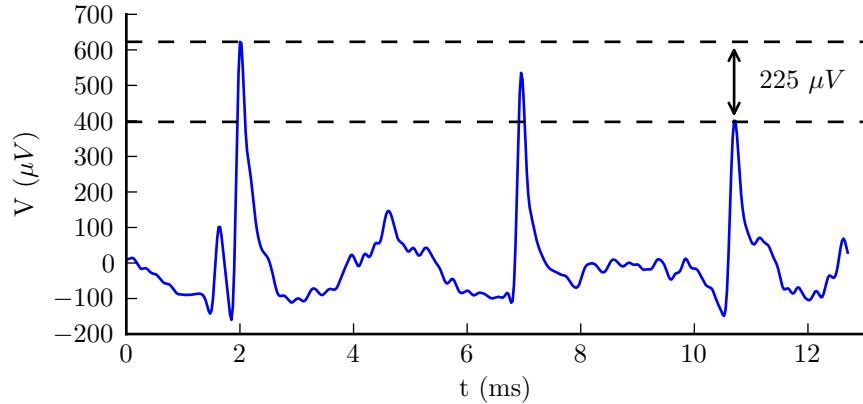


Figure 2.7: Three action potentials in rapid succession from a single cluster demonstrating complex spiking. Notice the significant reduction in spike amplitude.

Since the values of N , T , R , τ_r and τ_c are observable for a given cluster, the resulting transcendental equation

$$\frac{2(\tau_r - \tau_c)}{T} N_B(N - N_B) + (N_B - 1) + \left(1 - \exp\left\{-N_B \frac{(\tau_r - \tau_c)}{T}\right\}\right) = R \quad (2.8)$$

can be solved numerically for N_B , after which the false positive estimate from refractory spiking is simply $f_p^{(r)} = N_B/N$. It should be pointed that the zeroth order expansion of the exponential in equation (2.8) yields the result from [91], whose calculation neglected the possibility of BB refractory violations. The assumption of Poisson spiking from the noise process B is imperfect in many recordings, but is nevertheless a reasonable basis for developing the estimator.

Two more metrics with biological basis are the burst index and complex spike index [92] of a cluster. Some neurons, such as the pyramidal neurons in CA1 with which we are primarily concerned here, are known to exhibit complex spike bursts. Such a burst typically involves several spikes in rapid succession, each with smaller amplitude than the one preceding it [93, 94].

To quantify the presence of these effects, we define the burst index of a cluster as the percentage of spikes that occur within 20 ms of their predecessor. The complex spike index

(CSI) is then defined as the percentage of spikes within a burst that exhibit amplitude decay minus the percentage of spikes within a burst that exhibit an increase in amplitude relative to their predecessor. For cells which do not exhibit complex spiking, such as the inhibitory interneurons near CA1, the CSI will typically be close to zero, while for pyramidal neurons in CA1 values of 50% or higher are not uncommon.

A common metric to quantify the separation between clusters is the isolation distance [95]. It is defined, for a given cluster, as the Mahalanobis distance (computed on peak amplitudes using the cluster mean and covariance) threshold at which the number of spikes below the threshold is twice the number of spikes in the cluster. Unfortunately this metric is dependent on the number of dimensions in the data. Transforming this distance using the chi-square distribution with the appropriate number of dimensions would avoid this problem, but this is rarely done in practice. Subsequently, care should be taken when comparing isolation distances reported in different publications.

Finally, one can use the assumption of Gaussian clusters to derive estimates of the probability of misclassification for each data point, which subsequently leads to false positive and negative estimates for each cluster [91].

2.4.2 Clustering algorithms

The literature proposing algorithms for spike sorting goes back almost as far as electrophysiology does [96]. Methods that have been proposed include:

- Over clustering using k-means followed by merging based on edge density [97];
- Density contour based approaches [98];
- Self organizing maps [99];
- Neural networks [80];
- Optimal linear filters [100];

- Gaussian mixture models [11];
- Independent component analysis [101–103];
- Student’s t-distribution mixture models [104–106];
- and many more [83, 107–110].

Despite all these approaches, the spike sorting problem remains unsolved. This is due in part to the large variation of cell types, densities and firing rates in different brain regions, as well as the challenges of electrode drift, complex spiking and overlapping waveforms. Some of these methods attempt to be fully automated, while others are semi-automatic and require operator input at key stages in the sorting process. Regardless of the algorithm used, manual inspection of the output remains an important verification step.

While a full review of all these methods is beyond the scope of this chapter, I want to briefly motivate our choice of algorithm. It is typical in our experiments to need to sort on the order of two or three hundred thousand spikes from a single recording session. The large number of spikes immediately precludes the use of techniques with runtime $\mathcal{O}(n)^2$ or higher. Due to the large difference in firing rate between interneurons and pyramidal units in CA1, the method must also be able to successfully identify both high and low density clusters.

As a compromise between the goal of fast execution time and quality of output, we adopted the KlustaKwik algorithm [111], together with further post-processing of the output. Briefly, KlustaKwik fits Gaussian mixture models to the spike data, using the Akaike information criterion [112] to determine the number of components in the model. Because spike data is rarely purely Gaussian, it tends to split single clusters into multiple components. On occasion, multiple low rate clusters are grouped together in a single component. We must therefore detect which components to merge, and which components to split.

Intuitively, components should be split if their peak data are overlapping, and their waveforms are similar. This is quantified as follows: let $\mathbf{x}_i^{(1)}$ and $\mathbf{x}_j^{(2)}$ be the peak amplitude data for two clusters. Estimate the mean $(\mu^{(1)}, \mu^{(2)})$ and covariance $(\Sigma^{(1)}, \Sigma^{(2)})$ of the clusters

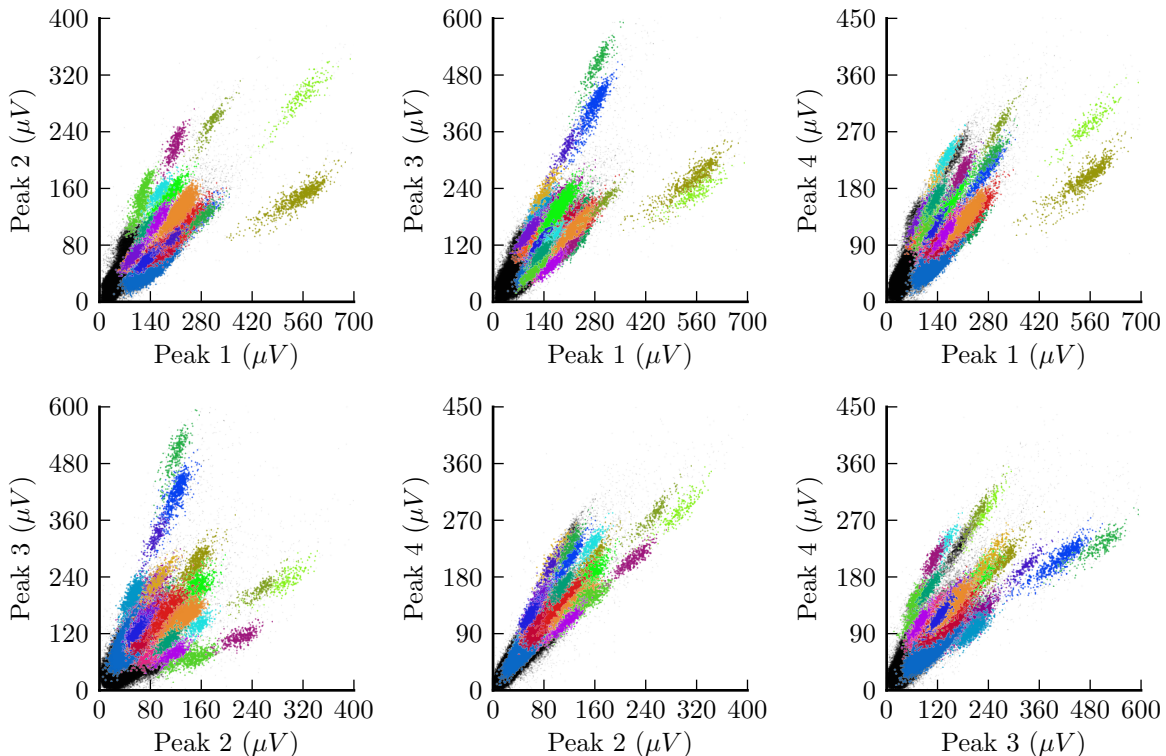


Figure 2.8: Output of the clustering algorithm on the data in figure 2.5. The algorithm identifies 24 clusters and subsequent manual inspection confirms 23 of these as single units.

from the data. Then compute the Mahalanobis distance across clusters:

$$m_i^{(1)} = \left(\mathbf{x}_i^{(1)} - \mu^{(2)} \right)^T \Sigma_{(2)}^{-1} \left(\mathbf{x}_i^{(1)} - \mu^{(2)} \right) \quad (2.9)$$

$$m_j^{(2)} = \left(\mathbf{x}_j^{(2)} - \mu^{(1)} \right)^T \Sigma_{(1)}^{-1} \left(\mathbf{x}_j^{(2)} - \mu^{(1)} \right) \quad (2.10)$$

and define the distance measure M as the maximum of the means.

$$M = \max \left(\frac{1}{N_1} \sum_{i=1}^{N_1} m_i^{(1)}, \frac{1}{N_2} \sum_{j=1}^{N_2} m_j^{(2)} \right) \quad (2.11)$$

Rather than directly thresholding M , whose typical values are not very intuitive, we again use the assumption of Gaussian data to convert M to the better understood range of cumulative probability, and merge clusters if $\beta = \text{CDF}_{\chi_d^2}(M) > 0.95$, and the Pearson correlation coefficient of the mean waveforms exceeds $\rho > 0.9$.

If a component contains more than one well isolated cluster, the density of spikes around the cluster mean is likely to be low (since the cluster mean should lie in between the two well isolated clusters). We therefore detect clusters to be split by computing the Mahalanobis distance of each spike in the cluster $m_i = (\mathbf{x}_i - \mu)^T \Sigma^{-1} (\mathbf{x}_i - \mu)$. We expect roughly 20% of spikes to fall within the quintile threshold m_T defined by $CDF_{\chi^2_d}(m_T) = 0.2$. If the fraction of spikes below this threshold ($\frac{\sum_i \Theta(m_T - m_i)}{\sum_i 1}$, where Θ is the heaviside function) is below 12.5%, we identify the component as needing to be split, and rerun on the KlustaKiwk algorithm on the data assigned to the component. The result of this post processing is shown in figure 2.8.

2.4.3 Manual clustering

Despite the inherent subjectivity involved, much electrophysiology data is clustered manually by a human operator. The process typically involves iterating over two dimensional projections of various spike features (see section 2.3) and visually identifying isolated clusters. Once such a cluster has been identified, the operator creates a boundary around the cluster, and the data within the all boundaries are considered to be part of the cluster. As this process is repeated the boundaries of individual clusters can be iteratively refined.

While there exist several software packages to perform such manual clustering, they are either tied to specific vendor hardware (e.g. *SpikeSort3D*, Neuralynx, MT), platform specific (e.g. *Klusters* [113]) or dependent on expensive commercial software environments (e.g. *MClust*, A.D. Redish). For these reasons, together with the flexibility to incorporate automated algorithms and improvements to the work flow available in these packages, I have developed an alternative package, which I have unimaginatively dubbed *PyClust*. The advantages of PyClust over its competitors include:

- No commercial dependencies, written entirely in Python using open source libraries.
- Cross platform, tested on Windows XP, Windows 7, Mac OS X, Ubuntu Linux 12.04.
- Support for both elliptical and polygon boundaries.

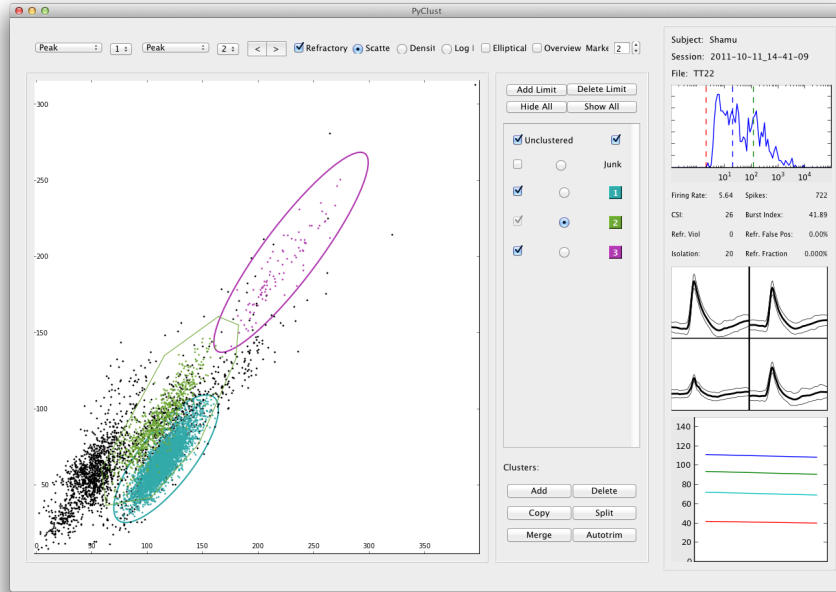


Figure 2.9: A sample dataset being clustered using the PyClust software package.

- Automatic boundary estimation.
- Algorithmic cluster splitting based on Gaussian mixtures.
- Easily extendable to various input file formats.
- Allows manual inspection of algorithmic clustering results.

Most of the details of implementation are uninteresting¹, but the automatic boundary estimation tool warrants discussion. If the data \mathbf{x}_i for a cluster were drawn from a multivariate normal, then $\chi_d^2 = \mathbf{x}^T \Sigma^{-1} \mathbf{x}$ is drawn from the chi-square distribution with d degrees of freedom, where d is the dimensionality of \mathbf{x} . Suppose a cluster contains N spikes, with N_r refractory violations. Each refractory violation involves two spikes, at least one of which should not be assigned to the cluster. We thus define a threshold T such that:

$$CDF_{\chi_d^2}(T) = 1 - \frac{1}{N - N_r} = \alpha \quad (2.12)$$

¹source code available at <http://bitbucket.org/bwillers/pyclust>

For a sample of $N - N_r$ data points drawn from the χ_d^2 distribution we would expect none of the data to exceed T , so we discard data past this threshold. In effect this procedure creates an ellipsoid boundary corresponding to the $\alpha = 1 - \frac{1}{N - N_r}$ confidence interval of the d dimensional normal distribution. If we apply this strategy to two dimensional projections of the data we obtain elliptical boundaries, that can then be visually inspected by the operator.

Since each such boundary will constrain the data and change the number of refractory violations, the outcome is dependent on the order in which we apply boundaries to each projection. We therefore calculate the effect of the proposed boundaries on every projection, and choose the one which yields the greatest improvement in the fraction of refractory spikes $\frac{N - N_r}{N}$.

A sample of the output of the algorithm on 6 dimensional principle component data is shown in figure 2.10. The first and second boundaries that are chosen (third row, third and first columns respectively) effectively remove almost all refractory spike violations in this example.

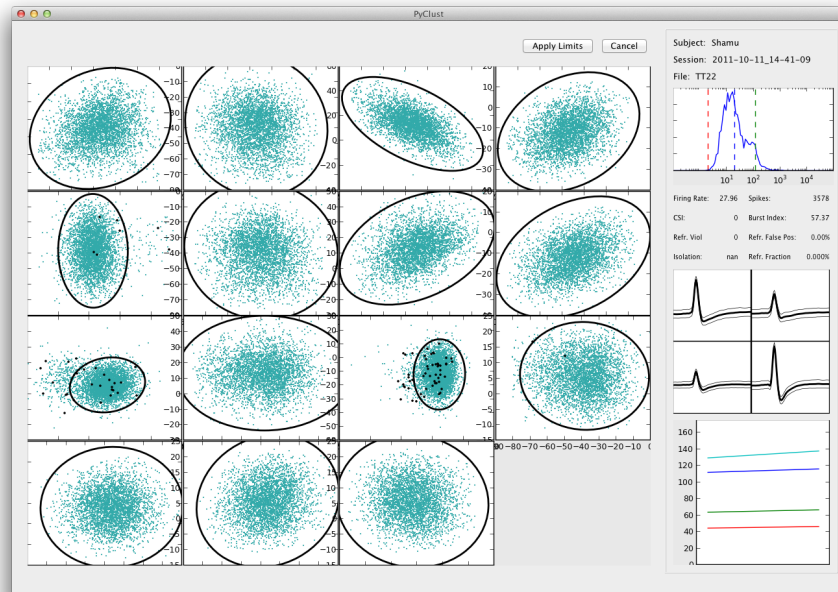


Figure 2.10: Boundaries produced by PyClust’s autotrim tool on first cluster visible in figure 2.9.

2.4.4 Electrode drift

An important challenge in spike sorting is the problem of electrode drift. Since the electrodes are not physically attached to the neurons they are recording from, it is possible, and in fact quite common, for the position of either the electrode or the cells to move slightly over the course of a recording session. The resulting systematic variation of the spike amplitude can substantially complicate the clustering process. Figure 2.11 is an example of such electrode drift. Notice how two distinct single units become indistinguishable as a result of the drift in peak amplitude.

One approach to solving the drift problem is to use some form of template matching or matched filters [100] to identify spikes in the filtered extracellular recording. By continually updating the template with an average of the recently detected waveforms it is possible to track the drifting waveform. Unfortunately this approach is complicated by the prevalence of complex spike bursts (figure 2.7), which lead to a large change in spike waveforms on a short

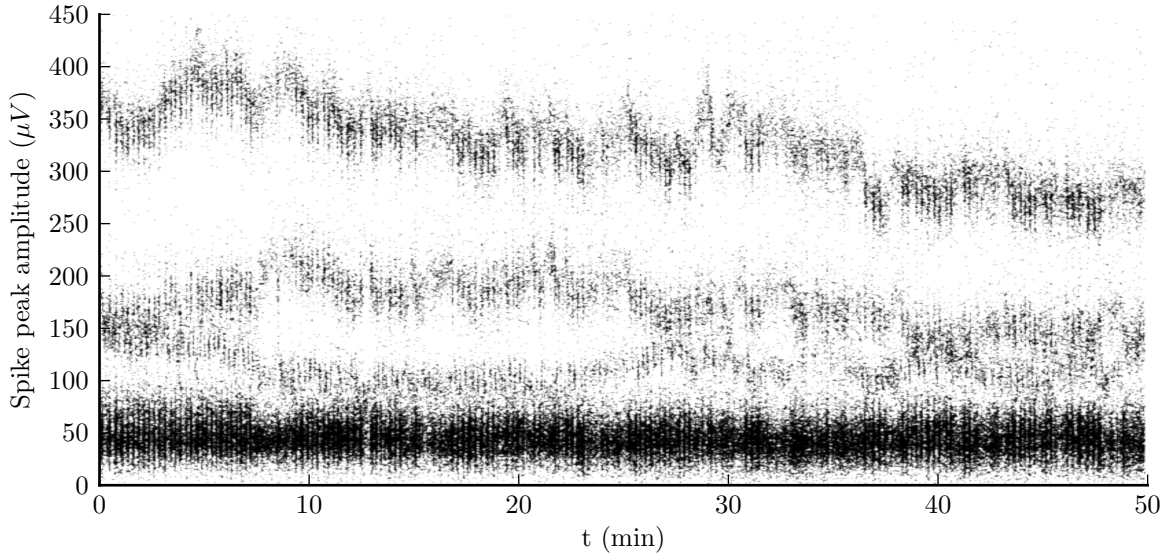


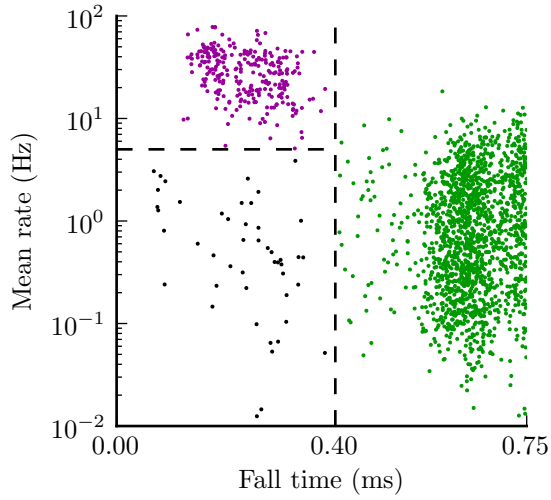
Figure 2.11: Spike peaks over an hour long session demonstrating the problem of electrode drift. Clearly three units are present in the recording, but two of the units are ambiguous as a result of drift.

timescale. The challenge is thus to design a template matching routine which is sensitive to longer timescale changes, but can still successfully match large variations in waveforms on a short timescale.

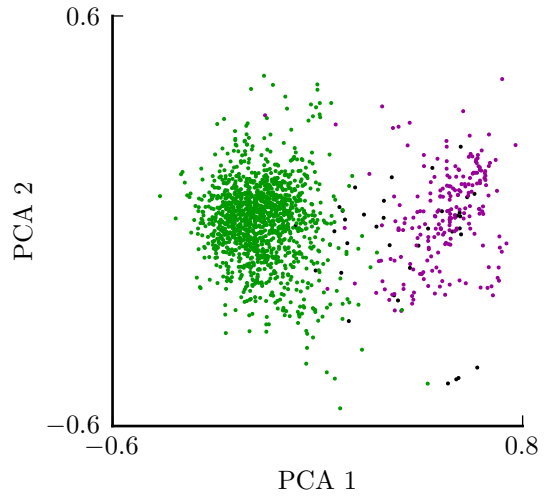
2.5 Unit classification

There are many cell types in the CA1 region, including excitatory pyramidal neurons and a many types of inhibitory cells. In order to perform sensible analysis of single unit data, we must therefore attempt to classify the cell type of each unit. While differentiating between different interneuron types based only on electrophysiological recording is exceeding difficult, there is fortunately a clear difference between pyramidal and interneuron data.

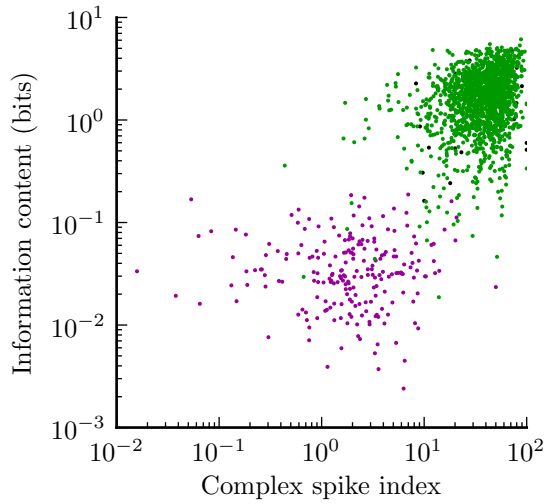
Typically, the fall time of the waveform for pyramidal units is significantly slower than that of interneurons, and the firing rates much lower. We can thus classify cell types based on a joint fall time and firing rate threshold, as shown in figure 2.12a.



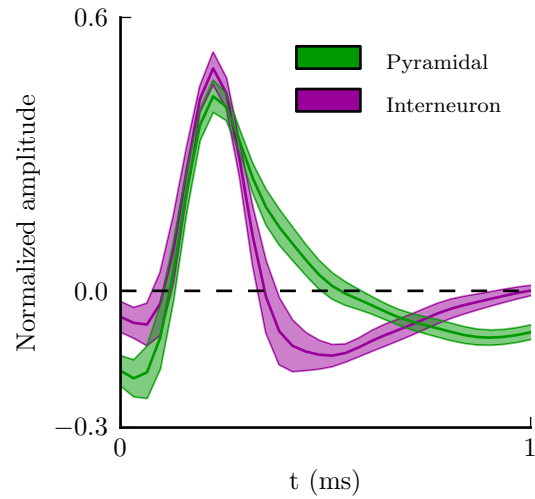
(a) Fall time / firing rate classification.



(b) Principle component classification.



(c) Spatial information and complex spiking.



(d) Waveforms (mean \pm std. dev.) of waveforms.

Figure 2.12: Classification of pyramidal and interneuron units based upon waveform and firing properties.

The output of this heuristic classification scheme can be confirmed in two ways. We can confirm the existence of two classes of waveforms by normalizing each unit's mean waveform (such that rms power is unity) and applying principle component analysis to a collection of single units in a dataset (figure 2.12b). Using the knowledge that pyramidal cells exhibit complex spiking and exhibit spatially selective firing, comparison of the CSI and spatial information content (see section 4.4.3) of the waveform classes confirms the identification of inhibitory and excitatory units (figure 2.12c).

Having established the method used to resolve single unit activity from extracellular recording, we now turn to the virtual reality system with which experiments were performed.

CHAPTER 3

Virtual reality for rats

3.1 Introduction

In this chapter we will outline the motivation for virtual reality as an experimental protocol, the design of the virtual reality system, and some sample behavioral data to demonstrate the capabilities of the system.

3.1.1 Motivation

Rodent models have played a key role in our understanding of the neural mechanisms of spatial behaviors and representations [17]. While more complicated models which are closer to humans both anatomically and genetically are available, experimentation on primates is controversial, difficult and extremely expensive. Rodents provide a middle ground between the dual goals of a sufficiently complex animal model and practical experimental concerns, including cost and available recording techniques.

The study of neural activity in rodent models during spatial behavior has yielded many important findings, including the original discovery of the place cell [17] and phase precession [25] in the hippocampus and grid cells [114] in the entorhinal cortex. However, there are three important problems which limit our ability to gain deeper insight into the underlying mechanisms of these effects.

The first problem is in identifying the role different sensory modalities and stimuli play in the formation of neural spatial representations. While place cells are thought to be driven primarily by distal visual stimuli [18, 68] and self-motion cues [115, 116], spatial navigation

and hippocampal activity have also been shown to be influenced by other sensory stimuli including smells [44, 72], sounds [117] and somatosensation [118]. It is exceedingly difficult to design an experiment wherein sensory inputs in all modalities can be carefully accounted for.

The second problem lies in the limitations of recording techniques. As discussed in section 1.1, extracellular recording via single electrodes, tetrodes, or silicon probes, while suitable for recording from freely behaving animals, are limited by their inability to record membrane potentials of single cells, and their difficulty in reliably recording from the same cell population over many days. While patch clamp and sharp electrode recording techniques can record membrane potentials, they generally require a head fixed subject [3]. There has been some progress in recent years in developing microdrives for intracellular recording from freely behaving animals [119, 120], but successfully employing these techniques remains challenging.

Optical recording methods, such as calcium dye imaging using confocal or multi-photon microscopy allows stable recording from a large population of cells [121, 122], but similarly requires a head fixed subject. As with intracellular recordings there has been tremendous research effort applied to problem of miniaturizing optical recording tools to allow for recording from freely behaving animals [123–125], with some very recent success [126]. What is needed, then, is a experimental design within which animals can express spatial behaviors whilst being head restrained.

Finally, some potentially interesting experiments are either impractical (e.g. exploring very large environments) or impossible (instantaneous ‘teleportation’ or alteration of spatially informative cues in all modalities, environments without boundaries, etc.) to perform in the real world.

For these and other reasons there has been an increasing interest in the use of virtual reality experimental protocols. These techniques, in a simple form, have been in use with insect models for some time [127, 128]. Studies have also shown that primates are capable of navigating virtual environments presented to them on a screen [129]. Early attempts at

creating a virtual reality apparatus for rodents involved multiple display monitors positioned throughout a Y-shaped track, and had limited success [130]. More recently, a linear treadmill was combined with a back-projected half-dome screen [131].

The biggest improvement in recent years [132] provided several key advances: a toroidal projection screen with an angular amplification mirror enabled projection for 360 azimuthal degrees; and a spherical treadmill enabled tracking of two-dimensional motion information. Based on these ideas, both intracellular [67] and optical [133] recording from the CA1 cell layer of a mouse model on a linear track have been reported in recent years. While the majority of focus in the literature in recent years is on virtual reality to enable head-fixed recording, the multi-modal stimulus control aspect has not received much attention.

In this chapter I will briefly describe the design of our virtual reality apparatus, which improves upon existing systems in four ways: significantly improved visual projection field of view; the addition of realistic auditory stimuli; monitoring of reward checking behavior; and software support for more complex environments, including spherical and cylindrical geometries.

3.1.2 Sensory capabilities of the rat

In order to design a virtual reality system for rats, it is necessary to first understand as much as possible about the sensory capabilities of the animals. Rats are predominantly nocturnal animals, and in the wild live in underground burrows. This immediately suggests that the visual modality should be of lesser importance than in humans.

Indeed, the tactile sense of the vibrissae are assumed to be a very important sense to the rat, based on the relative size of the sensory cortices [134]. While experimental setups to provide individual whisker stimulation exist [135, 136], doing so in a manner consistent with an animal moving through a virtual environment is an ambitious task beyond the scope of this work. If the system is thus unable to provide realistic whisker stimulation, it should be designed so that the input derived from whisking is ideally uniform, or if not uniform at

least uncorrelated with anything in the virtual space.

A similarly important sense is olfaction, which is equally difficult to manipulate. This is because of the reality that while olfactometers provide a means to provide different odors in a controlled manner, there is significant delay between the opening of a valve and the presentation of the odor. This delay (often on the order of a second or more) is due to the limited rate of air flow between the olfactometer and the subject. Any attempt to provide odors consistent with an animal's position in a virtual environment therefore requires the ability to *predict* the animal's position a second or more in the future, which is exceedingly difficult for all but the simplest tasks. As with tactile input from the vibrissae then, the best course of action is to ensure there are no persistent correlations between odors and particular features of the virtual environment.

The vestibular system provides sensory information about acceleration and orientation in most mammals. Since the virtual reality system is designed to keep the animal in one place, it naturally suppresses vestibular input. If the manipulation of such input is desired, it can in principle be achieved by rotating the device so that the gravitational force is applied at an angle to the body, as is done in flight simulators. However, since one of the primary questions we hope to address is whether vestibular inputs are necessary for place cell firing in the hippocampus, our system does not include such manipulations. Such a rotation system, while possible in theory, is also likely to be mechanically challenging to construct, as it must be capable of very rapid rotations about multiple axes.

One of the modalities that can be manipulated with great precision in virtual reality is of course the visual sense. While its usefulness to rats in the wild may be smaller than that of the other senses, distal visual cues have been shown to exert great influence over place cell firing [68]. The rat's visual system is quite different from that of humans in at several important areas.

First, the eye lacks a fovea and while it contains both rods and cones the cones represent only about 1% of light sensitive cells [137]. Unlike humans the rat eye contains only short and medium wavelength color receptors, with peak sensitivity at 359nm and 510nm. Very

little sensitivity remains past 650nm [138], which is why rats on a reversed light/dark cycle are often housed in rooms with red lights. This has an important practical consequence in that virtual environments should be designed so that sufficient contrast and variation is achieved in the scene without the use of red colors.

Second, rat's possess an extremely large field of view. While exact estimates differ, it is accepted that the azimuthal field is at least 270° [139]. Only 76° of this view is binocular, so rats use motion parallax for depth perception [140]. It is therefore necessary to project visual stimuli all around the animal. Furthermore the depth of focus of the visual system is around 7cm [141]. This means that effectively the entire visual field must be simultaneously in focus.

Third, the regions of the retina with the greatest ganglion cell density at at the top of the retina, corresponding to the part of the field of view directly in front of and below the rat. This, together with the large field of view, suggests that it is important to provide visual stimuli as close to the rat as possible (a key shortcoming of existing systems, which provide stimuli only up to the edge of the spherical treadmill).

Finally, the visual acuity of the rat is only one cycle per degree [142]. By contrast human visual acuity is roughly 30 cycles per degree. This fact substantially reduces the need for visual complexity, as the system need only project one pixel per cycle. As a result, a resolution as small as 640 by 480 pixels provides more visual clarity than the rat can discern, (assuming the pixels are evenly spread across the field of view).

As nocturnal animals, the auditory sense is likely important to rats in the wild. Rats have a much larger hearing range than humans, starting around 200 Hz at the low end and going as high as 80 or 90 kHz at the high end [143] [144]. Care must thus be taken to ensure the experimental setup is not contaminated by ultrasound sources.

Rats also vocalization at a wide range of frequencies. Long vocalizations around 20 kHz are emitted during times of stress, including detecting predators [145], pain [146, 147], anticipation of pain [148] and others [149, 150]. Distress calls by infant rats fall in the 30 to

50 kHz range [151, 152]. Positive contexts, such as play [153] and reward anticipation [154] have also been shown to elicit high frequency vocalizations. This opens up the interesting possibility of providing auditory stimuli at lower frequencies and recording ultrasonic vocalizations to potentially assess stress or reward anticipation, although this is not something we pursue here. Providing auditory stimuli which mimics the natural vocalizations is another interesting possibility, but for simplicity is not pursued here.

Perhaps the most important characteristic of the rats auditory system for our purposes is the ability to localize audio sources. Auditory localization is done based on the difference in the signals detected by the two ears, together with the direction specific reflection of sound waves caused by the outer ear [155]. One would thus expect, based on the smaller distance between their ears, that rats would perform poorly compared to humans in sound localization tasks. This expectation has been confirmed experimentally: while humans can pinpoint sounds within 3° [156], localization acuity of rats is in the $9\text{-}12^\circ$ range [157, 158]. Given their poor localization ability, care must therefore be taken to make positional auditory stimuli as realistic as possible.

3.1.3 System requirements

Given the goals of the system and the capabilities of the rat's sensory mechanisms we can now play out the requirements for the virtual reality system. The system should:

- Display visual stimuli covering the entire field of view of the rat, including on the floor directly in front of and round the animal;
- The resolution of the projected visual stimuli must be at least one pixel per degree;
- Provide realistic positional auditory stimuli;
- Track and record the motion of the rat in two dimensions;
- Update the visual and auditory stimuli in a realistic manner according to the animal's motion;

- Be quiet enough not to interfere with auditory stimuli, preferably below 50dB;
- Detect reward checking behavior;
- Record the animal's position in the virtual environment in a manner that can be synchronized with electrophysiological recording;
- Be free of electrical noise in the range of interest to electrophysiology (below 20kHz), in particular have minimal 60Hz AC noise;
- Provide liquid rewards to the animal;
- Allow grooming and rearing behavior for animals that are not head fixed;
- Be easily extensible to allow head fixation (i.e. should not require a change in the animal's orientation to operate);
- Have a minimally complex mechanism for defining new virtual environments.

3.2 System design

3.2.1 Overview

The system is inspired by previous designs [132] but differs in several important areas. The rat is held in a harness attached to a hinge joint on top of a spherical ball which acts as a treadmill. The rat is thus free to rear and groom, but cannot rotate on top of the ball. Tasks requiring the rat to rotate in the virtual environment are accomplished by allowing the rat to rotate the ball underneath it.

The projection screen is cylindrical in shape, and closed at both the top and bottom (with a sufficient gap in the floor to allow the ball to protrude as necessary). A curved mirror is placed at the top of the screen, with a pocket projector suspended beneath it, as shown in figure 3.1. The visual stimuli thus cover a very large field of view.

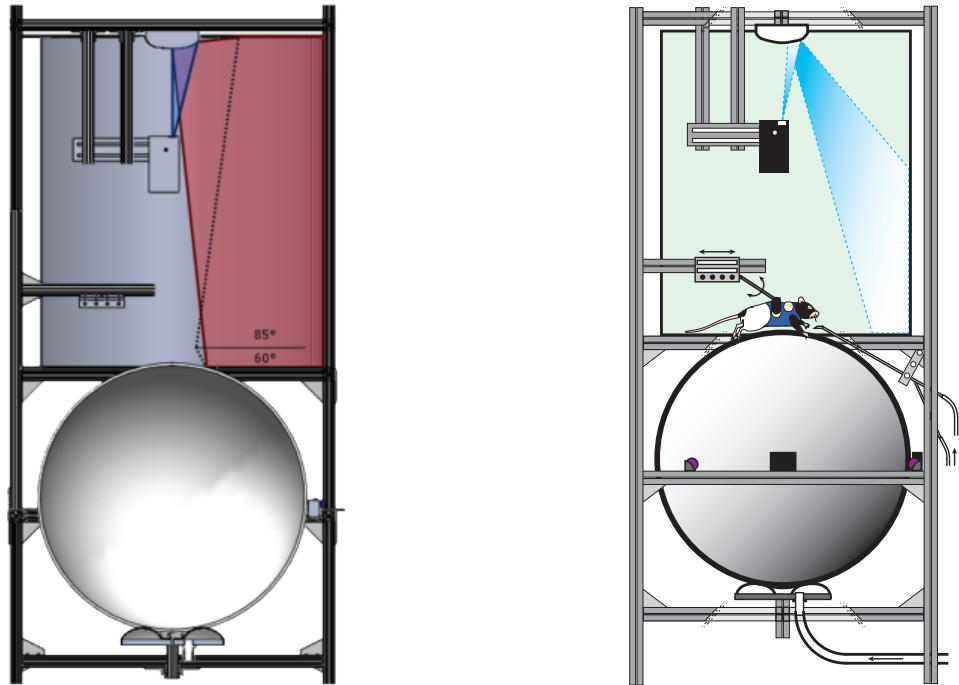


Figure 3.1: Schematic of the virtual reality system. The two angles indicate the vertical field of view above and below the horizontal covered by the projection system.

A small tube, which is used to dispense liquid reward, extends from the base of the screen in front of the rat. Seven speakers surround the frame and are used to produce realistic positional audio. The entire system is controlled by custom software which interfaces with the sensors and recording equipment via a micro controller (Atmega 8515, Amtel) and optionally synchronizes with the electrophysiology recording equipment by sending TTL frame numbers through a digital input output board (NI USB-6501, National Instruments).

3.2.2 Motion tracking

The rat is held atop a 24 inch diameter hollow Styrofoam sphere. To discourage chewing behavior, the sphere was coated with a thin layer of Foam Coat (Special Effects Supply Corporation, North Salt Lake, Utah). Unlike previous designs, the sphere is not purely suspended on a powerful jet of air, as such a system is extremely noisy. Instead, the sphere rests on an air cushion resembling an inverted hovercraft, which still allows for rotation about

all three principle axes with minimal friction.

The rotation of the Styrofoam sphere was detected by two laser sensors (ADNS-9500, Avago) mounted orthogonal to one another along the equator of the sphere. A micro controller queried each sensor every millisecond, and stored cumulative rotation data. The micro controller in turn was connected to the computer via a serial to USB interface, and the computer polled the micro controller for rotation data on every display frame. By directly controlling the laser sensors (rather than simply using an optical mouse as is done in other setups) we achieved a one-to-one mapping of treadmill rotation distances to virtual environment distances. The accuracy of the rotation sensors was 1 ± 0.01 reported rotations per true rotation of the sphere.

3.2.3 Visual stimuli

There are several components that work together to produce visual stimuli that accurately depict the virtual environment. As discussed above, the stimuli are projected onto a cylindrical screen which covers a large field of view. This is made possible by projecting on a convex shaped mirror, which reflects onto the entire projection screen. The screen was 75cm tall with a 68cm diameter, and manufactured by Hollywood Lamp & Shade, Hollywood, CA.

The geometry of the reflecting mirror is calculated numerically using simple optical principles (angle of incidence is equal to angle of reflection) to produce a surface which distributes the pixels from the micro-projector evenly across the screen. Once the geometry of the mirror has been calculated, it is machined from a solid aluminum block and polished until sufficiently smooth.

The software must then compute the inverse distortions of the visual stimuli needed to counteract the effect of the curved mirror. This is achieved by maintaining by imaging the virtual scene ‘reflected’ in a virtual copy of the mirror. This reflection mapping is done using a cube map [159], a standard technique in computer graphics.

Briefly, a 3D mesh of the mirror surface is created using the vertex coordinates calculated

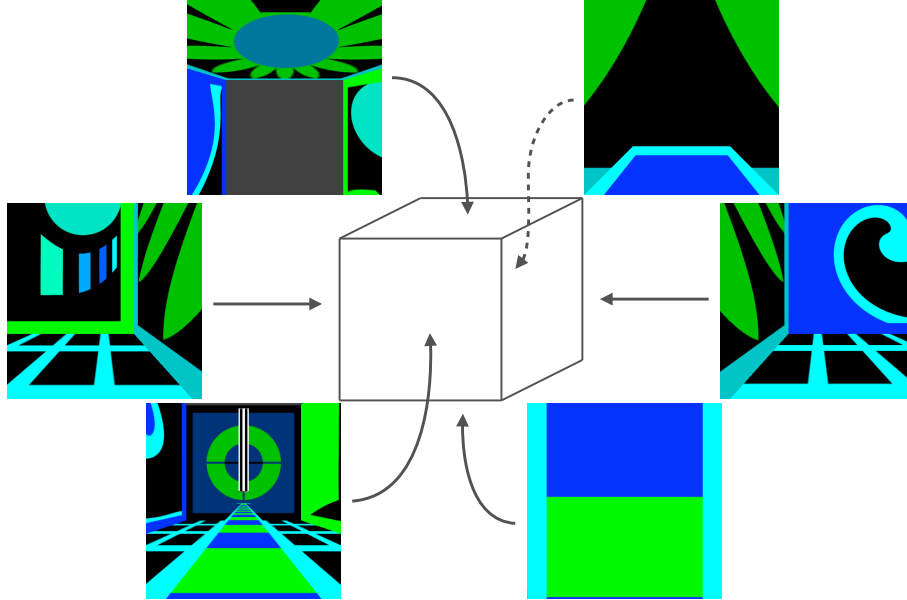


Figure 3.2: A sample cube map of the virtual linear track environment.

previously. For each frame to be drawn by the rendering software, six orthogonal views of the virtual environment are calculated from the current position of the rat within the virtual environment (see figure 3.2). Each of these views has a 90° field of view, and together represent an approximation of the environment as a cube (optically at infinity).

Every vertex of the mirror mesh is assigned a cubic texture coordinate, which is calculated numerically by the mirror surface generation algorithm. For each vertex of the mesh a ray is defined from the position of the rat to the point on the cylindrical screen where pixels hitting that vertex would be projected. This ray is then extended and the coordinate of its intersection with a bounding cube provides the cubic texture coordinate for that vertex (see figure 3.3). Note that while the cube map representing the environment must be recalculated on every frame, the cubic texture coordinates of the mirror need only be computed once.

Finally the virtual mirror mesh is imaged, and this distorted image is projected onto the real mirror at a resolution of 800×600 pixels using a micro-projector (MPro160, 3M) mounted below the mirror in the center of the screen. Using a micro-projector has two important advantages. First, the projector itself is very small so it does not block projection of visual stimuli up to 1cm of the rat. Second, it can be operating on (DC) battery power,

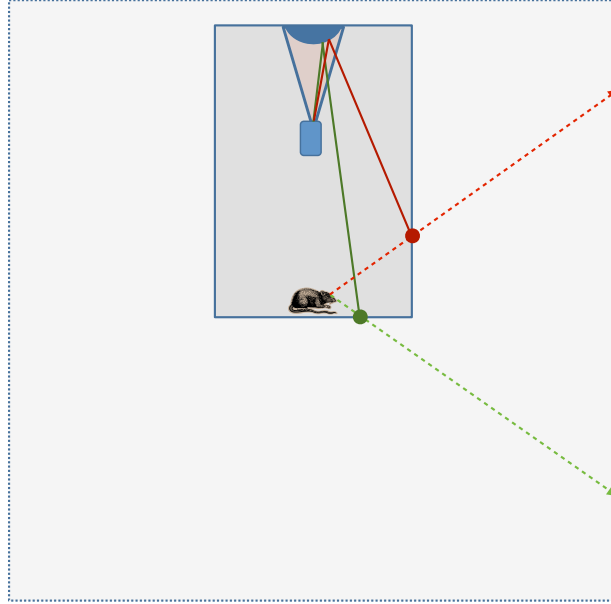


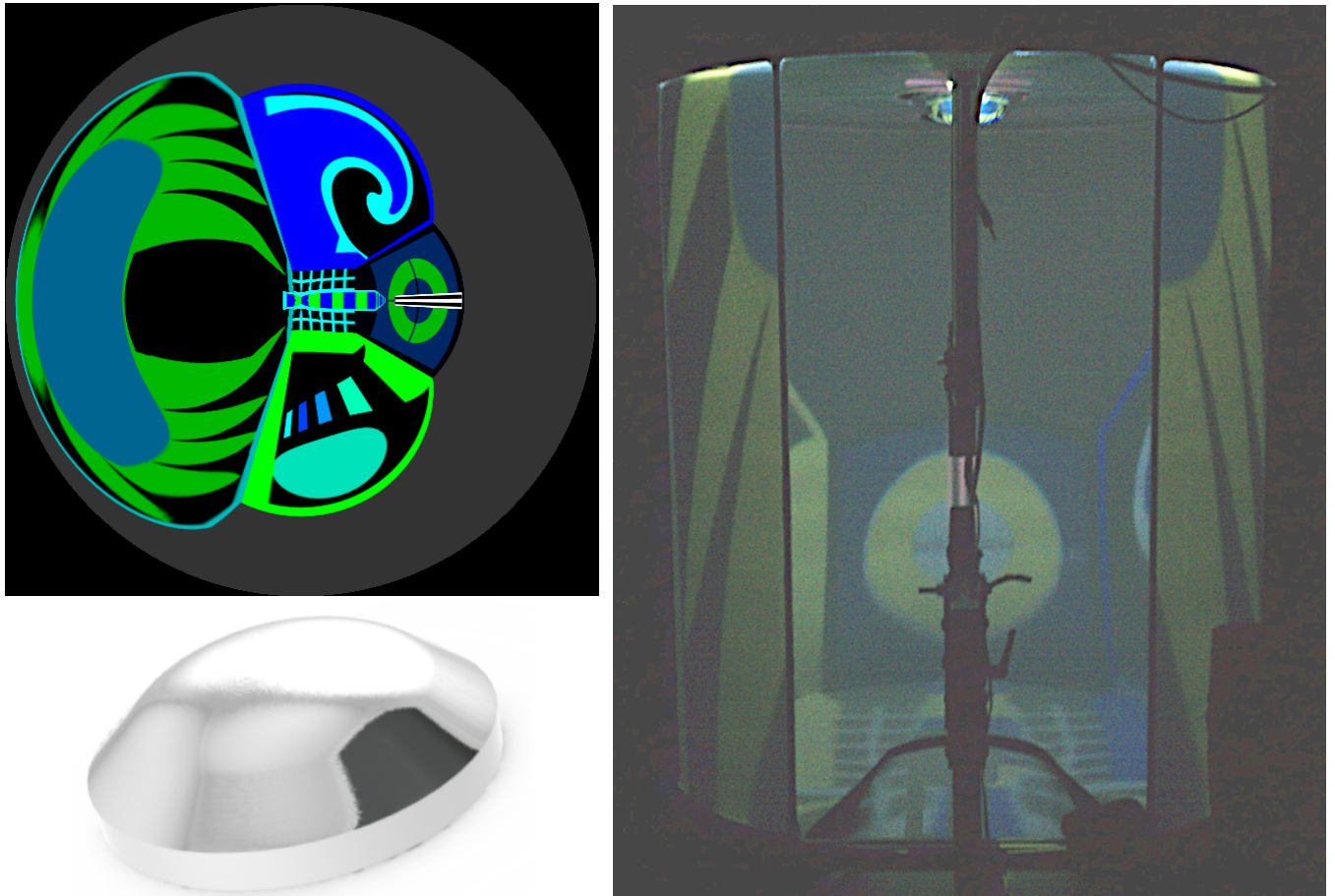
Figure 3.3: Two sample rays demonstrate how cube map texture coordinates are computed for each vertex on the mirror. The dark rectangle represents the physical screen geometry, while the lighter square is the virtual cube map.

removing the need for any 60Hz power lines, which can cause substantial electrical interference during electrophysiology (the video cables must necessarily carry electrical signals, but these are at much higher frequency ranges than are of interest). The mirror shape, together with a sample distorted image and the resulting projection are shown in figure 3.4a and 3.4b.

3.2.4 Auditory stimuli

Auditory stimuli were provided using seven speakers (SS-B1000, Sony) placed around the screen in a hexagonal distribution, with the seventh speaker position as a center speaker. The use of a thin fabric projection screen avoided acoustic distortions due to the screen geometry. The entire system was housed within a 3x3m acoustically shielded room to minimize external noise concerns.

Positional audio was generated by the software using the OpenAL sound programming



(a) The distorted image produced by the cube (b) Projected the distorted image onto the mir-
 map in figure 3.2, and the projection mirror. ror produces a scene with realistic perspective.

Figure 3.4: The distorted visual projection.

library, and the Rapture3D OpenAL implementation¹. The Rapture3D system allows the use of higher order ambisonic sound fields which much more accurately reproduce positional audio than simple surround sound systems. Audio was transmitted via HDMI from the computer to an AV Receiver (STRDH520, Sony) and from there to the speakers.

3.2.5 Reward checking and delivery

Liquid reward (typically a 10% sucrose solution) is dispensed through a stainless steel tube mounted between the treadmill and the floor of the projection screen (see figure 3.1). To prevent unconsumed sugar solution from contaminating the treadmill a larger stainless steel drainage tube surrounds the reward tube. The flow of liquid through the tube is controlled in the software by opening or closing a solenoid valve (003-0141-900, Parker) attached to a reservoir. Reward is typically dispensed in short pulses of 400ms, which allows the formation of droplets at the end of the reward tube, and can be activated by any of the trigger mechanisms described in section 3.2.6

Reward checking behavior were detected using one of several techniques. When electrophysiological recordings are not required, a capacitive touch circuit (AT42QT1010, Amtel), connected to the reward tube, was polled by the same micro controller responsible for monitoring the motion sensors. The operating frequency of the capacitive touch circuit is in the range of interest to electrophysiology, which makes it unsuitable for experiments where these recordings are desired.

An alternative detection mechanism is based on the junction potential created between the rat and the reward type when licking [160]. By recording the potential on the reward tube through the electrophysiology data acquisition system (referenced to the animal ground signal) a signal is obtained from which licking behavior can be extracted if necessary (see figure 3.5). This approach is typically less reliable than the capacitive touch circuit, and only works if a ground signal is available (i.e. for animals where a microdrive and ground screw have been implanted), but is free of the high frequency electrical noise of the capacitive

¹Rapture3D, version 2.5, Blue Ripple Sound Ltd, <http://www.blueripplesound.com>

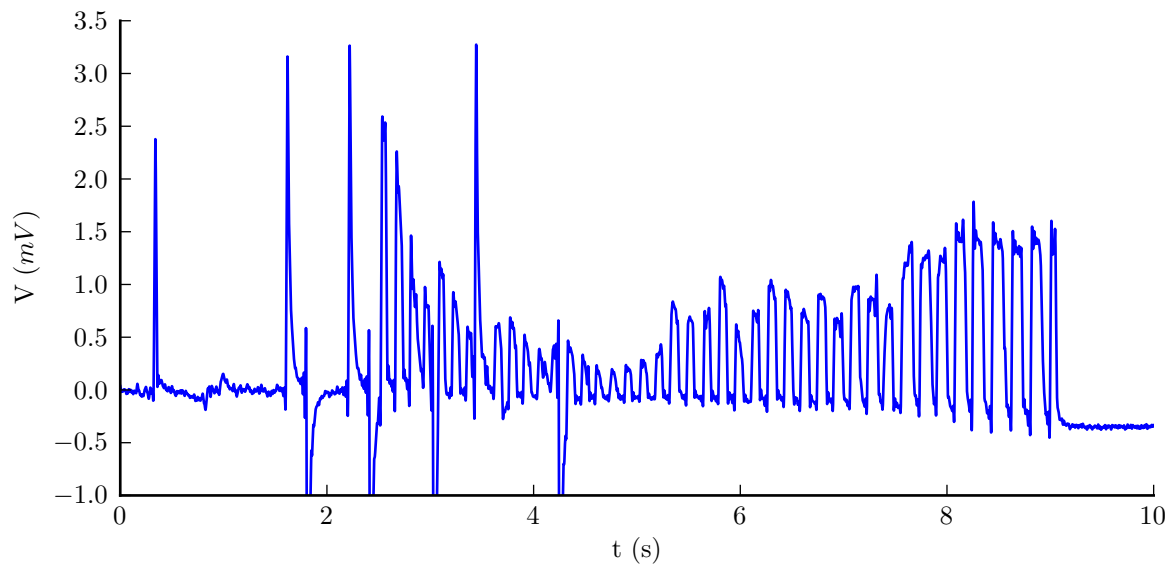


Figure 3.5: Potential difference between the skull ground electrode and the reward tube during lick behavior demonstrates the junction potential based reward checking system. Both the valve opening and closing and the individual licks of the reward tube are clearly visible.

touch approach.

3.2.6 Control software

The control software for the virtual reality system was written in C++ and tested and run on a Windows 7 platform, but requires only minor adjustments to run on a Linux platform. The graphical subsystem is built using the Ogre3D library² and the positional audio subsystem using the OpenAL library³, both of which are cross platform. The NI USB-6501 is controlled using the NI-DAQmx API⁴. The only platform specific dependency is the micro controller interface, which is essentially just serial port I/O, and should be easily adaptable to other platforms.

To facilitate easy creation of virtual environments the software includes a parser for an XML based track file format. The track file specifies the geometry type (linear, planar, spherical or cylindrical), together with a collection of entities. Where appropriate the position of an entity (such as a visual stimulus or a positional audio source) is defined using two generalized coordinates: (x, y) for planar tracks, (θ, ϕ) for spherical tracks, and so on. Environmental entities available include simple geometric primitives, complex Blender meshes, positional audio sources, and trigger regions.

The task logic is created using a trigger system. Triggers can be defined based on either a timer or entry into or exit from trigger zones. Once activated these triggers are then used to activate dynamic elements in the track. Some of the dynamic elements available include reward dispensers; audio playback; moving scene elements; hiding or showing visual elements; etc. By chaining together these trigger elements fairly complex behavior can be elicited, while still being easy to edit and maintain.

Once the track file is selected and initial setup and configuration are done, the system iterates over a main event loop which continues until interrupted by the operator. To avoid

²Open Graphics Rendering Engine, version 1.6, <http://www.ogre3d.org>

³Open Audio Library, version 2.0.7.0, Creative Technology Ltd., <http://www.openal.org>

⁴NI-DAQmx, National Instruments Corporation, version 9.7

flicker artifacts due to screen tearing, the main loop is synchronized to the projector redraw rate. Each iteration of the main loop consists of several steps:

1. The micro controller is polled for the current state of the lick detector and the cumulative treadmill rotation since the last frame.
2. Position and orientation in the virtual world is updated based on the treadmill rotation after enforcing boundary checks for the environment.
3. Position and timer based triggers are activated as appropriate.
4. The frame counter is incremented, and its current value transmitted to the digital input TTL port on the electrophysiology data acquisition system.
5. The current frame number, position, orientation, lick detector state and treadmill rotation deltas are written to disk.
6. Trigger activation messages, if any, are written to disk.
7. The visual scene is updated and displayed.

In the following section we will examine some of the virtual environments created using this track editing system, together with brief summaries of animal performance in each environment.

3.3 Virtual environments

We now examine some of the virtual environments and tasks created using the track editing system described in section 3.2.6. We identify three categories of tasks: those based on navigation directly to a particular *beacon* stimulus; those based on navigation to an unmarked location based on distal stimuli; and those involving particular targeted manipulation of stimuli.

3.3.1 Audio-visual beacon orientation

A training task was developed to acclimatize the rats to turning on the treadmill, and to task their orientation acuity under different cue conditions. The rats were required to rotate the treadmill so that an audiovisual, visual or audio beacon stimulus was within a 60° arc in front of them. Non azimuthal rotation of the treadmill was ignored, effectively fixing the ‘virtual rat’ in place but allowing rotations. No stimuli other than the beacon were provided. The visual beacon consisted of a striped black and white vertical pillar. The auditory beacon was a complex chirp consisting of a 5-10 kHz sound pulse that repeated fifteen times a second. The audiovisual beacon was a combination of both of these.

The rat started every trial at a random orientation relative to the beacon, and once the rat successfully rotated to bring the beacon directly in front of him five reward pulses (of 400ms, as described in section 3.2.5). If the rat rotated the beacon away from the correct orientation while the reward was being dispensed the reward ceased, creating an incentive to maintain the correct heading and avoid spuriously spinning the treadmill. Once the reward was dispensed the stimuli were blacked out (i.e. auditory stimuli muted, and visual stimuli removed) for two seconds. During this blackout period rotations of the treadmill were ignored, and the rats orientation rotated randomly, ending the trial. The three trial types (audio, visual, audiovisual) were randomly interspersed during a session.

On the first day of exposure to the task a reward tone (see section 3.2.5) was coupled with the valve opening to provide clear feedback on when the goal was achieved. On sessions thereafter the reward tone was removed to avoid a strategy of simply spinning the treadmill until a reward tone was played.

3.3.2 Random foraging task

A set of training tasks to teach rats to manipulated the treadmill in a two dimensional environment were developed which closely mirror random foraging protocols used in place cell studies in the real world. The rat was placed on top a virtual table shaped like an

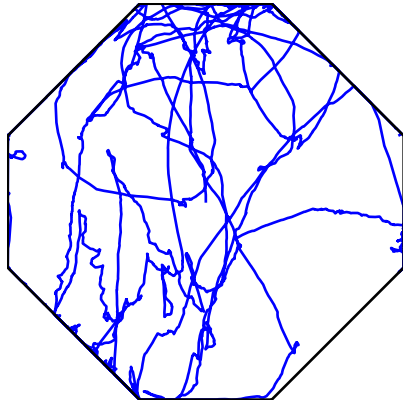
octagon, either 1.5m or 1m in radius depending on the variation. Visual stimuli were placed on the table, as well as the floor (150cm below the table) and the room walls to mimic the perspective variations present in the real world.

The rat obtained reward by moving toward any of several (either five, three, or one depending on the difficulty) visual beacons which consisted of a vertical pillar hanging above the table, together with a white circle on the table surface. Reward was dispensed up to five 400ms pulses, or until the rat left the reward area, whichever happened first. Once reward dispensation stopped, the pillar, circle and reward region were moved to a random location on the table. A shaping procedure was used where a naive rat would start on the large table with five reward sites, followed by the large table with three reward sites, then the small table with two reward sites, and finally the small table with a single reward site. This sequence of training tasks was the first exposure rats were given to virtual environments once they had been habituated to the harness and reward tube, and performance typically reached asymptotic levels within six sessions.

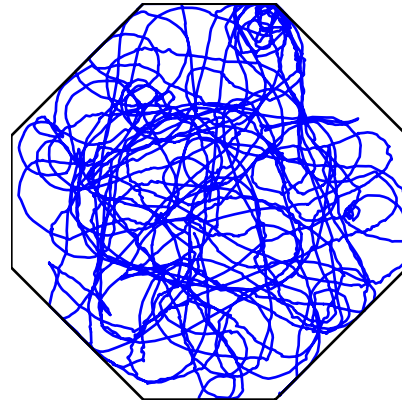
3.3.3 Linear track

The linear track is the protocol employed by a plethora of place cell studies, and was similarly important in the virtual reality system. Multiple variations were developed, but fundamentally the aim was the same in each case. Motion of the rat in the virtual environment was constrained to either to forward/backward or rotational degrees of freedom. The animal would start at one end of a narrow linear track, and would be rewarded for moving to the opposite end of the track.

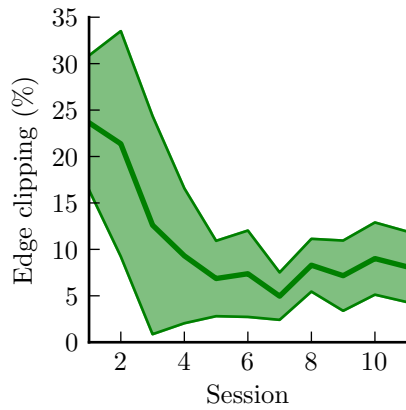
To mirror the perspective variation observed in the real world, the track was typically placed 150cm above the floor of the virtual room, and included salient visual stimuli on each of the four walls, the floor of the room, and the linear track itself. Upon reaching the end of the track, the rat could either manually rotate the environment for the return journey, or could be instantaneously rotated depending on the variation. This linear track formed the



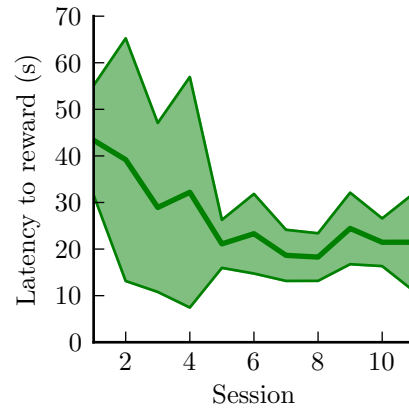
(a) Trajectory from session 1.



(b) Trajectory from session 9.



(c) Edge clipping.



(d) Reward latency.

Figure 3.6: Rat performance on the random foraging task. Asymptotic performance was achieved within six sessions on both the edge clipping and reward latency measures. Environment coverage also improved markedly from the first session.

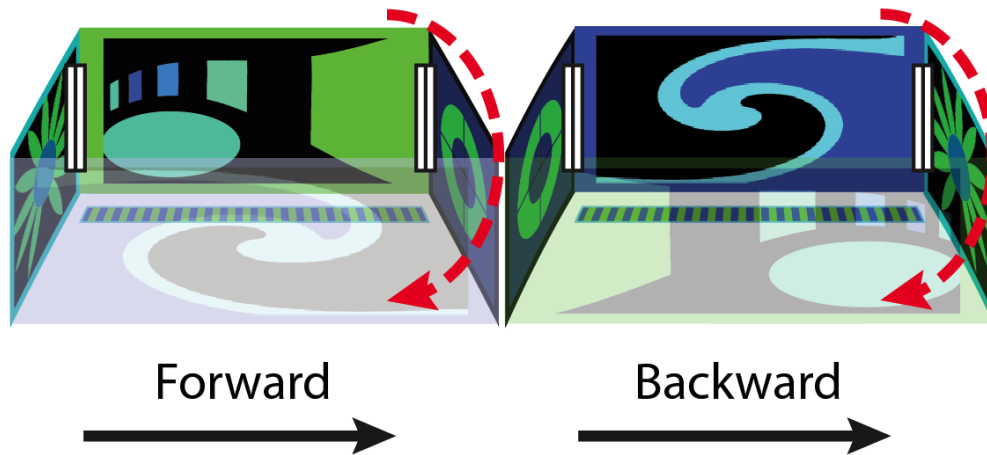


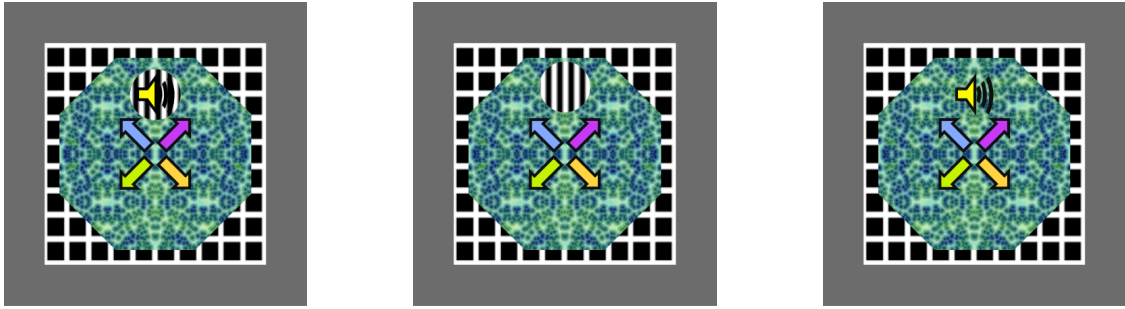
Figure 3.7: Schematic of the virtual linear track task. Upon reaching the end of the track, the rats orientation in the virtual environment is automatically rotated by 180 °.

basis for the electrophysiology experiments described in later chapters, and is depicted in figure 3.7.

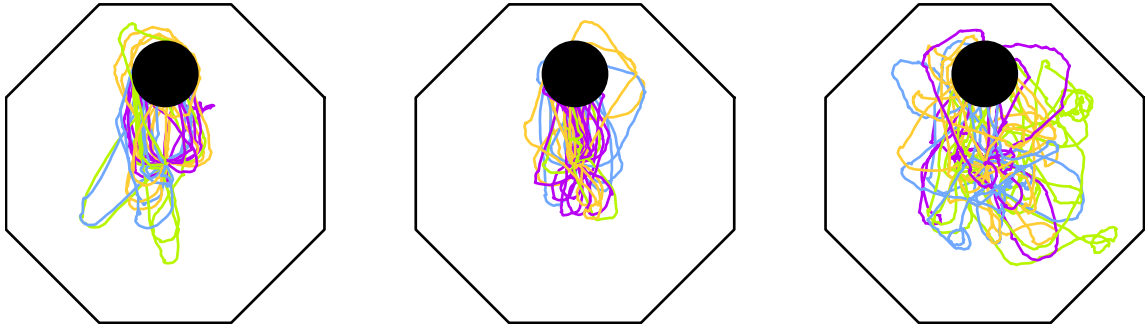
A variant of this track was used to test the rats ability to navigate to a particular position along the track. In these variations the reward was dispensed not at the end of the track, but far enough from the track end that the animal could overshoot the reward if it were simply running forward without heeding the stimuli presented. As with the orientation experiment rats proved to be more accurate with visual stimuli indicating the reward location than with purely auditory stimuli.

3.3.4 Two dimensional beacon navigation

As a more complex variant of the linear track experiments described above, this task was designed to measure the spatial accuracy with which rats could move toward a particular beacon stimulus. As in the orientation task, the beacon could be either a visual pillar, and auditory chirp, or both. The geometry of the environment was the same as in the foraging task (an octagonal table). For each trial, rats started at the center of the table at a random orientation. Reward was dispensed once they navigated to within 25cm of the beacon, after

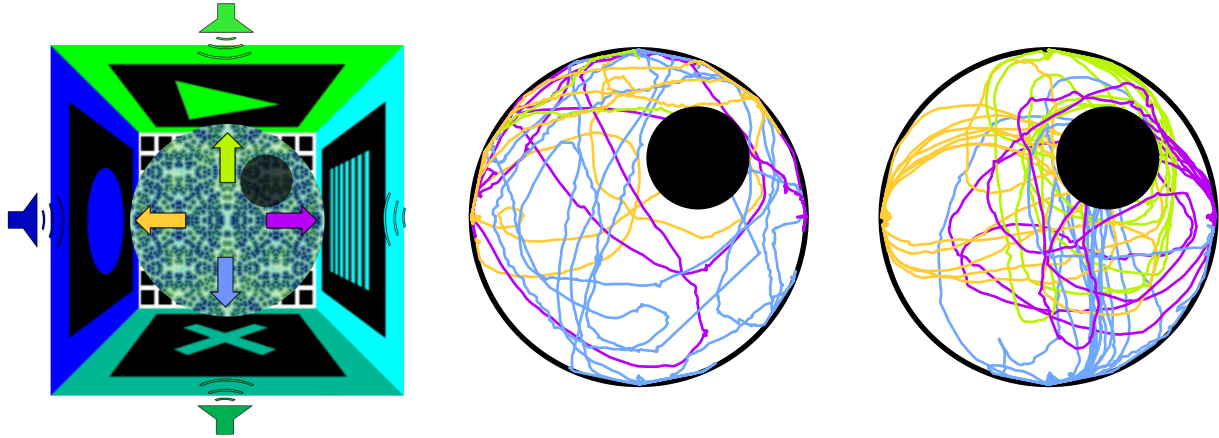


(a) Top down schematic of the audiovisual beacon task. (b) Top down schematic of the visual beacon task. (c) Top down schematic of the audio beacon task.



(d) Trajectories from a rat in the audiovisual beacon task. (e) Trajectories from a rat in the visual beacon task. (f) Trajectories from a rat in the audio beacon task.

Figure 3.8: Two dimensional audiovisual beacon navigation task. The rat starts in the center of the table, at an orientation chosen randomly from a set of four possible orientations. The location of the reward site is marked by either a visual beacon, and auditory beacon, or both.



(a) Top down schematic of the virtual environment. (b) Trajectories from a rat's first session on the task. (c) Trajectories from the sixth session of the same rat.

Figure 3.9: Spatial navigation task based on the Morris water maze. Rats typically reached asymptotic performance in five or six sessions.

which a blackout was applied and the rat instantaneously moved back to the center of the table, again at a random orientation. As in other tasks rats demonstrated greater accuracy in navigating based on visual stimuli than audio stimuli, although they were still able to perform the task when auditory stimuli were presented (see figure 3.8).

3.3.5 Spatial navigation task

Having examined rats ability to navigate toward particular beacons, we developed a task to test their ability to navigate toward an unmarked location based on distal stimuli, modeled after the Morris water maze [161].

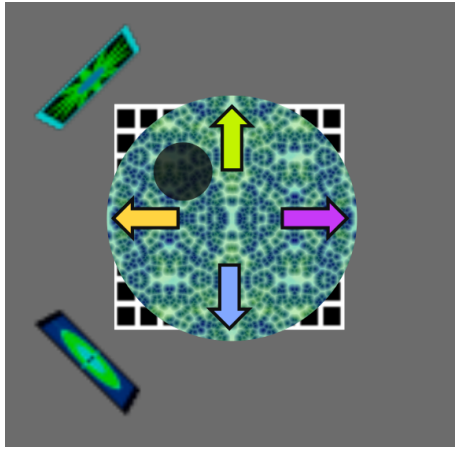
The environment consisted of a circular table (with a one meter radius) centered in a room with distinct visual cues on each wall, and distinct positional audio cues at the center of each wall (see figure 3.9a). The table was 125cm above the floor, and the room was square with 4.5 meter sides.

Each trial began with the rat located at one of four random start locations along the

edge of the table, facing away from the table center. The northeast quadrant of the table contained an unmarked reward zone (30cm radius during initial training, 20cm radius in final test version). Upon entry to the reward zone reward was dispensed up to five pulses as discussed previously, with the modification that the previously unmarked reward zone was marked with a white circle while reward was dispensed to provide immediate feedback on task completion. After reward dispensation finished, the environment was blacked out for two seconds and the rat instantaneously moved to one of the four starting locations. The rats successfully learned the task within a comparable time to that of the original water maze (five sessions). Once asymptotic performance was achieved, a probe trial was conducted in which the reward zone was removed, and the rat freely explored the environment for four minutes. During this probe trial rats spent significantly more time in the quadrant previously associated with reward.

Having demonstrated that rats can successfully perform spatial navigation tasks in the presence of audiovisual stimuli, we designed a variation of the task wherein all visual or auditory cues were removed in blocks of 8 trials (i.e. 8 trials with all cues, 8 trials with only audio cues, 8 trials with only visual cues). These three blocks repeated twice in random order. Interestingly, the rats were unable to perform the spatial navigation task in the presence of only auditory cues, but their reward checking behavior exhibited spatial information even in the audio only cue condition.

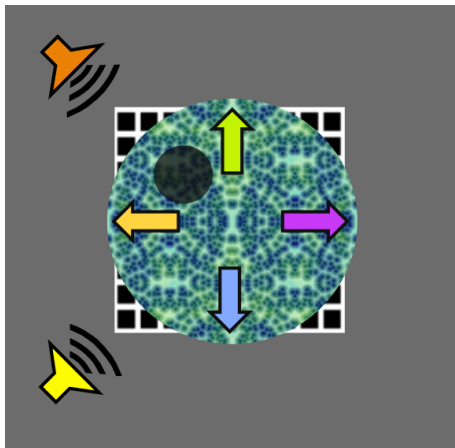
To account for the possibility that the rats may simply have learned to ignore the audio cue in the joint cue condition, and test if spatial learning is possible based only on distal auditory cues we designed two more versions of the navigation task. In each case two stimuli were used (either purely auditory or purely visual) in a layout (see figures 3.10a and 3.10c) based on a previous study which provided evidence of spatial navigation based purely on distal auditory cues [162]. This task failed to show evidence of spatial learning in the auditory cue condition, with rats adopting a strategy of searching at a fixed distance from the edge of the table (figure 3.10d).



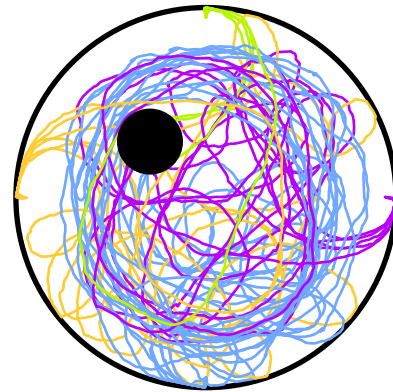
(a) Top down schematic of the spatial navigation task with two visual stimuli.



(b) Trajectories from a single session in the visual task.



(c) Top down schematic of the spatial navigation task with two auditory stimuli.



(d) Trajectories from a single session in the audio task.

Figure 3.10: Spatial navigation task based on the Morris water maze with purely auditory or visual cues. Rats were unable to navigate based on auditory cues, instead adopting a circling search strategy.

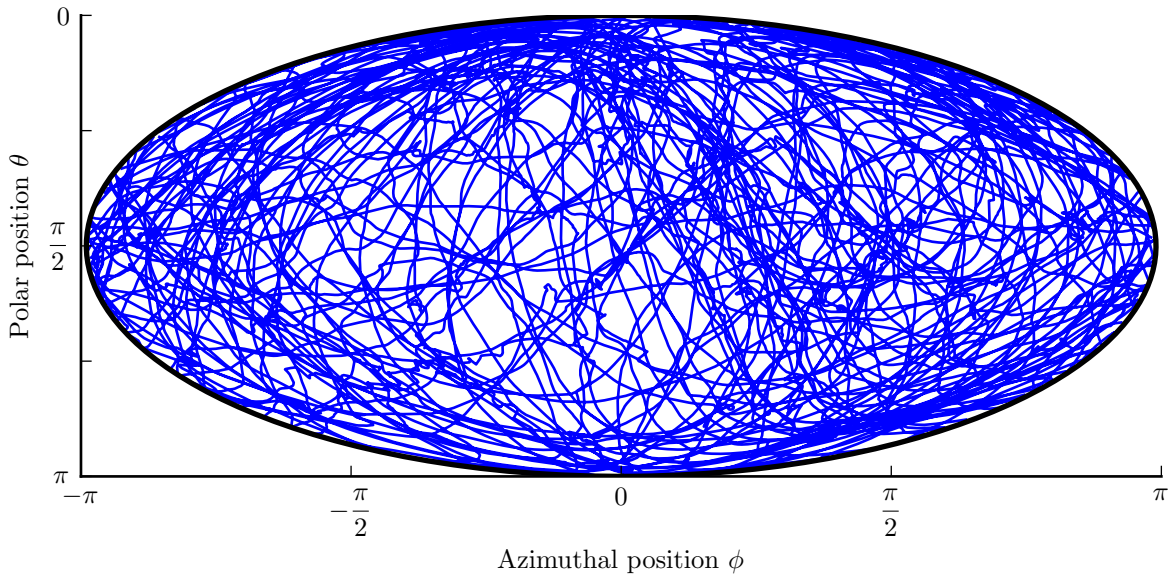


Figure 3.11: Sample trajectory of a rat in the spherical foraging task, depicted using the Mollweide map projection.

3.3.6 Foraging in spherical geometry

To design an environment without boundaries we implemented a spherical geometry track. The virtual rat is constrained to move on the surface of a sphere of radius 31cm (for an effective surface area of 1.2m^2 , comparable to the one meter square open field environments often used in place and grid cell studies). As with the planar foraging task the rat is rewarded for reaching a reward site indicated by a vertical pillar. When reward dispensation is finished, the reward site and accompanying visual cue is moved to one of 20 predefined locations evenly spread across the surface of the sphere. To provide visual landmarks 16 visual stimuli, mostly simple geometric shapes, are suspended in air above the sphere. Trajectories from a rat performing the spherical foraging task are depicted in figure 3.11.

3.3.7 Strobed linear navigation

Two variations of the linear track were designed where all stimuli are temporarily removed from the environment. The first environment is a linear track navigation task based on

distal visual cues in which stimuli are removed on six out of every seven frames (seven frames roughly correspond to the period of the hippocampal theta rhythm). The second environment is a regular linear track where all visual cues are removed whenever the rat enters the two regions of the track (corresponding to roughly 40% of the track length). Results from single unit data are presented in a later chapter.

CHAPTER 4

Place cells on the virtual linear track

4.1 Introduction

The linear track is the canonical experimental protocol for much of the literature on hippocampal physiology. Many important findings in the study of place cells were based on linear track experiments (or variations thereof), including phase precession [25], place field plasticity and asymmetric expansion [29], sequence replay [34], and others. It is therefore a natural choice for initial studies in virtual environments.

The virtual linear track provides the opportunity to test the contribution of non-visual stimuli, including vestibular and olfactory cues, to many results from the real linear track. Moreover, knowledge of the activity of place cells on a virtual linear tracks would provide a baseline against which to gauge results from more complicated tasks, which may involve manipulation of the virtual scene in ways that lack any real world analogue, and would thus be difficult to interpret independently. Place cells have been measured in VR in head fixed mice [67, 133], and are thought to be similar in VR and RW but this has not been tested

For these reasons, we performed hippocampal recordings from six rats in a virtual linear track. Four of the rats were also run on a real world linear track with comparable visual stimuli for comparison. The details and results of these experiments are presented in the remainder of this chapter.



(a) A top down schematic of the environment.



(b) A rat performing the task.

Figure 4.1: The environment used for electrophysiological recording in a virtual linear track.

4.2 Methods

4.2.1 Real and virtual environments

As described in section 3.3.3, the linear track environment constrains the animal's motion in the virtual space along one dimension, and rewards are dispensed at alternating ends of the track.

The virtual environment consisted of a 220×10 cm linear track suspended 1m above the floor and centered in a $3 \times 3 \times 3$ m room. Optic flow was provided along the length of the track by alternating 5cm wide green and blue strips on the track surface. A white grid (30cm spacing) on the black floor provided parallax-based depth perception. Distinct distal visual cues covered all 4 walls and provided the only spatially informative stimuli in the VR (figures 4.1a and 4.1b). To maximize the number of trials run in a session, the visual scene was instantaneously rotated by 180° when the rats reached the end of the track.

In RW, rats ran back and forth on a 220×6 cm linear track that was placed 80cm above the floor. The track was surrounded by four 3×3 m curtains that extended from floor to

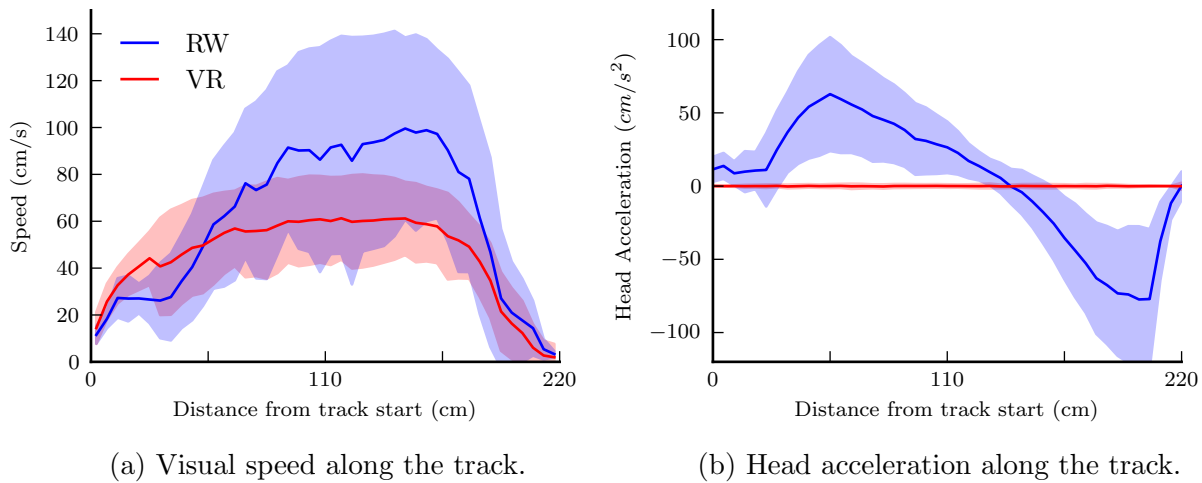


Figure 4.2: Speed profiles along the track were comparable in RW and VR, although slightly slower in VR. In contrast, head acceleration (and thus vestibular cues) were effectively eliminated in VR.

ceiling. The same stimuli on the walls in the virtual room were printed on the curtains, to ensure that distal visual cues in RW were very similar to those in RW. The same reward protocol (sugar water coupled with a tone) was employed in both VR and RW.

All experiments were conducted in identical acoustically- and EMF-shielded rooms. In both RW and VR four LEDs mounted on top of the drive were used to track the rats' head position at a sampling rate of 70Hz. Rats reliably learned to come to a stop at the end of the VR track, while their speed was somewhat lower in VR (figure 4.2a). Head acceleration was effectively eliminated in VR (figure 4.2b).

4.2.2 Subjects and training

A trial was defined as one complete traversal of the track, from one of the other, and back to the original position. In the virtual linear track rats were run for fifteen trials, after which some manipulations of the environment were performed. Data after the fifteenth trial were thus not included in the present analysis. In the real world, rats ran many trials, but for

consistency only the first fifteen trials were included in the analysis.

Six adult male Long-Evans rats (approximately 3.5 months old at the start of training) were individually housed on a 12 hour light/dark cycle. Animals were food restricted (15-20 grams of food per day) to maintain body weight. Animals were allowed to access a restricted amount of water (25-35 ml of water per day) after the behavioral session to maintain motivation. All experimental procedures were approved by the UCLA Chancellor's Animal Research Committee and were conducted in accordance with NIH guidelines.

After habituation to the harness and virtual reality system, animals were trained to run back and forth in a virtual linear track with the same dimensions as those described above, but with different visual stimuli. This was done to control for the amount of experience on the final version of the task. Typical training time for a naive rat was around four weeks in VR. Due to the relatively short training period needed in the real world, rats were trained in the same RW environment that was used for the final experiment.

In addition to the standard experiment outlined above, we performed two additional controls. The first was designed to assess whether the visual pillar which represented the reward location, which was the same in both travel directions, affected the effects observed. Two rats were run on a variations of the task with the pillar cue removed at either one, or both ends of the track. The second control tested the role of the passive scene reversal at the ends of the track, and involved two rats performing a variation of the task where active turning of the spherical treadmill was required to rotate the virtual environment.

Before and after each task recording session in VR and RW an hour-long baseline session was recorded to ensure stability of units. During baseline sessions, rats were allowed to rest in a box outside the task apparatus.

By the time the first place cell was detected (3 to 5 weeks after surgery, see section 4.2.3 below), rats were fully habituated to run the VR and RW tasks with their implant. From this point on, rats ran the VR task in the final environment as described above. At the time of recording, the rats had experienced both the RW and VR environments for at least one

week.

4.2.3 Surgery and electrophysiology

Rats showing sufficient performance in the VR task were implanted with 25-30g drives containing up to 22 independently adjustable tetrodes (13m nichrome wires) positioned over both dorsal CA1 areas (-4.0mm A.P., 2.4mm M.L. relative to bregma). Surgery was performed under isoflurane anesthesia and heart rate, breathing rate, and body temperature were continuously monitored. Analgesia was achieved by using Lidocaine (0.5mg/kg, sc) and Buprenorphine (0.03mg/kg, ip). Two 2mm-diameter craniotomies were drilled using custom software and a CNC device with a precision of 25 μ m in all 3 dimensions. Dura mater was removed and the drive was lowered until the cannulae were 100 μ m above the surface of the neocortex. The implant was anchored to the skull with 7-9 skull screws and dental cement. The occipital skull screw was used as ground for recording. Rats were administered 40mg sulfamethoxazole and 8mg trimethoprim in drinking water and 10mg/kg carprofen (Rimadyl bacon-flavored pellets) one day prior to surgery and for at least 10 days during recovery.

Tetrodes were lowered gradually after surgery into the hippocampus and allowed to stabilize above the CA1 hippocampal subregion. Positioning of the electrodes in CA1 was confirmed through the presence of sharpwave ripples during recordings, and through histology after experiments were completed (figure 4.3).

Signals from each tetrode were acquired by one of four 27-channel headstages, digitized at either 32kHz or 40kHz, bandpass-filtered between 0.1Hz and 9kHz, and recorded continuously. Spikes were extracted off-line and sorting was performed using a combination of the algorithm discussed in 2.4.2 and manual sorting 2.4.3.

In total, we recorded 106, 62, 55, 136, and 73 track active cells in the five rats in VR, and 125, 72, 22 and 21 track active cells in the four rats in RW.

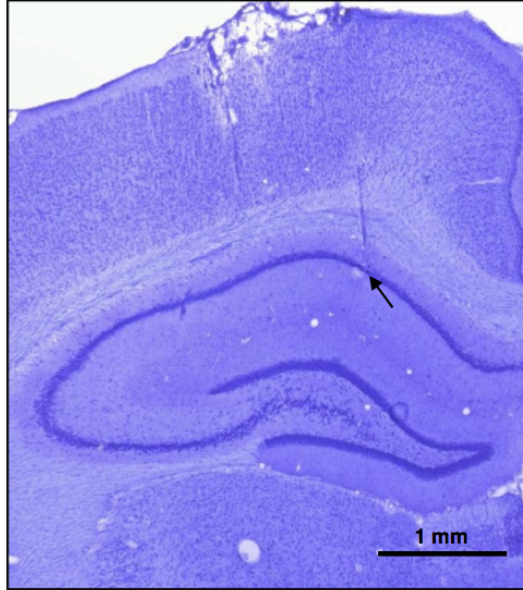


Figure 4.3: Histology micrograph shows a tetrode track ending in CA1. Arrow indicates the tetrode tip. Scale bar: 1mm.

4.3 Quantifying selective activity

Meaningful quantification of place cell firing properties require the introduction and precise definition of two constructs, the ratemap and place field.

Since the activity of place cells on a linear track can be different in the two opposing running directions, the animal's position was linearized so that the linearized position x starts from zero, and increases to $2L$ (for a track of length L) at the end of the trial. Firing activity during running periods and stationary periods were considered separately.

4.3.1 Ratemaps

The spatial firing ratemap $\lambda(x)$ provides an estimate of the firing rate of the cell at the linearized position x . A simple way to estimate the ratemap $\lambda(x)$ of a single unit is to bin both the animal's position data (yielding an occupancy histogram) and the position at the time of each spike (a spike count histogram), and then simply dividing the latter by the former.

If some smoothing of the ratemap is desirable (which is usually the case), these histograms can be smoothed by convolution with a Gaussian kernel. For reasonable values of the bin size δ_x and the smoothing kernel width σ_x metrics computed from $\lambda(x)$ are typically fairly insensitive to the exact value of these parameters, but the potential dependence on the parameterization should be kept in mind.

A more rigorous approach is afforded by the point process modeling framework [163], which provides a means to compute the likelihood of a ratemap model. Briefly, time is discretized into narrow bins of width δ (typically 1ms) with centers $t_i, i = 1 \dots T$. The spike train of a cell can then be represented as a binary vector $Y_i \in 0, 1$, with unit value in each bin where a spike occurred. Since a spike waveform recording is typically at least 1ms wide, there cannot be more than one spike within a 1ms time bin. The ratemap can be modeled in an appropriate manner, typically an expansion of basis functions such as polynomials or splines. Let the parameters of the model be $a_1 \dots a_M$, and use the notation $\hat{\lambda}_{\mathbf{a}}(x)$ for the ratemap model.

By treating each time bin as an independent Bernoulli trial with a probability of a spike occurring $P_i(\mathbf{a}) = \hat{\lambda}_{\mathbf{a}}(x(t_i))\delta$, we can calculate the likelihood of the observed spike train as a function of the model parameters:

$$\mathcal{L}(a_1, \dots, a_M) = \prod_{i=1}^T [P_i(\mathbf{a})]^{Y_i} [1 - P_i(\mathbf{a})]^{1-Y_i} \quad (4.1)$$

and hence the log likelihood:

$$l(a_1, \dots, a_M) = \sum_{i=1}^T Y_i \ln [P_i(\mathbf{a})] + (1 - Y_i) \ln [1 - P_i(\mathbf{a})] \quad (4.2)$$

Now that we have a means to compute the likelihood we can fit the model using the standard techniques (gradient descent, Markov chain Monte Carlo, etc.). If the model $\hat{\lambda}_{\mathbf{a}}(x)$ is convex in its parameters $a_1 \dots a_M$ simple gradient descent is guaranteed to converge to the global optimum, and also has the advantage of being very fast to compute. Two important model classes for which this property holds are Poisson regression

$$\ln \hat{\lambda}_{\mathbf{a}}(x) = \sum_{i=1}^M a_i f_i(x) \quad (4.3)$$

and logistic regression:

$$\text{logit}(P(x)) = \ln \frac{\hat{\lambda}_{\mathbf{a}}(x)\delta}{1 - \hat{\lambda}_{\mathbf{a}}(x)\delta} = \sum_{i=1}^M a_i f_i(x). \quad (4.4)$$

Choosing a larger number of basis functions for the expansion becomes analogous to using narrower smoothing kernels in the binning approach, but has the advantage of providing a natural way to use the techniques in the model estimation literature (AIC [112], BIC [164], etc.) to choose the appropriate model order in a systematic manner. Finally, goodness of fit testing can be performed through the time rescaling theorem [165,166]. Having computed the firing ratemap of the cell based on its spike train, we can now quantify its spatial information content.

4.3.2 Place fields

A *place field* is a region of space within which a spatially selective cell exhibits active firing. Since some cells can exhibit multiple place fields it is useful to analyze them separately. We define a place field as a region where the ratemap exceeded 5Hz for at least 5cm. The boundaries of a place field are defined as the points where the firing rate drops below 5% of the peak value within the place field for at least 5cm.

To ensure place fields thus defined exhibit activity over multiple trials we require that a place field be active over many trials. However, for fields with low firing rate it may be entirely normal to see a trial without spiking activity. To determine whether a field is abnormally quiet on a given trial we therefore use a probabilistic approach. For each trial t compute the ratemap within the place field boundaries over all trials except the current one $\lambda^{\{T-t\}}(x)$. The number of spikes on trial t is therefore expected to be drawn from the Poisson distribution with expected value

$$E[N_t] = \int \lambda^{\{T-t\}}(x) O_t(x) dx. \quad (4.5)$$

Where $O_t(x)$ is the occupancy on trial t . If the observed number of spikes is below the $\alpha = 0.05$ percentile of the Poisson distribution the field is considered to be inactive on that trial.

By treating the firing ratemap within a place field as a probability density function, we can compute moments. The first few of these have very natural interpretations: the center of mass of the place field, the half-width, and skewness:

$$\tilde{\lambda}(x) = \frac{\lambda(x)}{\int \lambda(x) dx} \quad (4.6)$$

$$x_{com} = \int x \tilde{\lambda}(x) dx \quad (4.7)$$

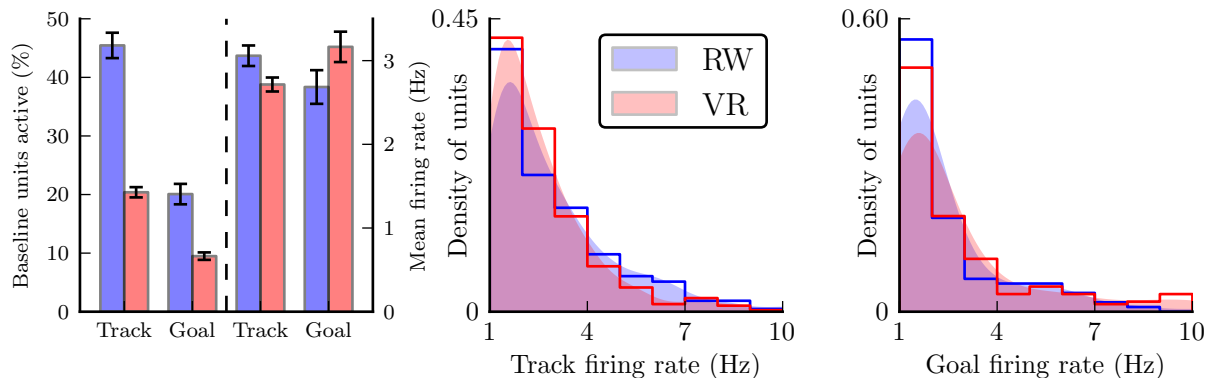
$$\sigma^2 = \left(\frac{\text{width}}{2} \right)^2 = \int (x - x_{com})^2 \tilde{\lambda}(x) dx \quad (4.8)$$

$$\text{skew} = \int \left(\frac{x - x_{com}}{\sigma} \right)^3 \tilde{\lambda}(x) dx \quad (4.9)$$

4.4 Properties of the rate code

4.4.1 Selective hippocampal activation in VR

The first fundamental question about hippocampal activity in VR is whether the overall level of cell activity is comparable to that in RW. To address this we compared the number of cells that are track active (defined as having rate above 1 Hz during running periods on the track) in VR and RW sessions to the number of cells isolated during the preceding baseline session. During baseline sessions rats were allowed to rest in a sleep box, and typically exhibited a wide variety of behaviors including grooming, sleeping and exploring. Baseline sessions thus provide an opportunity for a maximal subset of cells to be active, and comparing task to baseline cell counts provide an estimate of the fraction of hippocampal cells active during



(a) Fraction of cells active and (b) Track firing rate distribution for active cells. (c) Goal firing rate distribution for active cells.

Figure 4.4: While the fraction of pyramidal cells active in the VR (20.4 ± 0.9 %) was half that of RW (45.5 ± 2.1 %), the firing rates of active cells differed only slightly on the track ($p = 0.035$, rank-sum test) between VR (2.71 ± 0.08 Hz) and RW (3.06 ± 0.12 Hz). Firing rates of active cells at the goal location were also similar between VR (3.16 ± 0.18 Hz) and RW (3.06 ± 0.12 Hz). RW data are represented in blue, and VR data in red. Histograms are overlaid with a kernel density estimate using a Gaussian kernel and Silverman’s rule [167] for bandwidth estimation. A similar color and plotting convention is used throughout the remainder of the text.

the task sessions.

We recorded a total of 2119 pyramidal cells in baseline sessions preceding the VR task, and 528 pyramidal cells in baseline sessions preceding the RW task (as mentioned above, the VR task was run with greater frequency). Interestingly, while 45.5% of the RW baseline cells were track active, only 20.4% of the baseline cells were active in VR (figure 4.4a). Despite this two fold reduction in the number of active cells, the track firing rates of active cells in the VR (2.71 ± 0.08 Hz) were only slightly smaller than those in RW (3.06 ± 0.12 Hz), an effect that may be explained by the reduced running speed in VR [35]. Firing rates at the goal location were also comparable (figure 4.4c), but once again the fraction of active cells was halved in VR (figure 4.4a). This suggests that a subset of cells were selectively deactivated

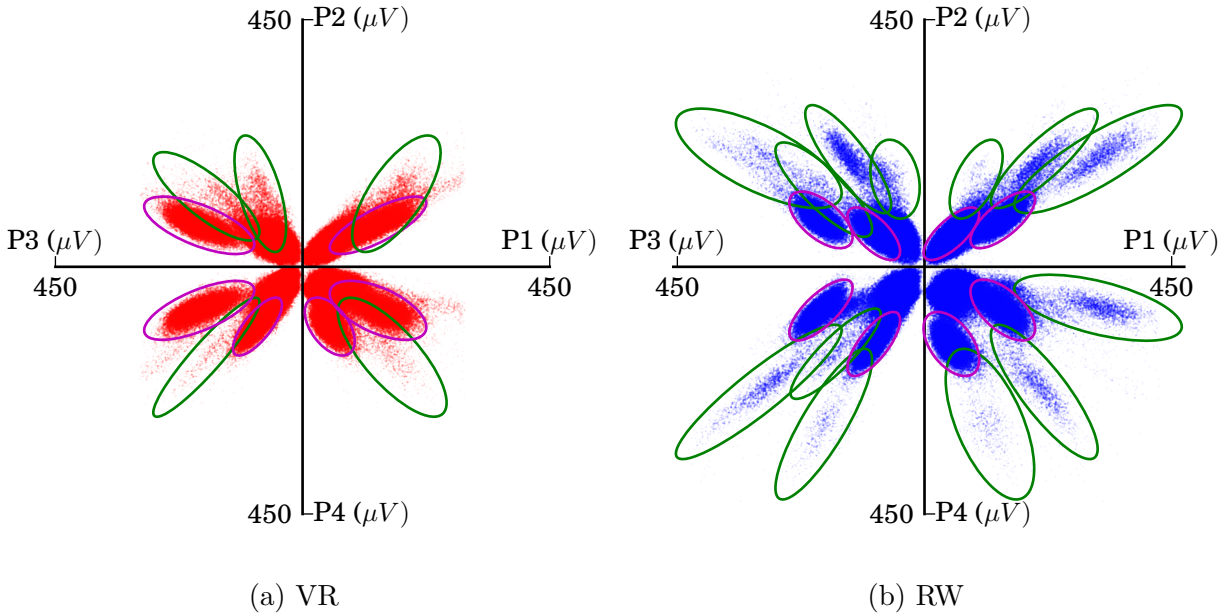


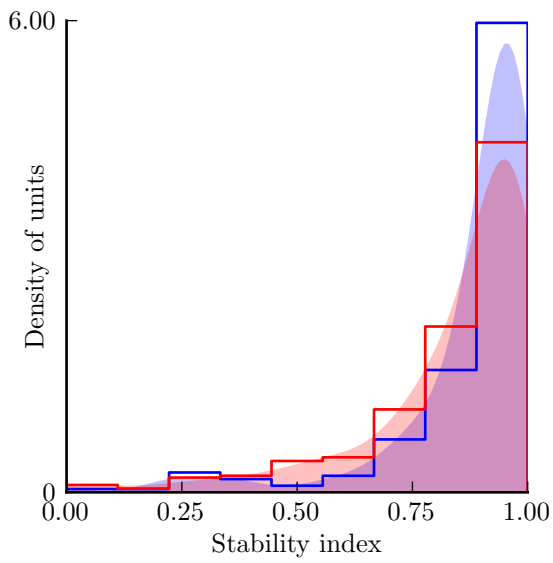
Figure 4.5: Peak projections of spike data recorded from the same tetrode on the same day in both VR and RW conditions clearly demonstrate the reduction in active cell count. Pyramidal neurons circled in green, interneurons in purple.

in the VR, rather than overall reduction in firing rates. The effect is evident in comparing spike sorting data projections for VR and RW data recorded from the same tetrode on the same day (figures 4.5a and 4.5b).

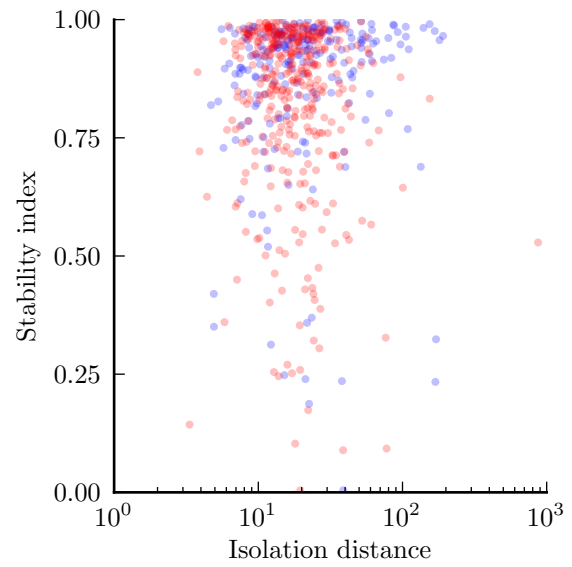
4.4.2 Stability

One important consideration is the possibility of unstable spiking activity occurring outside a clearly defined place field. To quantify this we introduce the *stability index*, defined for each cell as the correlation between the ratemap computed over even numbered trials and the ratemap computed over odd numbered trials. By comparing even and odd numbered trials (rather than the first and second half of trials) we avoid mislabeling systematic variation as instability.

The stability index for track active cells was slightly lower in VR than in RW (figure 4.6a), but this was not due to unit isolation concerns (figure 4.6b). Cluster isolation distance, false



(a) Stability index in VR and RW



(b) Stability index vs isolation distance

Figure 4.6: The stability index of cells in VR (0.80 ± 0.01) is slightly lower than for cells in RW (0.87 ± 0.01), ($p = 1.01 \times 10^{-5}$, rank-sum test). However, this is not due to cluster isolation differences in the two conditions.

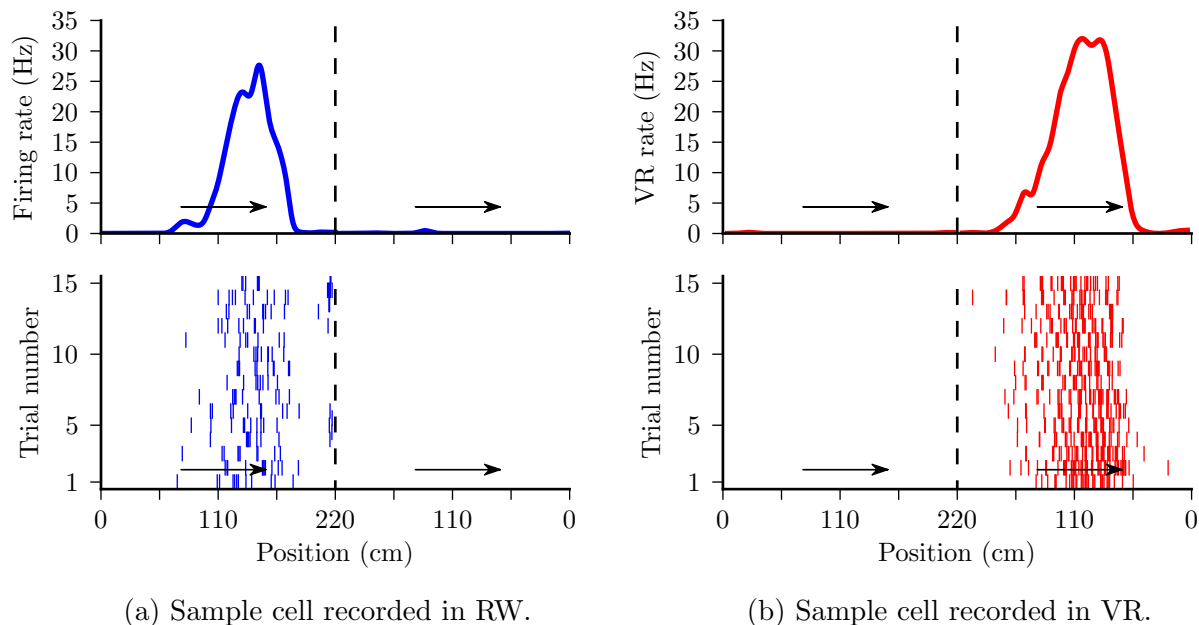


Figure 4.7: Sample cells exhibiting clear spatially selective firing. Top panel depicts the ratemap $\lambda(x)$, while the bottom is a raster plot indicating individual spike positions on each trial.

positive estimate, and false negative estimates (section 2.4.1) alone could not explain the variance observed in stability, but recording in VR has a significant effect, as assessed by a four way ANOVA ($p_{iso} = 0.06$, $p_{fp} < 0.05$, $p_{fn} = 0.6$, $p_{vr} < 0.001$). All further analysis was thus restricted to cells that were classified as stable, defined as having stability index greater than one half.

4.4.3 Spatial selectivity and information content

Clearly spatially selective firing was observed in cells both in RW and VR (figures 4.7a and 4.7b). However, not all cells in either RW or VR exhibit such clearly selective firing. It is thus helpful to quantify the degree of spatial selectivity exhibited by the spiking activity of a cell.

To quantify the spatial information in a ratemap we begin with the information theory

definition of entropy. For a random variable X with discrete probability density $p(x)$ the entropy is defined as:

$$H(X) = - \sum_i p(x_i) \log_2 p(x_i) \quad (4.10)$$

Thus defined the entropy measures the expected surprisal of the distribution. It can be thought of as a measure of how much is *not* known about the outcome of a draw from the distribution. The distribution with lowest entropy is the Dirac delta, while the uniform distribution has maximal entropy.

To apply this definition we need a probability distribution, so define

$$\xi(x_i) = \frac{p_i \lambda(x_i)}{\bar{\lambda}} \quad \text{where } \bar{\lambda} = \sum_i p_i \lambda(x_i) \quad \text{and } p_i = \frac{O(x_i)}{\sum_j O(x_j)}. \quad (4.11)$$

Since our interest is in defining a measure of spatial information which is greater for a cell with a more spatially selective ratemap, we define the information content of a ratemap to be the entropy of the uniform ratemap minus the entropy of ξ .

$$I = H(p) - H(\xi) = \sum_i p_i \left(\frac{\lambda(x_i)}{\bar{\lambda}} \right) \log_2 \left(\frac{\lambda(x_i)}{\bar{\lambda}} \right) \quad (4.12)$$

In addition to computing the information content for a given cell, we are also interested in finding whether a cells exhibits spatial modulation, which we define here to mean a spatial information content greater than what would be expected by chance in the absence of any relationship between the rat's position and spike timing. We can estimate a null distribution for the information content of a cell by repeatedly shuffling the spike train vector for each trial with respect to the position vector, and then computing the information content for the shuffled ratemaps.

Finally, as an alternative to spatial information we introduce the sparsity [168] of a ratemap (roughly corresponding to what fraction of the track the cell is active over), which is defined as:

$$S = 1 - \frac{(\int \lambda(x) dx)^2}{\int [\lambda(x)]^2 dx} \quad (4.13)$$

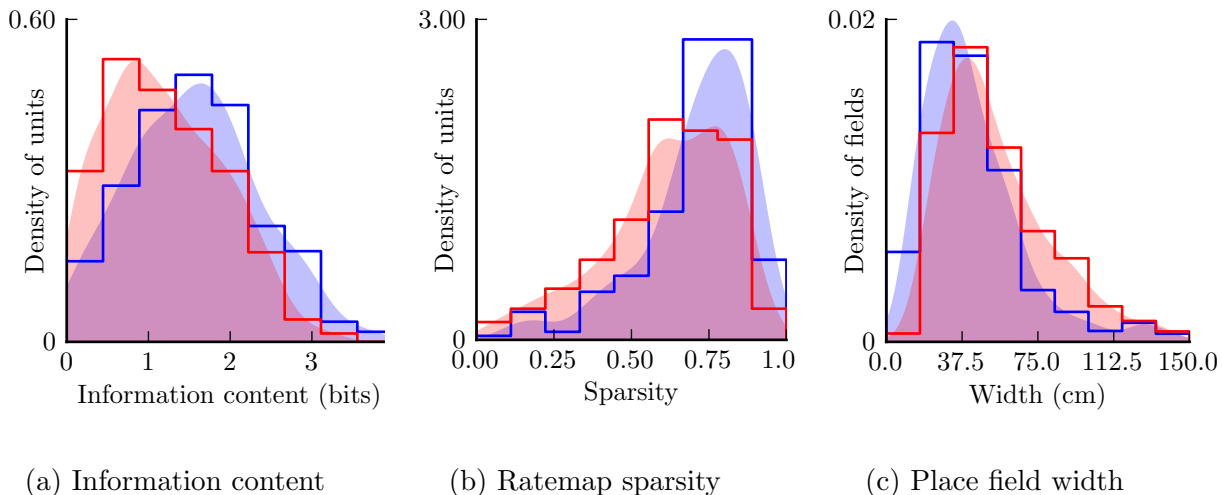


Figure 4.8: Spatial information content of pyramidal cells in VR (1.23 ± 0.03 bits) is significantly reduced ($p = 6.48 \times 10^{-8}$, rank-sum test) compared to those in RW (1.58 ± 0.05 bits). Similarly, ratemap sparsity in VR (0.65 ± 0.01) is significantly reduced ($p = 1.21 \times 10^{-9}$, rank-sum test) compared to RW (0.73 ± 0.01). Consistent with this, place field width in VR (55.8 ± 1.2 cm) is significantly greater ($p = 6.94 \times 10^{-12}$, rank-sum test) than in RW (44.3 ± 1.4 cm).

So the sparsity of a uniform ratemap is zero, and a delta function ratemap has sparsity unity.

Both the spatial information content (figure 4.8a) and the ratemap sparsity (figure 4.8b) are lower in VR than in RW. However, cells in both VR and RW overwhelmingly exhibit spatial modulation, with 96% of pyramidal cells in VR and 99% of cells in RW having spatial information content significantly above chance level. A reasonable explanation for these two results, which is borne out by the data, is that cells in VR still exhibit spatially selective firing, but that their place fields are wider than place fields in RW (figure 4.8c).

4.4.4 Directional firing

An interesting property of place cell firing on real world linear tracks is their directionality. A majority of place cells are active in only one direction [35], an effect which is absent in

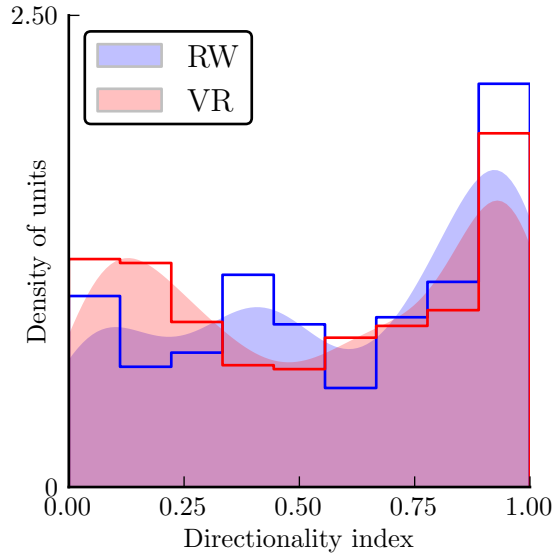


Figure 4.9: There is no significant difference ($p = 0.212$) between the observed distribution of directionality index values in VR (0.56 ± 0.02) and RW (0.59 ± 0.02).

two dimensional environments unless a spatial sequence is introduced [26]. We quantify this effect by defining the *directionality index*:

$$D = \left| \frac{\int (\lambda_F(x) - \lambda_R(x)) dx}{\int (\lambda_F(x) + \lambda_R(x)) dx} \right| \quad (4.14)$$

Where λ_F and λ_R are the firing ratemaps for the forward and backward running directions respectively. Cells which fire in only one running direction thus have a directionality index of unity, while cells which fire equally in both directions have a directionality index of zero. Cells with $D \geq 0.5$ are considered to be directional, while cells with $D < 0.5$ are considered bidirectional.

Despite the absence of vestibular cues associated with turning around in the VR, the observed distributions of directionality index values are not significantly different in VR and RW (figure 4.9). This implies that vestibular cues are *not* necessary for directional place cell firing, but that distal visual cues are sufficient to generate directional activity.

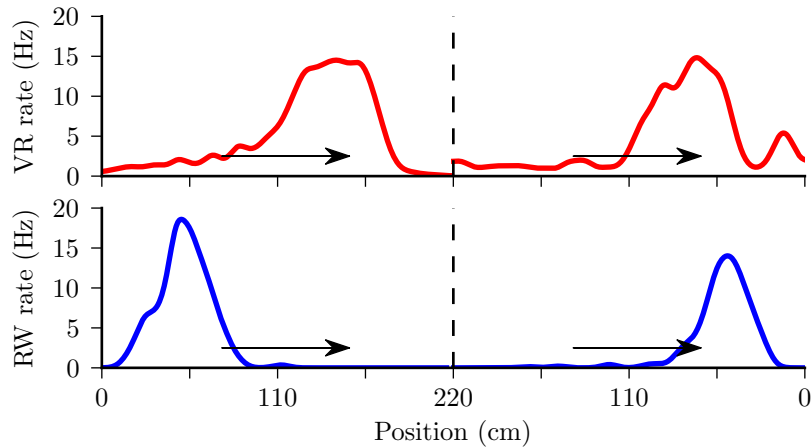


Figure 4.10: Ratemaps from two sample cells that exhibit bidirectional activity. The cell active in the VR (red) fires at the same distance from the start of the track, while the RW cell (blue) fires at the same absolute spatial position.

4.4.5 Bidirectional activity: the disto code

However, while the fraction of cells that were bidirectional is comparable in VR and RW, the ratemaps of these cells exhibited very different characteristics. It is known that bidirectional cells in RW fire at roughly the same spatial position in both running directions [73, 75, 168], though there is a slight backward shift in each direction around the common midpoint, creating a prospective coding scheme. This firing pattern is also apparent in our data (figure 4.10).

In sharp contrast to the position coding of bidirectional cells in the RW, bidirectional cells in VR tended to fire at the same distance from the start of the track in both running directions, creating a *disto-code* (figure 4.10).

To quantify this effect, we introduce the disto-code index and position-code index. We begin by finding, for bidirectional cells, the boundaries of the largest place field. In the opposite running direction these boundaries are used to define a position-coding zone (Z_P), and a disto-coding zone (Z_D) by flipping the boundaries as appropriate. The disto-code

index is then defined as:

$$I_D = \frac{\int_{x \in Z_D} \lambda(x) dx - \int_{x \notin Z_D} \lambda(x) dx}{\int_{x \in Z_D} \lambda(x) dx + \int_{x \notin Z_D} \lambda(x) dx}, \quad (4.15)$$

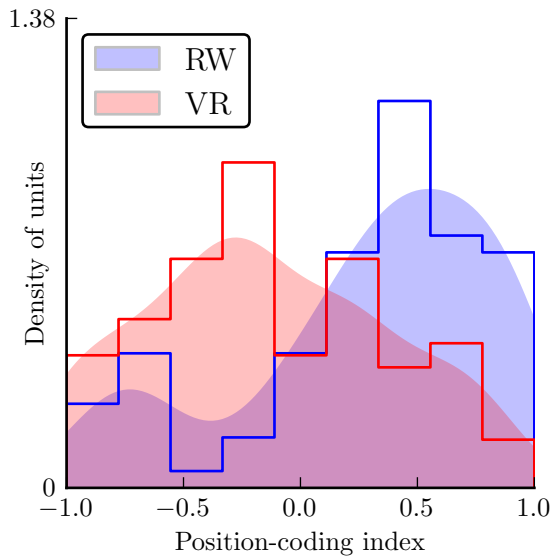
and similarly the position-code index is defined as:

$$I_P = \frac{\int_{x \in Z_P} \lambda(x) dx - \int_{x \notin Z_P} \lambda(x) dx}{\int_{x \in Z_P} \lambda(x) dx + \int_{x \notin Z_P} \lambda(x) dx} \quad (4.16)$$

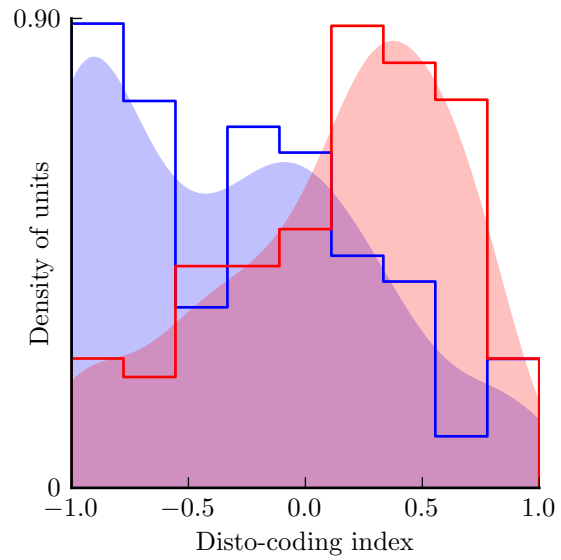
Defined in this way, the index values are in the range $[-1, 1]$, with positive values for indicating the presence of a disto- or position-coding scheme, and negative values indicating an absence of these effects. It should be noted that the two are not mutually exclusive, a cell which fires in the middle of the track, for example, would have positive values for both I_D and I_P . Nevertheless, cells in RW exhibited significantly positive position-code index (figure 4.11a), but negative disto-code index (figure 4.11b). Cells in VR displayed the opposite effect, with negative position-code index (figure 4.11a), but positive disto-code index (figure 4.11b).

It is possible that the disto-coding cells are in fact responding in time [116], rather than distance. Since these two variables are so closely linked in the current experiment, it is not possible to conclusively disambiguate them. It can however be partially addressed by comparing ratemaps calculated in both distance and time during the fastest and slowest trial blocks. By calculating the correlation between the fast and slow ratemaps, we find that a distance representation is more stable than a time representation, not just at the population level (figure 4.12a), but also for individual cells (figure 4.12b).

If the majority of individual cells in VR exhibit a disto-coding scheme, it stands to reason that the population level coding scheme should also be distance based. While single cell properties are interesting, the collective activity of multiple units is an equally important area to investigate. To estimate the similarity of the population rate code between one position and another we define the population vector overlap by computing a normalized dot product along the unit dimension (where N is the number of single units in the population):

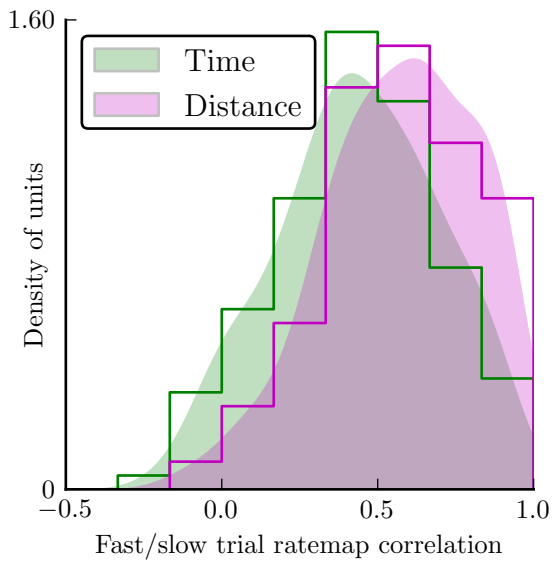


(a) Position-coding index

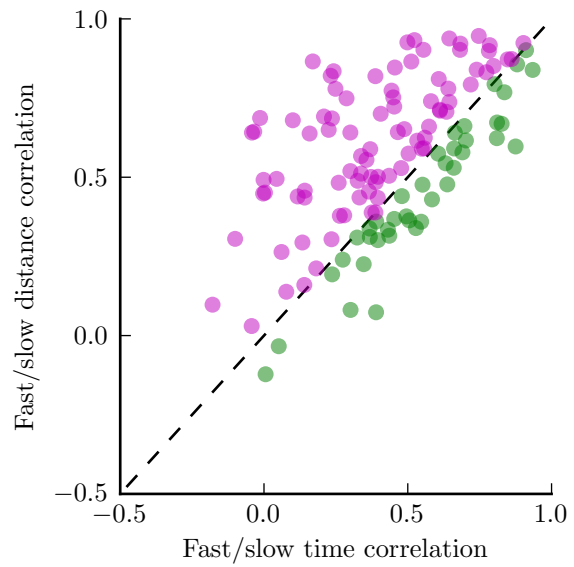


(b) Disto-coding index

Figure 4.11: Position-code index values were positive in RW (0.27 ± 0.05 , $p = 8.2 \times 10^{-7}$, sign-rank test), but negative in VR (-0.11 ± 0.04 , $p = 1.8 \times 10^{-2}$, sign-rank test), indicating the presence of a bidirectional position code in RW, but it's absence in VR. In contrast, disto-code index values were negative in RW (-0.25 ± 0.06 , $p = 5.1 \times 10^{-5}$, sign-rank test) but positive in VR (0.14 ± 0.04 , $p = 9.5 \times 10^{-4}$, sign-rank test), indicating the presence of a disto code.



(a) Population distribution



(b) Individual cells

Figure 4.12: The fast/slow trial correlations are significantly ($p = 4.8 \times 10^{-5}$, rank-sum test) greater in the distance representation (0.57 ± 0.02) than in the time representation (0.44 ± 0.02). The majority of individual cells also displayed greater correlation in the distance representation than in time.

$$PVO(x, y) = \frac{\sum_{j=1}^N \lambda_j(x) \lambda_j(y)}{\sqrt{\sum_{j=1}^N \lambda_j^2(x)} \sqrt{\sum_{j=1}^N \lambda_j^2(y)}} \quad (4.17)$$

Since the overlap values are not normal in their distribution, we estimate significance using a shuffling bootstrap approach. By repeatedly shuffling the unit identities and computing the overlap we obtain a distribution of overlap values under the null hypothesis that a cell’s ratemap at the two positions (x, y) is no more correlated than the ratemaps of two unrelated cells. The advantage of this shuffling approach is that it maintains effects which are not specific to the single cells (such as position dependence of place field width).

The population vector of bidirectional cells in RW reveals a clear -45° diagonal (figure 4.13a), indicating that cells spiked around the same position on the track in both movement directions. The opposite is true in VR, where the population vector reveals a clear $+45^\circ$ diagonal (figure 4.13b), indicating that cells spiked at the same distance along the track in both directions. In both cases these diagonals significantly exceed levels expected by chance in the absence of either position or distance coding effects (figures 4.13c and 4.13d). A disto-code like response has been reported on a single unit level in RW [115, 169], but not on the population level.

The visual cues presented by the virtual environment are different in two running directions (i.e. the scene has minimal symmetries). This therefore suggests that the disto-coding cells, which fire the same way in both directions, are not responding based upon visual stimuli. We hypothesize that they are in fact representative of a path integrator neural circuit based upon self motion cues such as optic flow and ambulatory input.

One possibility to consider is that the disto-code may arise due to the presence of a salient visual stimulus (the vertical pillar) that signifies reward in both running directions. To check that this single symmetry in the virtual environment was not responsible for the disto-code observed we ran two rats in a control experiment in which the pillar was removed at either one or both ends of the track. The rats’ behavior was not altered by this manipulation, and the bidirectional cell still exhibited a clear disto-coding scheme figure 4.14.

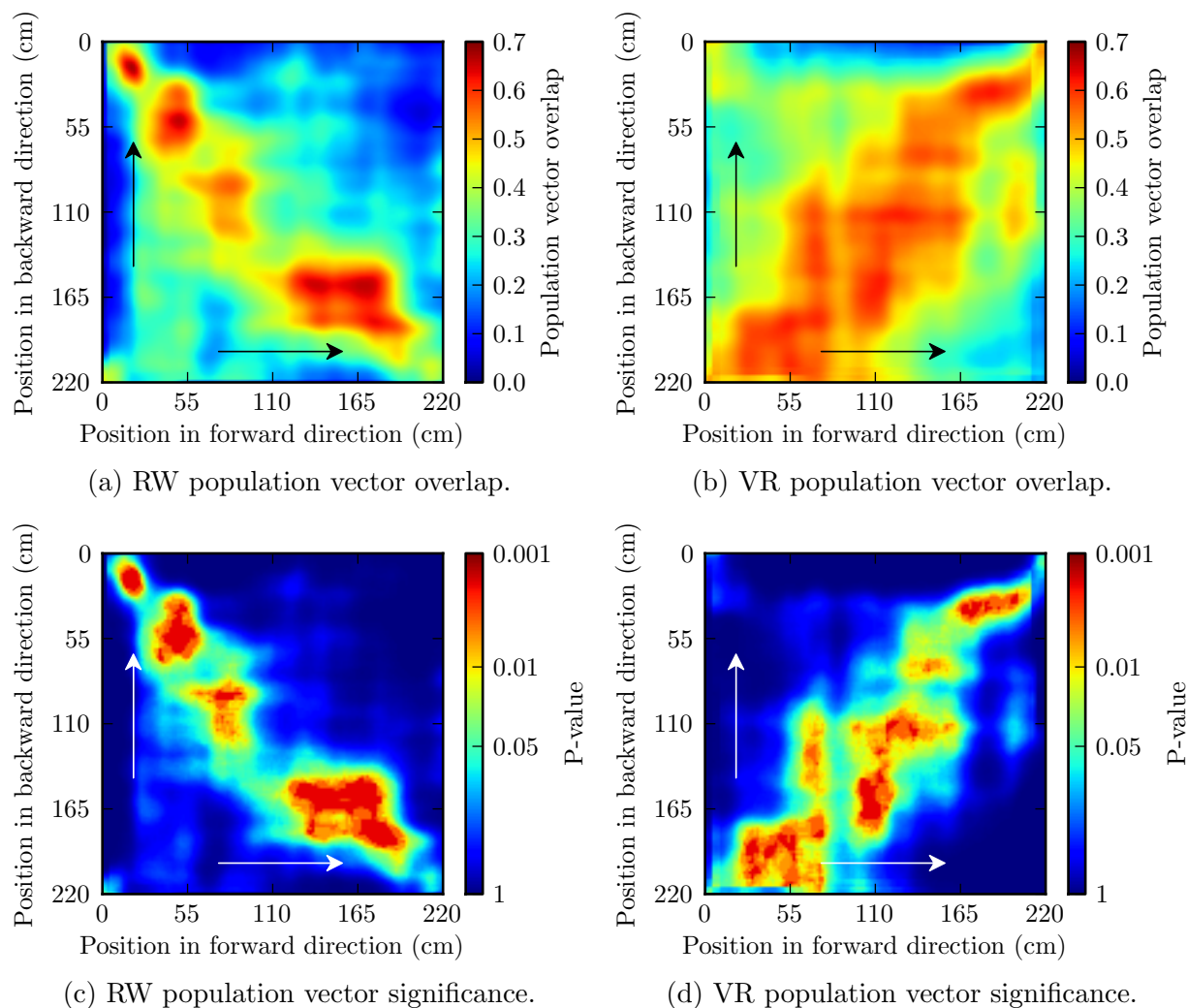
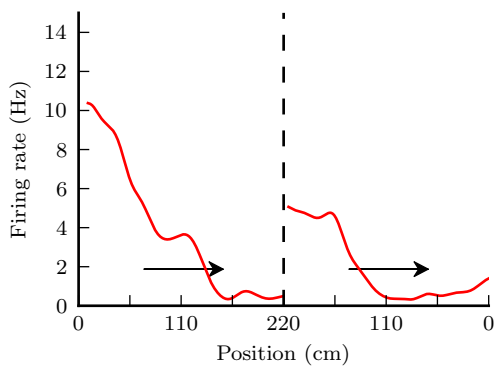
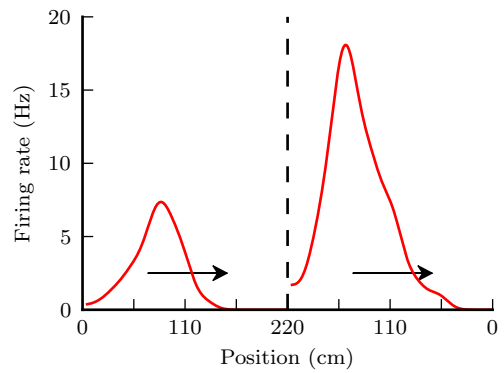


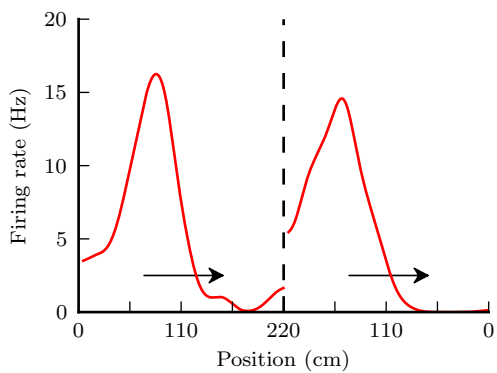
Figure 4.13: Population vector analysis of bidirectional cells in RW and VR reveals opposite coding schemes. In RW the population rate code overlap is significantly above chance level along a -45° diagonal, reflecting the presence of a position code. In VR, the population vector overlap is significantly above chance level along a $+45^\circ$ diagonal, reflecting the presence of a distance based coding scheme. Note also how the wider place fields in VR manifest as a wider band in the population vector.



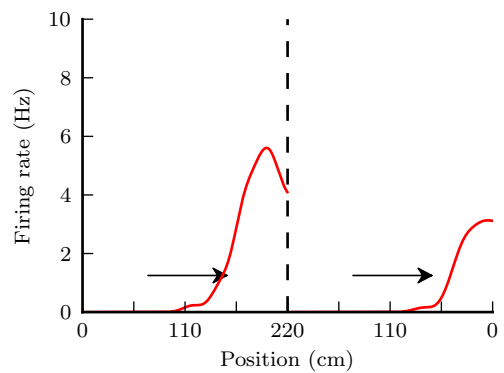
(a) Single pillar condition sample 1.



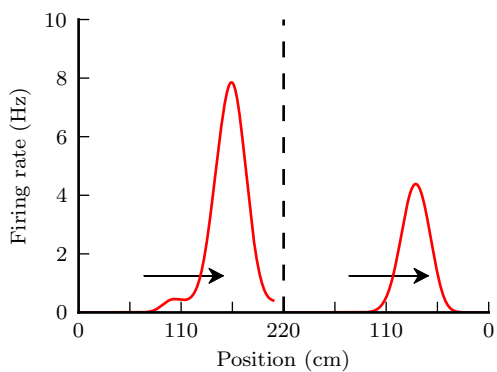
(b) Zero pillar condition sample 1.



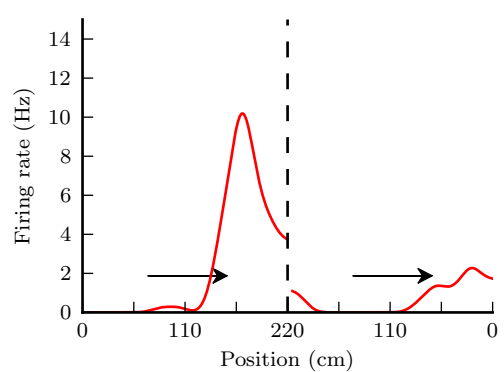
(c) Single pillar condition sample 2.



(d) Zero pillar condition sample 2.



(e) Single pillar condition sample 3.



(f) Zero pillar condition sample 3.

Figure 4.14: Ratemaps from six sample cells recorded in the pillar control experiment still exhibit clear disto-coding.

4.5 Properties of the temporal code

4.5.1 Reduction in theta frequency does not alter phase precession

The local field potential (see section 1.1) in CA1 is known to exhibit strong oscillations in the theta band (4-12 Hz) during running behavior, which modulates both pyramidal and interneuron firing rates.

Multi-taper power spectral analysis of LFP recordings in VR and RW during running behavior reveal the clear presence of theta oscillations in both recording conditions. However, the frequency of theta rhythm in VR is reduced compared to RW, an effect most clearly visible when comparing the autocorrelation of LFP recordings from the same electrode in both conditions (figure 4.15).

To ensure calculations involving phase precession and theta rhythm were not adversely affected by noisy LFP data, only LFPs exhibiting clear theta rhythm were used for further analysis. The criteria for inclusion was that an LFP needed to have power in the theta band (4-12Hz) exceeding at least one third of the power in the delta band (0.01-4Hz) during running periods.

Despite the reduced frequency of the theta rhythm, place fields in both VR (figure 4.16a) and RW (figure 4.16b) displayed clear phase precession [25, 57, 60, 66, 67], with spikes farther into the place field preferentially occurring at lower phases of the hippocampal theta rhythm.

To quantify the strength of phase precession in a place field, we define a circular linear correlation coefficient [170] between the position of individual spikes and their theta phase, as follows:

$$\rho(x, \phi) = \sqrt{\frac{r_{cx}^2 + r_{sx}^2 - 2r_{cx}r_{sx}r_{cs}}{1 - r_{cs}^2}}, \quad (4.18)$$

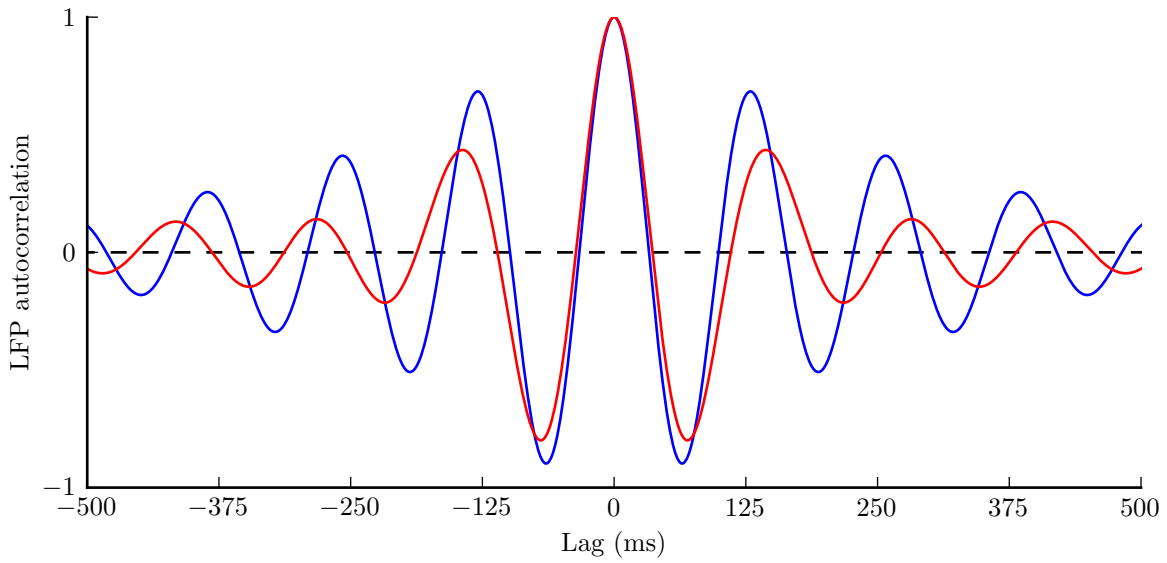


Figure 4.15: Autocorrelation of hippocampal LFP data exhibits clear peaks at multiples of the theta period in both VR and RW.

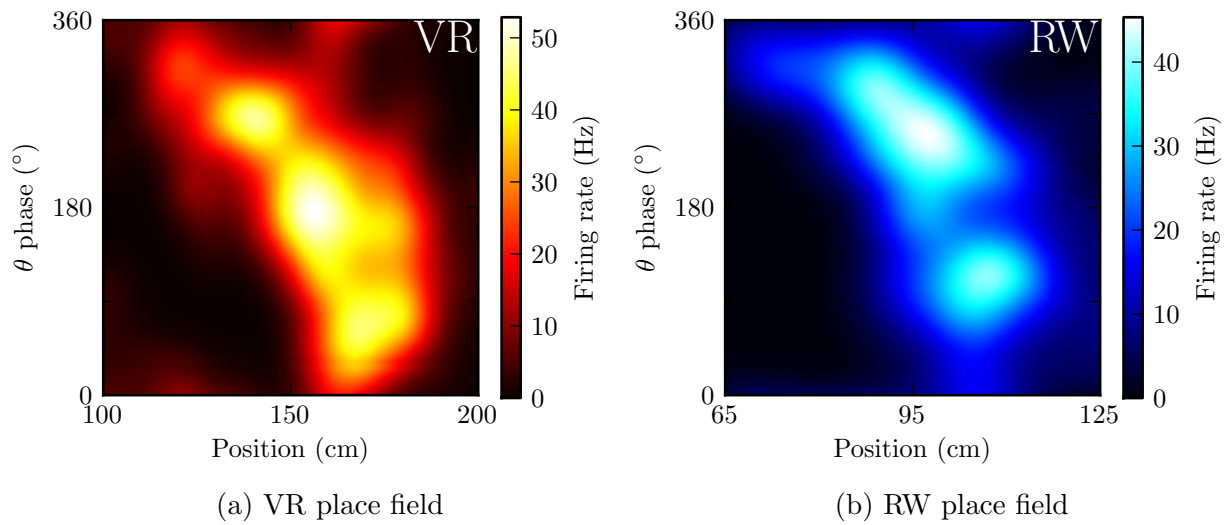


Figure 4.16: Spatio-temporal firing rates, computed in a manner analogous to the linear ratemaps for sample place fields in VR and RW. Phase precession is clearly visible in both cases.

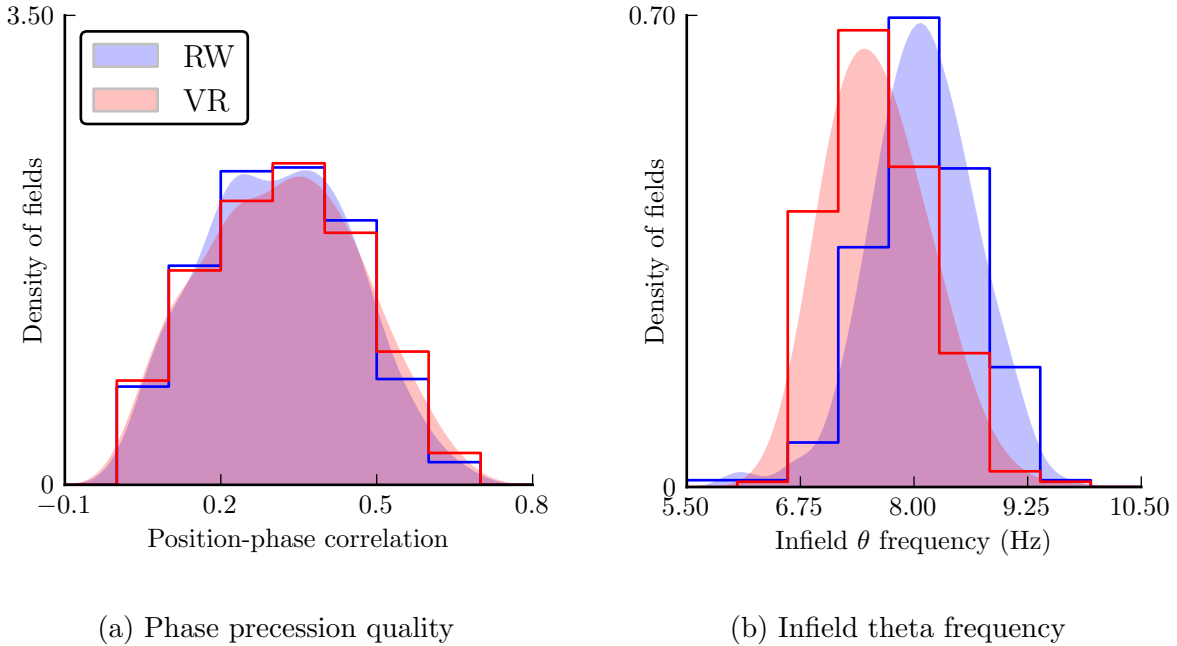


Figure 4.17: Quality of phase precession, assessed by a circular linear correlation measure, showed no difference between VR (0.33 ± 0.01) and RW (0.33 ± 0.01) place fields, while the frequency of theta rhythm within the place fields was significantly ($p = 1.83 \times 10^{-49}$, rank-sum test) reduced in VR (7.53 ± 0.02 Hz) compared to RW (8.25 ± 0.03 Hz).

where

$$r_{cx} = \text{corr}(x, \cos \phi) \quad (4.19)$$

$$r_{sx} = \text{corr}(x, \sin \phi) \quad (4.20)$$

$$r_{cs} = \text{corr}(\cos \phi, \sin \phi). \quad (4.21)$$

The quality of phase precession in VR was identical to that in RW (figure 4.17a), despite a 9% reduction in the theta rhythm frequency within each place field (figure 4.17b).

4.5.2 Reduction in spiking frequency

Both pyramidal and interneurons are known to be modulated by the hippocampal theta rhythm [25, 52, 57, 60, 66, 67]. While pyramidal neurons phase precess, and thus necessarily

must spike at a frequency faster than the theta rhythm, interneurons are typically phase locked to theta, firing preferentially at a particular phase of theta. The reduction in LFP theta frequency should thus manifest itself in a reduction of the spiking frequency of both pyramidal and interneurons.

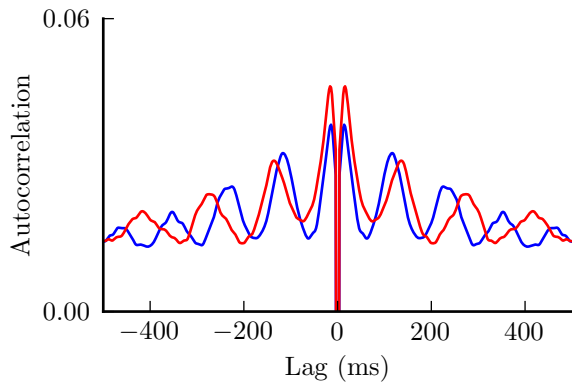
By computing the autocorrelation of single unit spike trains (figures 4.18a and 4.18b) and finding the temporal lag of the first peak, we can estimate the spiking frequency of cells. Such analysis confirms the significant reduction in theta rhythm frequency (figures 4.18c and 4.18d).

One potential reason for such a difference in the frequency of theta rhythm could be the reduced speed of the rats in VR compared to RW. In fact, the well known speed dependence of theta frequency is a fundamental requirement of a popular class of models of phase precession. In order to investigate this effect we must introduce a method of estimating the frequency of theta rhythm in a time dependent way, something which a standard autocorrelation does not allow.

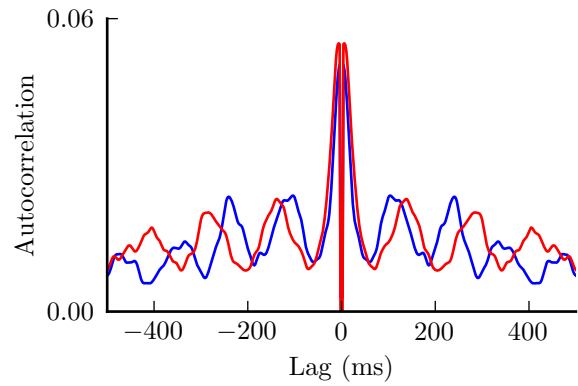
4.5.3 Time dependent frequency estimation

There are in fact several approaches to estimating the frequency of the theta rhythm in a time dependent way. The simplest of these involves estimation of the phase of the oscillation using the Hilbert transform. Once the phase is determined, jumps of 2π in the oscillation phase can be used to define the beginning and end of an individual theta cycle. The inverse period of these theta cycles provide an estimate of the average theta frequency over the course of the cycle. While simple, this method is limited in the temporal resolution it can provide.

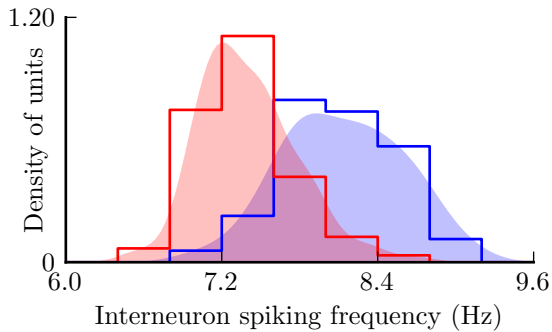
An alternative is to numerically differentiate the phase estimates produced by the Hilbert transform to produce an estimate of the instantaneous frequency of the oscillation. This overcomes the temporal resolution problem, but has been shown to provide biased estimates [171]. The short time Fourier transform (STFT) provides a third approach, but is plagued by the



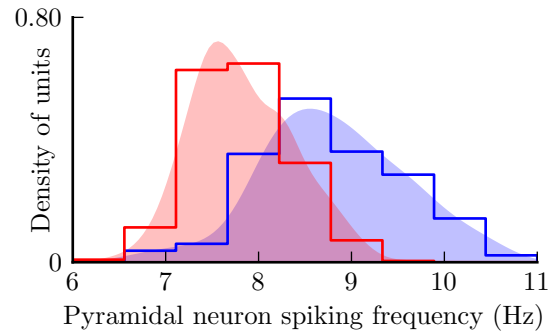
(a) Autocorrelation of spike train recorded from the same interneuron in both VR and Rw.



(b) Autocorrelation of spike train recorded from the same pyramidal neuron in both VR and Rw.



(c) Interneuron spiking frequency



(d) Pyramidal neuron spiking frequency

Figure 4.18: Spiking frequency of interneurons in VR (7.40 ± 0.03 Hz) was significantly lower ($p = 5.2 \times 10^{-16}$, rank-sum test) than in RW (8.13 ± 0.07 Hz). Pyramidal neurons similarly exhibited significantly ($p = 7.6 \times 10^{-51}$, rank-sum test) decreased spiking frequency in VR (7.83 ± 0.03 Hz) compared to RW (8.81 ± 0.05 Hz).

inverse relationship between temporal accuracy and frequency accuracy. The most accurate method for LFP data is based on the Kalman filter [171], and is the one employed in this analysis, unless otherwise stated.

4.5.4 Speed dependence of LFP theta rhythm

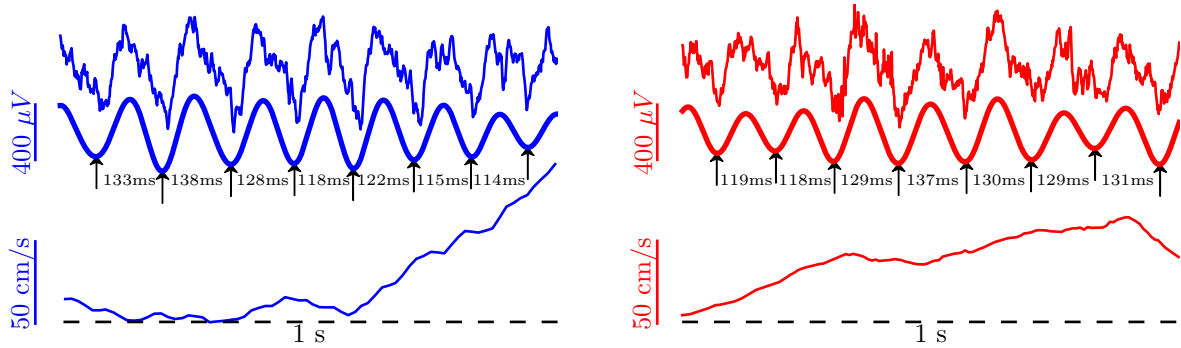
In RW the frequency of the hippocampal theta rhythm is known to increase with running speed. While this is reflected in our RW data, data recorded in VR do not exhibit any clear relationship between speed or theta frequency (figure 4.19c). In fact, the distribution of correlation coefficients between speed and theta frequency in VR is centered around zero (figure 4.19d), whereas in RW a large majority (85.4%) of recordings exhibit significant correlation between running speed and theta frequency. These results are consistent with previous studies which reported modification of the theta rhythm by lesions of the vestibular nucleus [172].

The fact that phase precession is identical in VR and RW despite the large changes in the theta rhythm places restrictions on theories of phase precession that depend on the precise value of theta frequency or its speed dependence [25, 173–175]. Instead they favor alternative mechanisms that are insensitive to these phenomena [29, 60, 66], that apply equally to networks with diverse connectivity patterns such as the entorhinal cortex and CA1, and hence do not require recurrent excitatory connections [29, 66].

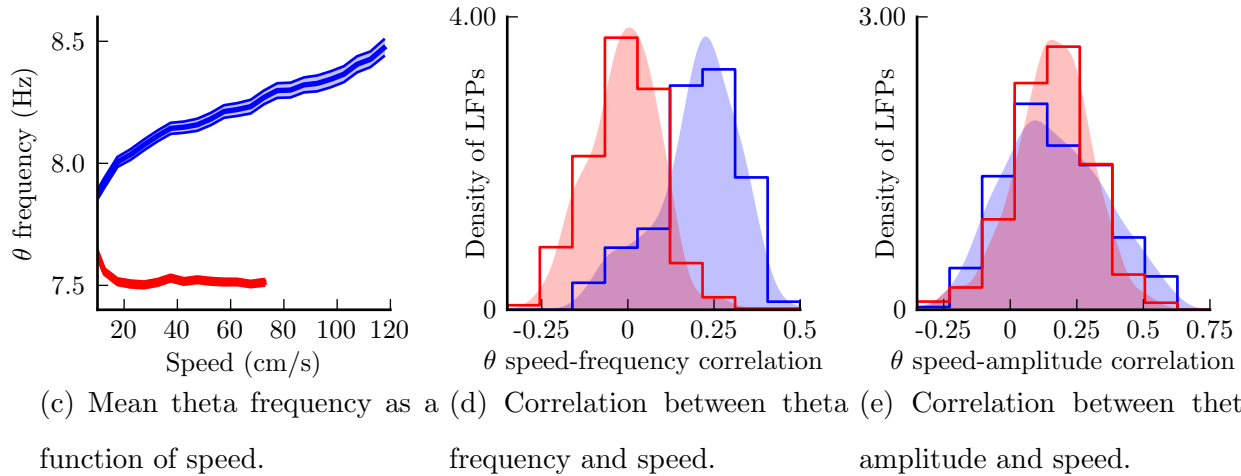
Interestingly, the amplitude of theta oscillations increases similarly with speed in VR and RW (figure 4.19e). Suggesting that unlike frequency, theta amplitude is unaffected by vestibular cues.

4.5.5 Speed dependent interneuron spike frequency

Since the LFP theta rhythm strongly modulates both pyramidal and interneuron spiking activity, the absence of speed dependent change in the LFP frequency should manifest itself in the spiking frequency of both cell types. However, since pyramidal neurons are selective

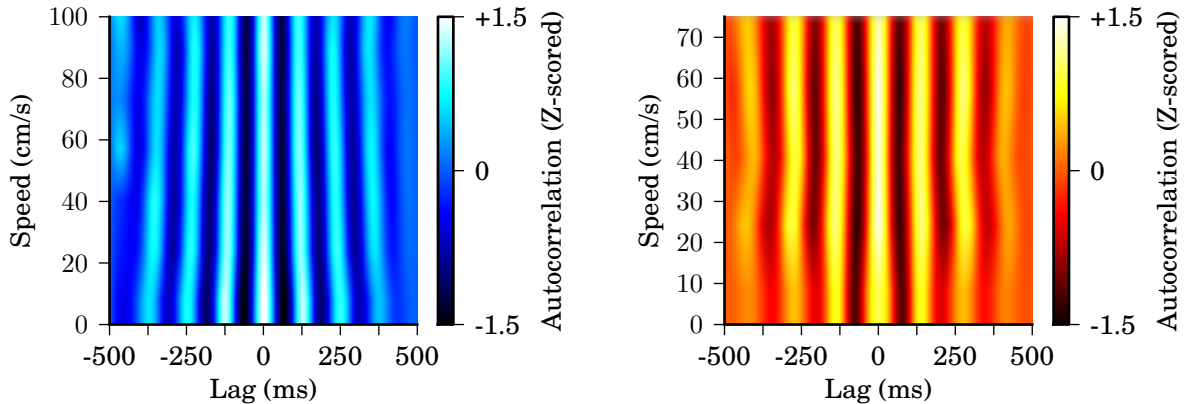


(a) Unfiltered LFP, theta-filtered LFP, and speed (b) Similar sample data as figure 4.19a from the same electrode in VR.



(c) Mean theta frequency as a function of speed. (d) Correlation between theta frequency and speed. (e) Correlation between theta amplitude and speed.

Figure 4.19: Speed dependent frequency increased is absent in VR. Correlation coefficients between theta frequency and speed in RW (0.21 ± 0.01) and VR (-0.01 ± 0.01) reveals the absence of speed dependence in theta frequency. In contrast, theta amplitude is similarly affected by speed in RW (0.16 ± 0.01) and VR (0.16 ± 0.01).



(a) Sample interneuron in RW.

(b) Sample interneuron in VR.

Figure 4.20: Sample speed dependent spike train autocorrelation from interneurons in RW and VR. The RW cell shows clear speed dependent increase in theta frequency (i.e. decrease in period), while the VR cell does not exhibit any reliable change with speed. For ease of visual comparison each speed bin has been z-scored.

active on only portions of the track, and typically have much lower mean rates than interneurons, estimation of speed dependent effects on spiking frequency for pyramidal neurons is a difficult task.

We therefore focus on interneurons, for which we can compute speed-dependent spike train autocorrelation. Computing the autocorrelation of a point process can be achieved by iterating over all possible pairs of events in the process, and computing the time difference between events. For n spikes, this produces a set of $n(n - 1)$ time deltas, which can then be binned with bin sizes appropriate to the problem under investigation.

This approach to computing an autocorrelation lends itself naturally to extension to speed-dependent autocorrelation. For each pair of spikes, compute not only the time difference δ_t , but also the mean speed between the two spike times. By binning these $n(n - 1)$ pairs of time and speed values, we can estimate a speed dependent autocorrelation which, for each speed bin, can then be filtered in the theta band to produce an estimate of the theta modulated spiking frequency at different speeds. Applying this procedure to interneuron

spike trains confirms the speed modulation of theta rhythm in RW (figure 4.20a), and the absence of speed modulation in VR (figure 4.20b).

4.6 The role of passive scene rotation

4.6.1 Different environments hypothesis

One important consideration is the potential effect of the passive scene rotation when the rat reaches the ends of the track in VR. By passively reversing the scene, the animal is potentially deprived of visual and self-motion cues which may be necessary to establish that it is viewing the same scene from a different angle, rather than simply an entirely different scene. Such an effect could potentially explain the absence of a bidirectional position code in virtual reality.

This argument, however, does not stand up to further scrutiny. It has been shown that the subpopulations of cells active in different environments are largely independent [29]. The hypothesis that the rat is treating the virtual scene as two independent worlds, rather than views of the same world, thus makes a prediction about the fraction of cells that should be bidirectional.

Suppose, for the time being, that the rat treats each of the two running directions as different environments. Given that the visual and other sensory cues are of similar saliency in both running directions, it is reasonable to assume that the probability of a cell being active (i.e. exceeding firing rate threshold T) in one “environment” is the same as the probability of it being active in the other.

Define $F_1(r)$ as the cumulative distribution function of firing rates in the first environment, and similar $F_2(r)$ for the second environment. We can similarly define $F_{1\cup 2}(r)$ for the cumulative distribution of firing rates in the combined environment (i.e. using spiking and occupancy data from both environments). From the assumption of equal probability of activation we have $p = 1 - F_1(T) = 1 - F_2(T)$. Let η indicate the fraction of time spent in the

first environment (typically very close to 0.5, but we do not need to assume any particular value here).

It follows that the mean rate observed in the joint environment will be roughly $r_{1\cup 2} = \eta r_1 + (1 - \eta)r_2$. It thus has a cumulative distribution function $F_{1\cup 2}(r) = \eta F_1(r) + (1 - \eta)F_2(r)$. The probability of being active in the joint environment is therefore

$$\begin{aligned} p_{1\cup 2} &= 1 - F_{1\cup 2}(T) = 1 - \eta F_1(T) - (1 - \eta)F_2(T) \\ &= 1 - \eta(1 - p) - (1 - \eta)(1 - p) \\ &= p \end{aligned} \tag{4.22}$$

So to estimate p we can use the fraction of cells active in the joint environment, which (as discussed in section 4.4.1) was roughly 0.2 in VR and 0.45 in RW.

Now suppose there are N cells in the baseline that may potentially be active in either of the two environments, based on these probabilities. We then expect $n_1 \sim \text{Binomial}(N, p)$ cells to be active in the first environment, and $n_2 \sim \text{Binomial}(N, p)$ in the second environment, and $n_{1\cup 2} \sim \text{Binomial}(N, p^2)$ to be active in the joint environment. The fraction of active cells that are directional (i.e. active in only one of the two environments) is then

$$d(N, p) = 1 - \frac{n_{1\cup 2}}{n_1 + n_2 - n_{1\cup 2}}. \tag{4.23}$$

Numerical simulation of the distributions of $d(N, p)$ using the values of N and p observed in the data are depicted in figure 4.21. As expected, in RW the observed fraction of directional cells falls well outside the 95% confidence limit. The VR data are even further outside the confidence intervals than the RW data is.

The observed fractions of cells that are directional are thus significantly lower than would be predicted by independent activation based on the hypothesis that place cells treat the two movement directions as distinct environments. Based on these results, it is reasonable to reject the distinct environment hypothesis.

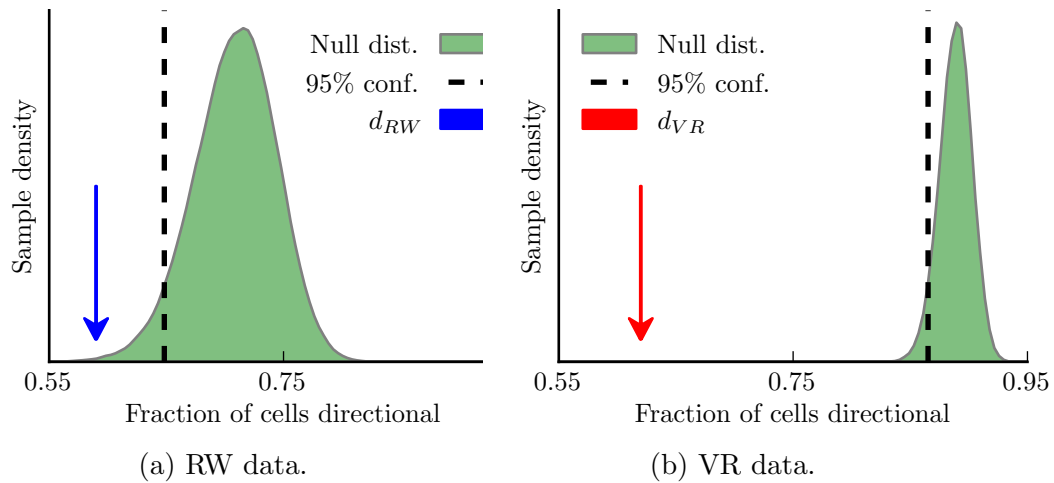


Figure 4.21: The observed fraction of cells that are directional lies well outside the null distribution calculated from the hypothesis that cells treat the two running directions as different environments.

4.6.2 Rotation triggered population vector analysis

How does the cell population respond to the instantaneous passive rotation of the visual scene at the track ends? To test this, we computed a rotation triggered population vector overlap. Briefly, for each cell we computed the firing rate with 10ms temporal resolution over a window starting five seconds before the rotation, and extending fifteen seconds after the rotation. We then compute the population vector $PVO(t_1, t_2)$ in a manner analogous to the spatial population vector overlap described in equation (4.17). The analysis is restricted to cells that are active (mean rate exceeding 1Hz) in the five seconds preceding the passive scene reversal, and the two ends of the track are treated separately.

The population vector reveals several interesting effects (figure 4.22). The first of these is the absence of any sudden change in the population rate immediately following the rotation. In fact, there is a high degree of overlap in the ratemap starting a few seconds before rotation, and continuing roughly five seconds after rotation. It is apparent from the median speed profile that this region of high overlap corresponds to the period during which the rats are

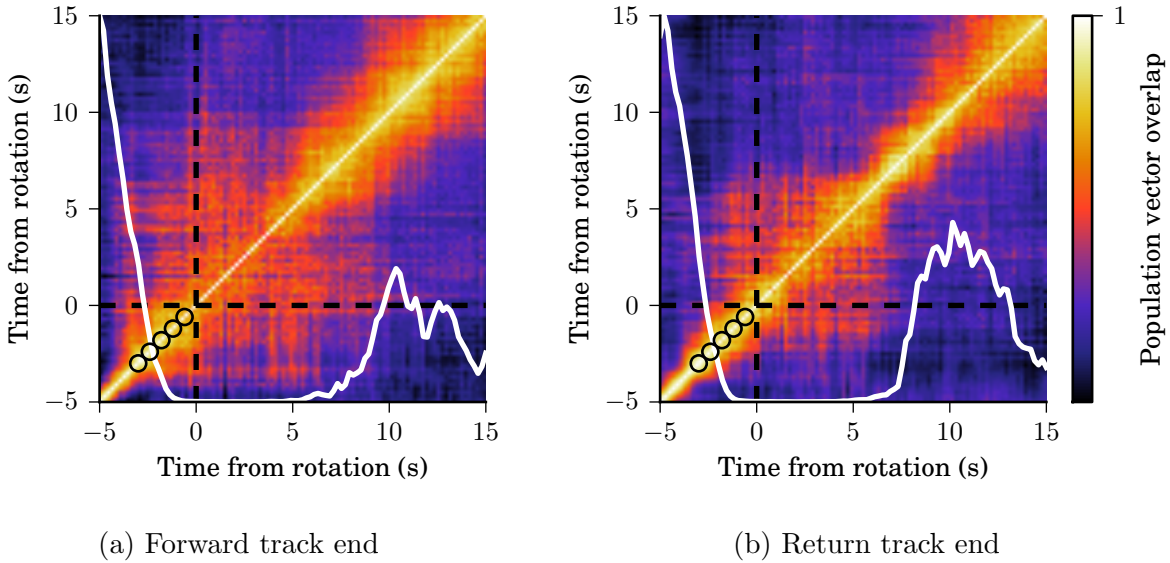


Figure 4.22: Rotation triggered population vectors for the two ends of the track. Black dashed line indicates the time of scene rotation, and circles indicate timing of reward pulses. Median speed profile overlaid in white.

stationary, and consuming reward.

At first glance these results appear at odds with a report by Jezek et al. [176] of representation switching within a theta cycle after a change in visual cues, and subsequent flickering between representations lasting a few seconds. There are, however, several significant differences. Notably, while flickering was reported primarily in CA3, it was less clear in CA1, an observation potentially attributable to the lack of recurrent excitatory connections in CA1. Further, the analysis in the Jezek study is restricted to periods of mobility, while in our case the switch in the visual stimuli happens during immobile periods of reward consumption, when the rats' attention is focused on the physical reward tube rather than the virtual environment. These findings further support the conclusion that the passive scene rotation is unlikely to be responsible for the appearance of the disto-code.

4.6.3 Active turn control experiment

To confirm that the passive scene reversal protocol did not somehow induce the disto-coding scheme, a control experiment was run in which two rats were trained to run a variation of the virtual linear track task where the rats were required to actively rotate the treadmill to rotate the virtual environment. Bidirectional cells recorded under this protocol still exhibited clear disto-coding, with the position-code index significantly lower than the disto-code index.

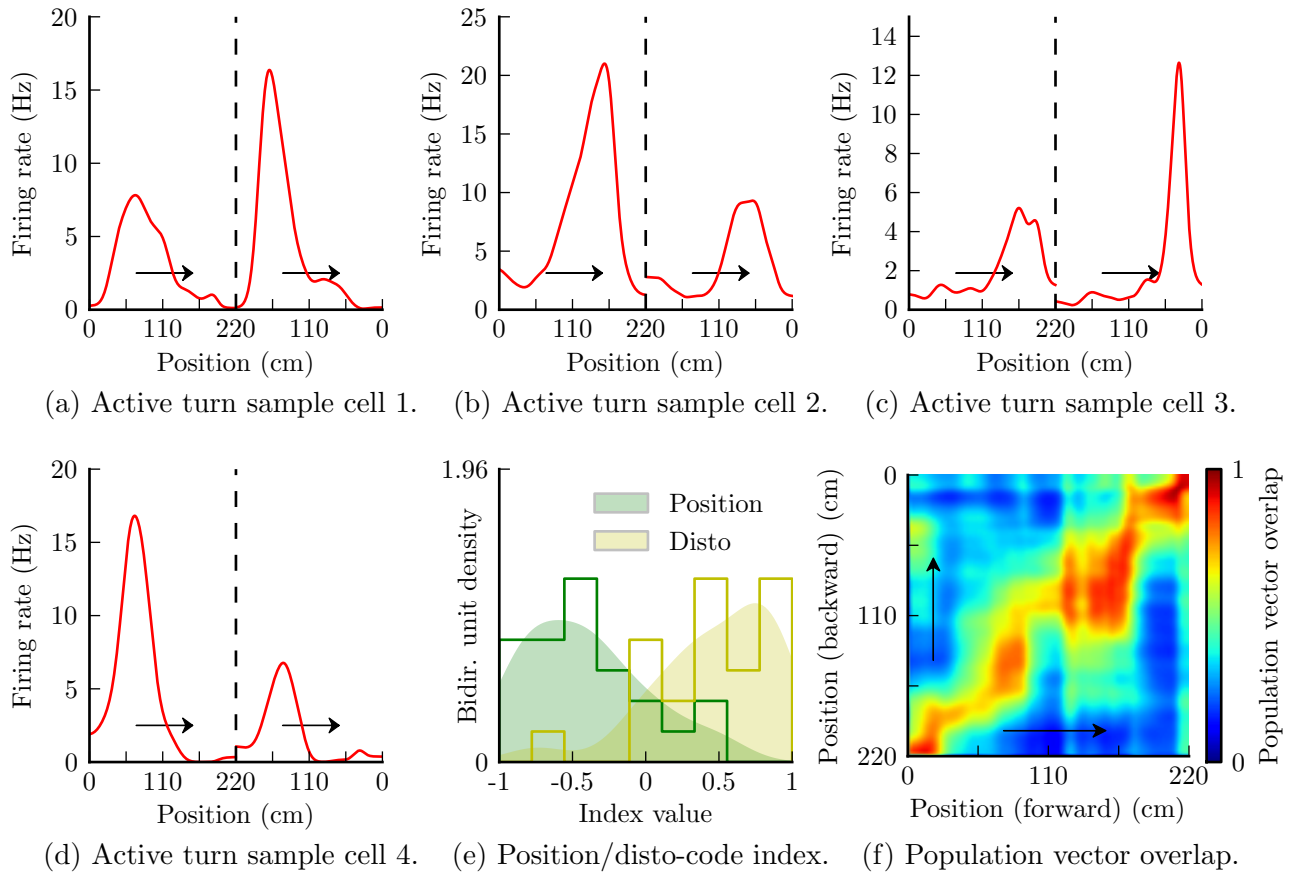


Figure 4.23: The disto-code persists under the active turning control protocol. Ratemaps from four sample cells exhibit clear disto coding. The position-code index (-0.30 ± 0.08 , $p = 4.6 \times 10^{-3}$, sign-rank test) was significantly weaker than the dominant disto-code index (0.5 ± 0.07 , $p = 6.0 \times 10^{-5}$, sign-rank test), a result confirmed by the 45° diagonal in the population vector.

4.7 Same cell comparisons

While comparisons of population statistics are interesting, ideally one would like to compare the same individual cells in VR and RW. Such a comparison could, for example, demonstrate whether the disto-coding and position-coding bidirectional cells are different subpopulations, or whether the same cell can express both coding schemes depending on the inputs.

As mentioned in section 1.1, it is difficult to identify cells across multiple recordings with a high level of certainty. On days where the rats were run in both VR and RW environments cell identification was performed by overlaying cluster boundaries from one session on spike data from the second and manually identifying clear overlaps. If electrode drift or other factors rendered the identification ambiguous, no cells from either session were used for same cell analysis. In all, 40 cells were reliably identified as being active in both VR and RW recording sessions on the same day.

Given the literature on importance of distal visual cues, which are identical in VR and RW, one might expect that these cells would fire in a similar fashion in both the virtual and real environments. To assess the similarity of two ratemaps we use two approaches: the correlation coefficient, and the Hellinger distance [177] between the (normalized) ratemaps. The Hellinger distance is a measure of the similarity between two probability distributions, and is defined (with $f(x)$ and $g(x)$ the density functions) as:

$$H(f, g) = \sqrt{\frac{1}{2} \int \left(\sqrt{f(x)} - \sqrt{g(x)} \right)^2 dx} \quad (4.24)$$

So applied to ratemaps $\lambda_1(x)$ and $\lambda_2(x)$, we obtain

$$H(\lambda_1, \lambda_2) = \sqrt{\frac{1}{2} \int \left(\sqrt{\frac{\lambda_1(x)}{\int \lambda_1(x') dx'}} - \sqrt{\frac{\lambda_2(x)}{\int \lambda_2(x') dx'}} \right)^2 dx}. \quad (4.25)$$

By computing the measures for pairs of cells that cannot be the same cell (such as cells recorded on different tetrodes), we obtain an estimate of the distribution of these two similarity measures under the null hypothesis that the same cell's VR and RW ratemaps are no

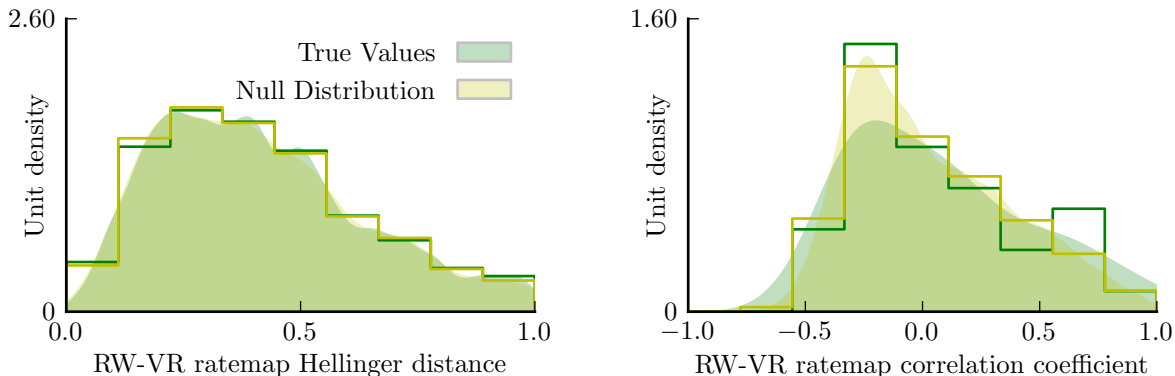


Figure 4.24: VR and RW ratemaps for cells reliably identified as the same did not exhibit similarity significantly above chance level using either a correlation measure ($p = 0.61$, rank-sum test) or Hellinger distance ($p = 0.8$, rank-sum test).

more similar than the ratemaps of random cell pairs. Surprisingly, neither measure’s distribution for the true cell pairs are significantly different from the null distribution (figure 4.24), a result which reinforces the importance of multi modal sensory stimuli to the activity of hippocampal pyramidal cells. Six sample cells in VR and RW are presented in figure 4.26.

Is there no relationship between the same cell’s firing in VR and RW then? Using a similar shuffling procedure to compute a null distribution for other ratemap metrics, we find that the firing rate (figure 4.25a), information content (figure 4.25b), and directionality index (figure 4.25c) all exhibit significant correlation between VR and RW. This paradoxical result suggests that to some extent these properties may be either ‘hard wired’ in the circuit, or determined by distal visual cues or self motion cues which are identical in VR and RW. As a result, a cell’s level of spatial and directional tuning is predictable, but exactly where it fires is dependent on particular environmental cues. Trying to compare the same cells on linear tracks in multiple rooms would test this finding without any potential concerns about the role of virtual reality.

It is worth noting that within the same cells the disto-index was reliably larger in VR than in RW (figure 4.25e), while the position-code index was larger in RW than VR (figure 4.25d). This suggests that the same cell is capable of expressing both coding schemes, depending

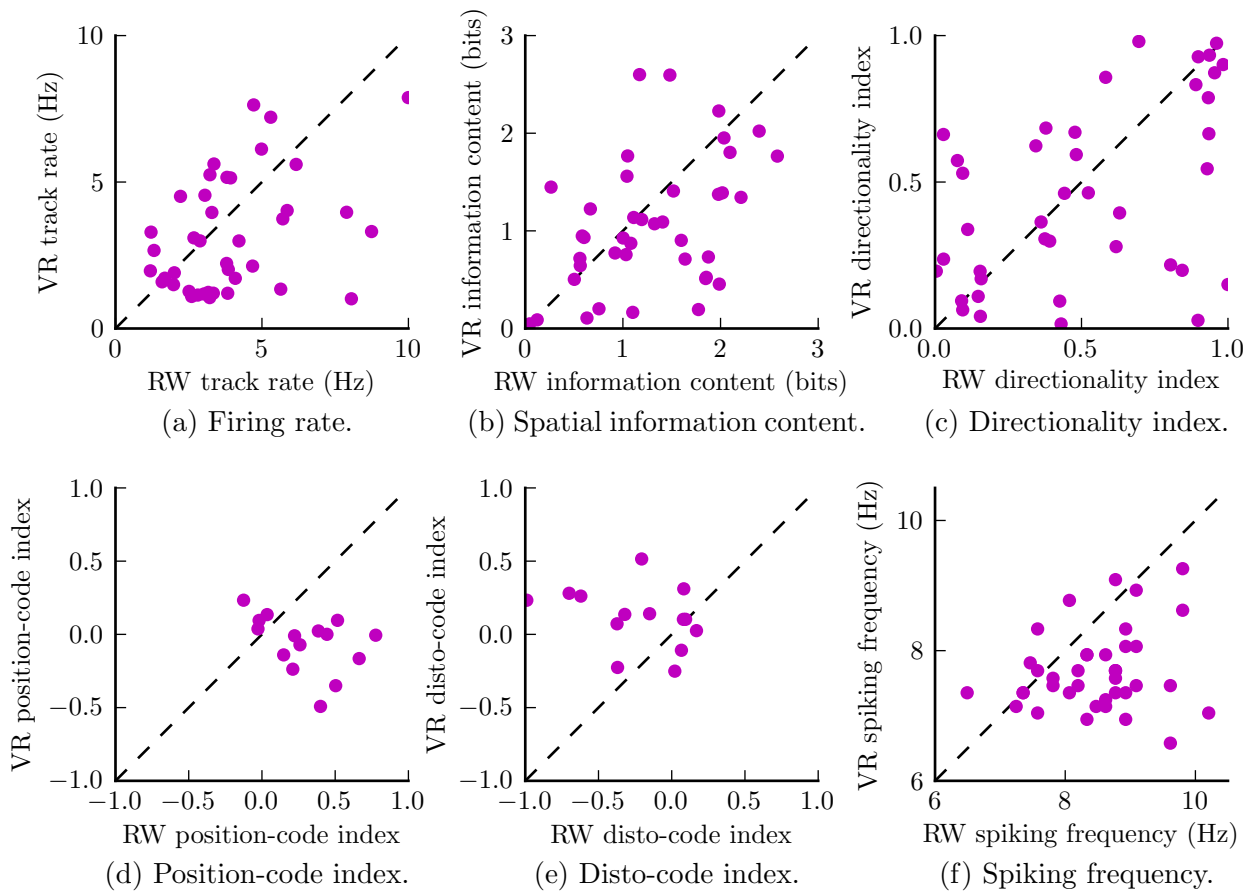


Figure 4.25: Comparison of cell properties in VR and RW for cells which could be reliably identified as the same cell in both sessions. Significant correlations between VR and RW were observed for firing rate (corr. coeff = 0.4, $p = 0.011$), spatial information content (corr. coeff = 0.43, $p = 6.1 \times 10^{-3}$), and directionality index (corr. coeff = 0.49, $p = 1.5 \times 10^{-3}$). No significant RW-VR correlation were observed for position-code index ($p = 0.19$), disto-code index ($p = 0.3$), or spike frequency ($p = 0.24$). Position-code index was reliably larger in RW, disto-code index reliably larger in VR, and spiking frequency reduced in VR.

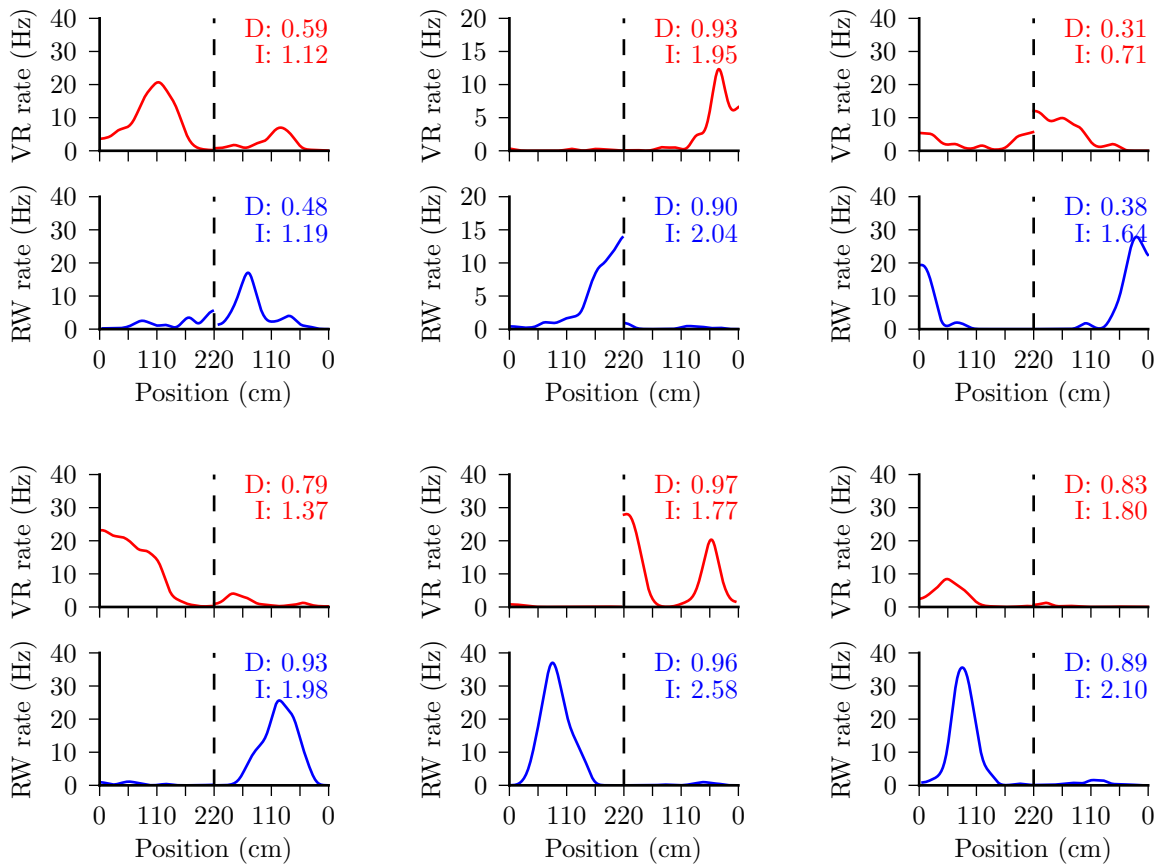


Figure 4.26: Six sample cells which were reliably identified in both VR (red) and RW (blue). While the directionality index and spatial information content were correlated across the two environments, the ratemaps were not similar despite the consistent distal visual cues in VR and RW. Directionality index and information is indicated in each case.

on the available stimuli. Spiking frequency was reduced in VR for the majority of cells, but the absence of significant correlation in the spiking frequency in two environments suggests that the spike frequency is not an intrinsic cell property, but rather a consequence of phase precession.

CHAPTER 5

Conclusion

5.1 Summary and discussion

Despite forty years of study, the mechanisms generating place cell activity in the hippocampus remain poorly understood. In part this is the result of challenges in recording single unit activity, and controlling multi-sensory stimuli in experimental paradigms.

The spike sorting problem in extracellular recording has similarly been the focus of considerable research effort. However, there is a disconnect between much of the literature, which tests primarily on synthetic single electrode datasets with a few thousand spikes, and practical application in hippocampal electrophysiology, where hundreds of thousands of spikes are not uncommon on a single tetrode. Feature extraction methods such as graph Laplacian features [86] and clustering algorithms such as dominant sets [108] show great promise on small datasets, but have an algorithmic complexity much too large to be applied to large hippocampal datasets. On the other end of the spectrum various on-line sorting algorithms, such as those based on matched filters [100] allow for fast execution, but necessarily compromise on sorting accuracy. By combining existing mixture based methods [111] with post processing heuristics similar to those employed by human operators I have developed a sorting algorithm which produces sorting results comparable to those of skilled human operators in a systematic and automated manner. This algorithm was combined with a feature rich software tool for manual sorting or inspection and modification of automated sorting results to significantly reduce both the time required to sort hippocampal tetrode data, as well as the subjectivity in the sorting process.

In recent years there has been significant interest in the use of virtual reality systems to enable the use of head fixed recording techniques such as patch clamp or optical methods in behaving animals [67, 178–180]. The type of experiments possible within these virtual reality setups has been limited to simple linear tracks, and the systems have several drawbacks including the inability to provide precise auditory stimuli and the fact that surgical implantation of a head fixing plate must be performed before animals can be trained on the system.

In contrast, the virtual reality system we have developed is much less invasive (though it can be easily extended to head-fixed recording if required). The display of grooming behavior in the VR is evidence of low level of stress in the rats using the harness fixing system. The addition of realistic positional auditory stimuli together with a much larger visual field of view creates a more immersive system (figure 3.1). Combined with expanded software this has enabled the study of interesting virtual environments such as a virtual ‘water maze’ task (figures 3.9 and 3.10), and foraging behavior with spherical boundary conditions (figure 3.11). The addition of lick detection capability has revealed an interesting dissociation between the spatial information in navigation and reward checking behavior, which are differently modulated by visual and auditory cues.

While there is much to learn from membrane potential recordings of place cells and grid cells, before results from virtual reality experiments can be properly interpreted a control study is necessary to determine whether, based on standard extracellular recordings, place cells in virtual reality are comparable to their real world counterparts.

Results from this comparison between the real and virtual linear tracks reveals several important aspects of the sensory mechanisms affecting hippocampal activity, and are consistent with recent studies [181]. In both VR and RW an overwhelming majority of pyramidal neurons displayed significant spatial selectivity, and phase precession was comparable between VR and RW. This demonstrates that a robust cognitive map can be generated by in environments where only purely visual cues provide spatial information. Despite this comparisons of the same cell in VR and RW reveal that while visual cues are sufficient to generate

place fields, they are not sufficient to provide identical representations in environments where visual cues are highly similar but other sensory cues differ [71].

The results are unlikely to be due to the small differences in the visual cues between the real and virtual conditions, but rather the absence of spatial information in other sensory modalities. When combined with the observation that roughly half the cell population shuts down in VR, this suggests that subpopulations of hippocampal cells preferentially respond to different sensory modalities. With the advent of substantial interest in the use of virtual reality to enable intracellular recording during behavior [67, 178–180], it is thus important to keep in mind that such studies may be selectively sampling a subpopulation of cells.

Bidirectional cells switch from a position based representation in RW to a distance based representation in VR, which is analogous to previous reports of different hippocampal cell response types based upon task demand [116]. Such observations could imply either the existence of distinct classes of cells, or adaptability of single units to alternate task demands. Given the observation that cells which are active in both VR and RW exhibit both distance and position coding schemes depending on the environment the latter possibility seems more likely. One potential explanation for the appearance of the distance-code may be that the virtual reality apparatus provides insufficient information for the rat to grasp that the virtual linear track is in fact the same environment viewed from two orientations. This explanation seems unlikely given the persistence of the distance-code in the active turning control experiment, together with the comparable level of direction selectivity in VR and RW. When considered together with the observations of position coding in RW [168] which is enhanced by the addition of odors and textures [73], these results argue that the bidirectional position code observed in RW is likely generated by the presence of proximal cues on the track. The distance-code observed in VR, by contrast, is likely generated by self motion cues such as proprioception and optic flow, which are the only cues which are similar in both running directions.

Distance-coding has been reported on a single unit level in RW [115, 169], but the dominant population coding effect in RW is position based [73]. Our data did not contain a significant

number of disto-coding cells in the RW population. The absence of such population level disto-coding suggests that the proximal cues exert a veto over self-motion cues in determining the bidirectional coding scheme. Such competitive effects between different sensory modalities may be driven by inhibitory mechanisms across multi-modal inputs, as seen recently in the primary visual cortex [182].

Observations of lateral entorhinal cortex neurons responding to local cues such as objects [183], and spatial selective activity of medial entorhinal cortex neurons [114], which are two of the primary inputs to the hippocampus, lead us to hypothesize that the visual and self-motion cues driving activity in VR reach CA1 via MEC, while proximal cues driving bidirectional position coding in RW reach CA1 via LEC. Consistent with this hypothesis, while both LEC and MEC project directly and indirectly to CA1 they modulated CA1 activity during sleep differently [184] and engage local inhibition [185]. Inhibitory effects between the MEC and LEC pathways may thus be the origin of the competitive interactions responsible for the disto-position coding switch.

Theta frequency was significantly reduced in VR, corroborating earlier results that vestibular inputs contribute to theta frequency [172], and its speed dependence was abolished. On the other hand, theta power had similar speed dependence in VR and RW suggesting that theta power is largely governed by distal visual and self-motion cues. Despite the large changes in theta frequency and its speed dependence, phase precession was intact in VR [67], and its quality was identical in RW and VR, indicating that distal visual and self-motion cues are sufficient to generate a robust temporal code. These results place restrictions on theories of phase precession that depend on the precise value of theta frequency or its speed dependence [25, 173–175]. Instead they favor alternative mechanisms that are insensitive to these phenomena [29, 60, 66], that apply equally to networks with diverse connectivity patterns such as the entorhinal cortex and CA1, and hence do not require recurrent excitatory connections [29, 66].

5.2 Future work

With reliable systematic spike sorting of hippocampal tetrode data being achieved, there are two more important challenges to overcome. Most important in the short term is the identification of the same cell across multiple recording sessions. Such identification is crucial for studies of long term changes in circuit behavior, as well as phenomena like sleep-replay [32–34], but at present is possible only for extremely well isolated single units. Solving this problem will likely require a better way to handle electrode drift within a recording session, and extrapolating the drift activity between two sessions. In the long term it would be ideal to be able to determine the spatial position, relative to the electrode, of the neurons recorded from. With recent advances in structural imaging techniques [186] such spatial information would make it possible to map the structural connectivity of cells after electrophysiological recording is completed. On-line spike sorting is important in brain machine interface problems, but is of lesser concern unless the experimental paradigm requires real time experimental response to neural activity.

Several technical improvements to the virtual reality system are possible, though challenging, and may significantly improve both the immersive quality of virtual environments as well as the range of possible manipulations. In non head fixed systems, real time tracking of the animals head position will enable the addition of subtle perspective changes to recreate depth perception, which due to the small binocular region is achieved in rodents primarily through head bobbing activity. The addition of spatially realistic scent cues may be possible through the combination of motorized valve olfactometers with the virtual reality software, although there are significant challenges as a result of the relatively slow speed at which scents diffuse through air. Even more ambitious, but not impossible, would be the reintroduction of vestibular cues by tilting the entire system to use gravitational acceleration. A much less glamorous improvement, which is extremely important, would be standardizing on system design and software, so that experiments can be accurately reproduced between different labs using virtual reality technology.

These results from the place cell control experiment on the virtual linear track suggest several further experiments to gain a better understanding of the mechanisms generating place cell activity. Several of these experiments could clarify the role of various sensory stimuli in the current experiment. The first of these is to use chemical or optogenetic methods to selectively inhibit input from different sensory modalities, particularly those that do not provide spatial information in VR, on the real linear track and see if similar phenomena are observed in their absence.

A second continuation experiment would be to reproduce the experiment using a swivel based VR system in which rotational vestibular cues are in tact. Such a system could not be used for head fixed recordings, and would likely take non-trivial effort to develop, but such an experiment could definitely disambiguate the role of rotational vestibular cues vs proximal cues in the disto/position coding switch observed in VR. Manipulating the ‘gain’ of the spherical treadmill, i.e. the ratio between the distance the rat runs on the physical sphere and the distance traveled in the virtual environment, provides a means to more conclusively separate the role of distance and time in the disto-coding result.

Moving beyond the linear track paradigm, the two dimensional virtual foraging task provides a paradigm where the relationship between distance and position is much less stereotyped, and the two can be further disambiguated. Once a better understanding of the differences between cell responses in virtual reality has been achieved, the virtual water maze and spherical foraging tasks provide unique opportunities to perform recordings from place cells in conditions which are extraordinarily difficult to do in the real world. Combined with lick detection data to measure reward expectancy such experiments may reveal much about the nature of spatial memory.

Virtual reality provides tremendous opportunity for novel experimental paradigms, the largest challenge in future work may ultimately be in understanding to what extent results obtained in virtual reality can be applied to the real world.

REFERENCES

- [1] A. L. Hodgkin, A. F. Huxley, and B. Katz, “Measurement of current-voltage relations in the membrane of the giant axon of *Loligo*,” *The Journal of physiology*, vol. 116, pp. 424–48, Apr. 1952.
- [2] G. Ling and R. Gerard, “The normal membrane potential of frog sartorius fibers,” *Journal of cellular and comparative physiology*, vol. 34, no. 3, pp. 383–396, 1949.
- [3] O. P. Hamill, A. Marty, E. Neher, B. Sakmann, and F. J. Sigworth, “Improved patch-clamp techniques for high-resolution current recording from cells and cell-free membrane patches,” *Pflügers Archiv : European journal of physiology*, vol. 391, pp. 85–100, Aug. 1981.
- [4] U. Mitzdorf, “Current source-density method and application in cat cerebral cortex: investigation of evoked potentials and EEG phenomena.,” *Physiological Reviews*, vol. 65, no. 1, pp. 37–100, 1985.
- [5] C. M. Gray and W. Singer, “Stimulus-specific neuronal oscillations in orientation columns of cat visual cortex.,” *Proceedings of the National Academy of Sciences of the United States of America*, vol. 86, no. 5, pp. 1698–1702, 1989.
- [6] L. Avitan, M. Teicher, and M. Abeles, “EEG generator—a model of potentials in a volume conductor.,” *Journal of Neurophysiology*, vol. 102, no. 5, pp. 3046–3059, 2009.
- [7] S. Katzner, I. Nauhaus, A. Benucci, V. Bonin, D. L. Ringach, and M. Carandini, “Local Origin of Field Potentials in Visual Cortex,” *Neuron*, vol. 61, no. 1, pp. 35–41, 2009.
- [8] D. Xing, C.-I. Yeh, and R. M. Shapley, “Spatial spread of the local field potential and its laminar variation in visual cortex.,” *Journal of Neuroscience*, vol. 29, no. 37, pp. 11540–11549, 2009.
- [9] D. A. Henze, Z. Borhegyi, J. Csicsvari, A. Mamiya, K. D. Harris, and G. Buzsáki, “Intracellular features predicted by extracellular recordings in the hippocampus in vivo.,” *Journal of Neurophysiology*, vol. 84, no. 1, pp. 390–400, 2000.
- [10] M. Abeles and M. H. J. Goldstein, “Multispikes train analysis,” 1977.
- [11] K. D. Harris, D. A. Henze, J. Csicsvari, H. Hirase, and G. Buzsaki, “Accuracy of Tetrode Spike Separation as Determined by Simultaneous Intracellular and Extracellular Measurements,” *Journal of Neurophysiology*, vol. 84, pp. 401–414, July 2000.
- [12] F. Wood, M. J. Black, C. Vargas-Irwin, M. Fellows, and J. P. Donoghue, “On the variability of manual spike sorting,” 2004.

- [13] C. M. Gray, P. E. Maldonado, M. Wilson, and B. McNaughton, “Tetrodes markedly improve the reliability and yield of multiple single-unit isolation from multi-unit recordings in cat striate cortex.,” *Journal of Neuroscience Methods*, vol. 63, no. 1-2, pp. 43–54, 1995.
- [14] W. B. Scoville and B. Milner, “Loss of recent memory after bilateral hippocampal lesions.,” *The Journal of neuropsychiatry and clinical neurosciences*, vol. 12, no. 1, pp. 103–113, 1957.
- [15] L. R. Squire, “Memory and the hippocampus: a synthesis from findings with rats, monkeys, and humans.,” *Psychological Review*, vol. 99, no. 2, pp. 195–231, 1992.
- [16] N. J. Cohen and H. Eichenbaum, *Memory, Amnesia, and the Hippocampal System*. MIT Press, 1993.
- [17] J. O’Keefe and J. Dostrovsky, “The hippocampus as a spatial map: Preliminary evidence from unit activity in the freely-moving rat.,” *Brain Research*, vol. 34, pp. 171–175, 1971.
- [18] J. O’keefe and L. Nadel, *The hippocampus as a cognitive map*. Oxford: Clarendon Press, 1978.
- [19] J. O’Keefe, “A review of the hippocampal place cells.,” *Prog Neurobiol*, vol. 13, no. 4, pp. 419–439, 1979.
- [20] M. W. Jung and B. L. McNaughton, “Spatial selectivity of unit activity in the hippocampal granular layer.,” *Hippocampus*, vol. 3, no. 2, pp. 165–182, 1993.
- [21] M. A. Wilson and B. L. McNaughton, “Dynamics of the hippocampal ensemble code for space.,” *Science*, vol. 261, no. 5124, pp. 1055–1058, 1993.
- [22] M. W. Jung, S. I. Wiener, and B. L. McNaughton, “Comparison of spatial firing characteristics of units in dorsal and ventral hippocampus of the rat.,” *Journal of Neuroscience*, vol. 14, no. 12, pp. 7347–7356, 1994.
- [23] O. J. Ahmed and M. R. Mehta, “The hippocampal rate code: anatomy, physiology and theory.,” *Trends in Neurosciences*, vol. 32, no. 6, pp. 329–338, 2009.
- [24] R. Muller, “A Quarter of a Century of Place Cells,” *Neuron*, vol. 17, no. 5, pp. 813–822, 1996.
- [25] J. O’Keefe and M. Recce, “Phase relationship between hippocampal place units and the EEG theta rhythm,” *Hippocampus*, vol. 3, no. 3, pp. 317–30., 1993.
- [26] E. J. Markus, Y. L. Qin, B. Leonard, W. E. Skaggs, B. L. McNaughton, and C. A. Barnes, “Interactions between location and task affect the spatial and directional firing of hippocampal neurons.,” *Journal of Neuroscience*, vol. 15, no. 11, pp. 7079–7094, 1995.

- [27] R. G. Morris, P. Garrud, J. N. Rawlins, and J. O'Keefe, "Place navigation impaired in rats with hippocampal lesions.," *Nature*, vol. 297, no. 5868, pp. 681–683, 1982.
- [28] M. R. Mehta, C. A. Barnes, and B. L. McNaughton, "Experience-dependent, asymmetric expansion of hippocampal place fields.," *Proceedings of the National Academy of Sciences of the United States of America*, vol. 94, no. 16, pp. 8918–8921, 1997.
- [29] M. Mehta, M. Quirk, and M. Wilson, "Experience-dependent asymmetric shape of hippocampal receptive fields," *Neuron*, vol. 25, no. 3, pp. 707–15., 2000.
- [30] G. Q. Bi and M. M. Poo, "Synaptic modifications in cultured hippocampal neurons: dependence on spike timing, synaptic strength, and postsynaptic cell type.," *Journal of Neuroscience*, vol. 18, no. 24, pp. 10464–10472, 1998.
- [31] H. Markram, J. Lübke, M. Frotscher, and B. Sakmann, "Regulation of synaptic efficacy by coincidence of postsynaptic APs and EPSPs.," *Science*, vol. 275, no. 5297, pp. 213–215, 1997.
- [32] Z. Nádasdy, H. Hirase, A. Czurkó, J. Csicsvari, and G. Buzsáki, "Replay and time compression of recurring spike sequences in the hippocampus.," *Journal of Neuroscience*, vol. 19, no. 21, pp. 9497–9507, 1999.
- [33] A. K. Lee and M. A. Wilson, "Memory of sequential experience in the hippocampus during slow wave sleep.," *Neuron*, vol. 36, no. 6, pp. 1183–1194, 2002.
- [34] T. J. Davidson, F. Kloosterman, and M. A. Wilson, "Hippocampal replay of extended experience.," *Neuron*, vol. 63, no. 4, pp. 497–507, 2009.
- [35] B. McNaughton, C. Barnes, and J. O'keefe, "The contributions of position, direction, and velocity to single unit activity in the hippocampus of freely-moving rats," *Experimental Brain Research*, vol. 52, no. 1, pp. 41–49, 1983.
- [36] S. I. Wiener, C. A. Paul, and H. Eichenbaum, "Spatial and behavioral correlates of hippocampal neuronal activity.," *Journal of Neuroscience*, vol. 9, no. 8, pp. 2737–2763, 1989.
- [37] P. E. Sharp, J. L. Kubie, and R. U. Muller, "Firing properties of hippocampal neurons in a visually symmetrical environment: contributions of multiple sensory cues and mnemonic processes.," *Journal of Neuroscience*, vol. 10, no. 9, pp. 3093–3105, 1990.
- [38] K. Zhang, I. Ginzburg, B. L. McNaughton, and T. J. Sejnowski, "Interpreting neuronal population activity by reconstruction: unified framework with application to hippocampal place cells.," *Journal of Neurophysiology*, vol. 79, no. 2, pp. 1017–1044, 1998.
- [39] G. M. Muir and D. K. Bilkey, "Theta- and movement velocity-related firing of hippocampal neurons is disrupted by lesions centered on the perirhinal cortex.," *Hippocampus*, vol. 13, no. 1, pp. 93–108, 2003.

- [40] X. Lu and D. K. Bilkey, “The velocity-related firing property of hippocampal place cells is dependent on self-movement.,” *Hippocampus*, vol. 20, no. 5, pp. 573–583, 2010.
- [41] J. B. Ranck, “Studies on single neurons in dorsal hippocampal formation and septum in unrestrained rats: I. behavioral correlates and firing repertoires.,” *Experimental neurology*, 1973.
- [42] H. Eichenbaum, M. Kuperstein, A. Fagan, and J. Nagode, “Cue-sampling and goal-approach correlates of hippocampal unit activity in rats performing an odor-discrimination task.,” *Journal of Neuroscience*, vol. 7, no. 3, pp. 716–732, 1987.
- [43] T. Kobayashi, H. Nishijo, M. Fukuda, J. Bures, and T. Ono, “Task-dependent representations in rat hippocampal place neurons.,” *Journal of Neurophysiology*, vol. 78, no. 2, pp. 597–613, 1997.
- [44] E. Wood, P. Dudchenko, and H. Eichenbaum, “The global record of memory in hippocampal neuronal activity,” *Nature*, vol. 397, no. 6720, pp. 613–6., 1999.
- [45] C. Hölscher, W. Jacob, and H. A. Mallot, “Reward modulates neuronal activity in the hippocampus of the rat.,” *Behavioural Brain Research*, vol. 142, no. 1-2, pp. 181–191, 2003.
- [46] S. A. Ho, E. Hori, T. Kobayashi, K. Umeno, A. H. Tran, T. Ono, and H. Nishijo, “Hippocampal place cell activity during chasing of a moving object associated with reward in rats.,” *Neuroscience*, vol. 157, no. 1, pp. 254–270, 2008.
- [47] J. L. Kubie, R. U. Muller, *et al.*, “Multiple representations in the hippocampus,” *Hippocampus*, vol. 1, no. 3, pp. 240–242, 1991.
- [48] J. D. Green and A. A. Arduini, “Hippocampal electrical activity in arousal,” *Journal of Neurophysiology*, vol. 17, no. 6, pp. 533–557, 1954.
- [49] J. J. Hopfield, “Pattern recognition computation using action potential timing for stimulus representation.,” *Nature*, vol. 376, no. 6535, pp. 33–36, 1995.
- [50] R. Schmidt, K. Diba, C. Leibold, D. Schmitz, G. Buzsáki, and R. Kempter, “Single-trial phase precession in the hippocampus.,” *Journal of Neuroscience*, vol. 29, no. 42, pp. 13232–13241, 2009.
- [51] J. Huxter, N. Burgess, and J. O’Keefe, “Independent rate and temporal coding in hippocampal pyramidal cells,” *Nature*, vol. 425, no. 6960, pp. 828–832, 2003.
- [52] C. Geisler, D. Robbe, M. Zugaro, A. Sirota, and G. Buzsáki, “Hippocampal place cell assemblies are speed-controlled oscillators,” *Proceedings of the National Academy of Sciences of the United States of America*, vol. 104, no. 19, pp. 8149–8154, 2007.
- [53] J. R. Huxter, T. J. Senior, K. Allen, and J. Csicsvari, “Theta phase-specific codes for two-dimensional position, trajectory and heading in the hippocampus.,” *Nature Neuroscience*, vol. 11, no. 5, pp. 587–94, 2008.

- [54] W. Skaggs and B. McNaughton, “Theta phase precession in hippocampal neuronal populations and the compression of temporal sequences,” *Hippocampus*, vol. 6, no. 2, pp. 149–172, 1996.
- [55] K. I. Blum and L. F. Abbott, “A model of spatial map formation in the hippocampus of the rat.,” *Neural Computation*, vol. 8, no. 1, pp. 85–93, 1996.
- [56] G. Dragoi and G. Buzsáki, “Temporal encoding of place sequences by hippocampal cell assemblies.,” *Neuron*, vol. 50, no. 1, pp. 145–157, 2006.
- [57] T. Hafting, M. Fyhn, T. Bonnevie, M. Moser, and E. Moser, “Hippocampus-independent phase precession in entorhinal grid cells,” *Nature*, vol. 453, no. 7199, pp. 1248–1252, 2008.
- [58] T. Klausberger and P. Somogyi, “Neuronal diversity and temporal dynamics: the unity of hippocampal circuit operations.,” *Science*, vol. 321, no. 5885, pp. 53–57, 2008.
- [59] M. Lengyel, Z. Szatmáry, and P. Erdi, “Dynamically detuned oscillations account for the coupled rate and temporal code of place cell firing.,” *Hippocampus*, vol. 13, no. 6, pp. 700–714, 2003.
- [60] M. Tsodyks and W. Skaggs, “Population dynamics and theta rhythm phase precession of hippocampal place cell firing: a spiking neuron model,” *Hippocampus*, vol. 6, no. 3, pp. 271–280, 1998.
- [61] O. Jensen and J. E. Lisman, “Hippocampal CA3 region predicts memory sequences: accounting for the phase precession of place cells.,” *Learning & Memory*, vol. 3, no. 2-3, pp. 279–287, 1996.
- [62] A. Kamondi, L. Acsády, X. J. Wang, and G. Buzsáki, “Theta oscillations in somata and dendrites of hippocampal pyramidal cells in vivo: activity-dependent phase-precession of action potentials.,” *Hippocampus*, vol. 8, no. 3, pp. 244–261, 1998.
- [63] J. C. Magee, “Dendritic mechanisms of phase precession in hippocampal CA1 pyramidal neurons.,” *Journal of neurophysiology*, vol. 86, pp. 528–32, July 2001.
- [64] M. R. Mehta and M. A. Wilson, “From hippocampus to V1: Effect of LTP on spatio-temporal dynamics of receptive fields,” *Neurocomputing*, vol. 32-33, pp. 905–911, June 2000.
- [65] M. R. Mehta, “Neuronal Dynamics of Predictive Coding,” *The Neuroscientist*, vol. 7, pp. 490–495, Dec. 2001.
- [66] M. R. Mehta, A. K. Lee, and M. A. Wilson, “Role of experience and oscillations in transforming a rate code into a temporal code.,” *Nature*, vol. 417, pp. 741–6, June 2002.

- [67] C. D. Harvey, F. Collman, D. A. Dombeck, and D. W. Tank, “Intracellular dynamics of hippocampal place cells during virtual navigation,” *Nature*, vol. 461, pp. 941–6, Oct. 2009.
- [68] R. Muller and J. Kubie, “The effects of changes in the environment on the spatial firing of hippocampal complex-spike cells,” *The Journal of Neuroscience*, vol. 7, no. 7, pp. 1951–68., 1987.
- [69] G. J. Quirk, R. U. Muller, and J. L. Kubie, “The firing of hippocampal place cells in the dark depends on the rat’s recent experience.,” *Journal of Neuroscience*, vol. 10, no. 6, pp. 2008–2017, 1990.
- [70] E. Save, A. Cressant, C. Thinus-Blanc, and B. Poucet, “Spatial firing of hippocampal place cells in blind rats.,” *Journal of Neuroscience*, vol. 18, no. 5, pp. 1818–26, 1998.
- [71] H. Tanila, “Hippocampal place cells can develop distinct representations of two visually identical environments.,” *Hippocampus*, vol. 9, no. 3, pp. 235–246, 1999.
- [72] E. Save, L. Nerad, and B. Poucet, “Contribution of multiple sensory information to place field stability in hippocampal place cells,” *Hippocampus*, vol. 10, no. 1, pp. 64–76, 2000.
- [73] F. P. Battaglia, G. R. Sutherland, and B. L. McNaughton, “Local sensory cues and place cell directionality: additional evidence of prospective coding in the hippocampus,” *The Journal of Neuroscience*, vol. 24, no. 19, pp. 4541–4550, 2004.
- [74] R. W. Stackman and J. S. Taube, “Firing properties of head direction cells in the rat anterior thalamic nucleus: dependence on vestibular input.,” *Journal of Neuroscience*, vol. 17, no. 11, pp. 4349–4358, 1997.
- [75] R. Stackman, A. Clark, and J. Taube, “Hippocampal spatial representations require vestibular input,” *Hippocampus*, vol. 12, no. 3, pp. 291–303, 2002.
- [76] P. Ravassard, A. Kees, B. Willers, D. Ho, D. A. Aharoni, J. Cushman, Z. M. Aghajan, and M. R. Mehta, “Multisensory Control of Hippocampal Spatiotemporal Selectivity.,” *Science (New York, N.Y.)*, May 2013.
- [77] A. B. Wiltschko, G. J. Gage, and J. D. Berke, “Wavelet filtering before spike detection preserves waveform shape and enhances single-unit discrimination.,” *Journal of Neuroscience Methods*, vol. 173, pp. 34–40, Aug. 2008.
- [78] R. Quiñan Quiroga, “What is the real shape of extracellular spikes?,” *Journal of Neuroscience Methods*, vol. 177, pp. 194–8, Feb. 2009.
- [79] S. Butterworth, “On the theory of filter amplifiers,” *Wireless Engineer*, vol. 7, pp. 536–541, 1930.

- [80] K. H. Kim and S. J. Kim, “Neural spike sorting under nearly 0-dB signal-to-noise ratio using nonlinear energy operator and artificial neural-network classifier,” *IEEE transactions on bio-medical engineering*, vol. 47, pp. 1406–11, Oct. 2000.
- [81] M. S. Fee, P. P. Mitra, and D. Kleinfeld, “Variability of extracellular spike waveforms of cortical neurons.,” *Journal of Neurophysiology*, vol. 76, no. 6, pp. 3823–3833, 1996.
- [82] T. J. Blanche and N. V. Swindale, “Nyquist interpolation improves neuron yield in multiunit recordings.,” *Journal of Neuroscience Methods*, vol. 155, no. 1, pp. 81–91, 2006.
- [83] D. A. Adamos, N. A. Laskaris, E. K. Kosmidis, and G. Theophilidis, “NASS: An empirical approach to spike sorting with overlap resolution based on a hybrid noise-assisted methodology.,” *Journal of Neuroscience Methods*, vol. 190, pp. 129–42, Apr. 2010.
- [84] J. B. Tenenbaum, V. De Silva, and J. C. Langford, “A global geometric framework for nonlinear dimensionality reduction.,” *Science*, vol. 290, no. 5500, pp. 2319–23, 2000.
- [85] M. Belkin and P. Niyogi, “Laplacian Eigenmaps for Dimensionality Reduction and Data Representation,” *Neural Computation*, vol. 15, no. 6, pp. 1373–1396, 2003.
- [86] Y. Ghanbari, P. E. Papamichalis, and L. Spence, “Graph-laplacian features for neural waveform classification.,” *IEEE transactions on bio-medical engineering*, vol. 58, pp. 1365–72, May 2011.
- [87] S. Mallat, “A theory for multiresolution signal decomposition: the wavelet representation,” *IEEE Transactions on Pattern Analysis and Machine Intelligence*, vol. 11, pp. 674–693, July 1989.
- [88] R. Q. Quiroga, Z. Nadasdy, and Y. Ben-Shaul, “Unsupervised spike detection and sorting with wavelets and superparamagnetic clustering.,” *Neural computation*, vol. 16, pp. 1661–87, Aug. 2004.
- [89] J. C. Letelier and P. P. Weber, “Spike sorting based on discrete wavelet transform coefficients,” *Journal of Neuroscience Methods*, vol. 101, pp. 93–106, Sept. 2000.
- [90] T. H. Bullock, *Introduction to Nervous Systems*. 1977.
- [91] D. N. Hill, S. B. Mehta, and D. Kleinfeld, “Quality metrics to accompany spike sorting of extracellular signals.,” *The Journal of Neuroscience*, vol. 31, pp. 8699–705, July 2011.
- [92] T. J. McHugh, K. I. Blum, J. Z. Tsien, S. Tonegawa, and M. A. Wilson, “Impaired hippocampal representation of space in CA1-specific NMDAR1 knockout mice.,” *Cell*, vol. 87, no. 7, pp. 1339–1349, 1996.

- [93] E. R. Kandel and W. A. Spencer, “Electrophysiology of hippocampal neurons: II. After-potentials and repetitive firing,” *Journal of Neurophysiology*, vol. 24, pp. 243–259, May 1961.
- [94] K. D. Harris, H. Hirase, X. Leinekugel, D. A. Henze, and G. Buzsáki, “Temporal Interaction between Single Spikes and Complex Spike Bursts in Hippocampal Pyramidal Cells,” *Neuron*, vol. 32, pp. 141–149, Oct. 2001.
- [95] N. Schmitzer-Torbert, J. Jackson, D. Henze, K. Harris, and A. D. Redish, “Quantitative measures of cluster quality for use in extracellular recordings.,” *Neuroscience*, vol. 131, pp. 1–11, Jan. 2005.
- [96] M. S. Lewicki, “A review of methods for spike sorting: the detection and classification of neural action potentials.,” *Network*, vol. 9, no. 4, pp. R53–R78, 1998.
- [97] M. S. Fee, P. P. Mitra, and D. Kleinfeld, “Automatic sorting of multiple unit neuronal signals in the presence of anisotropic and non-Gaussian variability.,” *Journal of Neuroscience Methods*, vol. 69, no. 2, pp. 175–188, 1996.
- [98] C. Vargas-Irwin and J. P. Donoghue, “Automated spike sorting using density grid contour clustering and subtractive waveform decomposition.,” *Journal of Neuroscience Methods*, vol. 164, pp. 1–18, Aug. 2007.
- [99] T. Hermle, C. Schwarz, and M. Bogdan, “Employing ICA and SOM for spike sorting of multielectrode recordings from CNS.,” *Journal of physiology, Paris*, vol. 98, no. 4-6, pp. 349–56.
- [100] F. Franke, M. Natora, C. Boucsein, M. H. J. Munk, and K. Obermayer, “An online spike detection and spike classification algorithm capable of instantaneous resolution of overlapping spikes.,” *Journal of computational neuroscience*, vol. 29, pp. 127–48, Aug. 2010.
- [101] S. Takahashi, Y. Anzai, and Y. Sakurai, “A new approach to spike sorting for multi-neuronal activities recorded with a tetrode—how ICA can be practical.,” *Neuroscience research*, vol. 46, pp. 265–72, July 2003.
- [102] S. Takahashi, Y. Anzai, and Y. Sakurai, “Automatic sorting for multi-neuronal activity recorded with tetrodes in the presence of overlapping spikes.,” *Journal of Neurophysiology*, vol. 89, pp. 2245–58, Apr. 2003.
- [103] S. Takahashi and Y. Sakurai, “Real-time and automatic sorting of multi-neuronal activity for sub-millisecond interactions in vivo.,” *Neuroscience*, vol. 134, pp. 301–15, Jan. 2005.
- [104] S. Shoham, “Robust, automatic spike sorting using mixtures of multivariate t-distributions,” *Journal of Neuroscience Methods*, vol. 127, pp. 111–122, Aug. 2003.

- [105] T. Takekawa, Y. Isomura, and T. Fukai, “Accurate spike sorting for multi-unit recordings,” *The European journal of neuroscience*, vol. 31, pp. 263–72, Jan. 2010.
- [106] T. Takekawa, Y. Isomura, and T. Fukai, “Spike sorting of heterogeneous neuron types by multimodality-weighted PCA and explicit robust variational Bayes,” *Frontiers in neuroinformatics*, vol. 6, p. 5, Jan. 2012.
- [107] D. Ge, E. Le Carpentier, J. Idier, and D. Farina, “Spike sorting by stochastic simulation,” *IEEE transactions on neural systems and rehabilitation engineering : a publication of the IEEE Engineering in Medicine and Biology Society*, vol. 19, pp. 249–59, June 2011.
- [108] D. A. Adamos, N. A. Laskaris, E. K. Kosmidis, and G. Theophilidis, “In quest of the missing neuron: spike sorting based on dominant-sets clustering,” *Computer methods and programs in biomedicine*, vol. 107, pp. 28–35, July 2012.
- [109] F. Wood, S. Goldwater, and M. J. Black, “A non-parametric Bayesian approach to spike sorting,” *Conference proceedings : ... Annual International Conference of the IEEE Engineering in Medicine and Biology Society. IEEE Engineering in Medicine and Biology Society. Conference*, vol. 1, pp. 1165–8, Jan. 2006.
- [110] J. A. Herbst, S. Gammeter, D. Ferrero, and R. H. R. Hahnloser, “Spike sorting with hidden Markov models,” *Journal of Neuroscience Methods*, vol. 174, pp. 126–34, Sept. 2008.
- [111] K. D. Harris, “KlustaKwik,” 2002.
- [112] H. Akaike, “A new look at the statistical model identification,” *IEEE Transactions on Automatic Control*, vol. 19, pp. 716–723, Dec. 1974.
- [113] L. Hazan, M. Zugaro, and G. Buzsáki, “Klusters, NeuroScope, NDManager: a free software suite for neurophysiological data processing and visualization,” *Journal of Neuroscience Methods*, vol. 155, no. 2, pp. 207–216, 2006.
- [114] T. Hafting, M. Fyhn, S. Molden, M.-B. B. Moser, and E. I. Moser, “Microstructure of a spatial map in the entorhinal cortex,” *Nature*, vol. 436, pp. 801–6, Aug. 2005.
- [115] K. M. Gothard, W. E. Skaggs, K. M. Moore, and B. L. McNaughton, “Binding of hippocampal CA1 neural activity to multiple reference frames in a landmark-based navigation task,” *The Journal of Neuroscience*, vol. 16, no. 2, pp. 823–35., 1996.
- [116] E. Pastalkova, V. Itskov, A. Amarasingham, and G. Buzsáki, “Internally generated cell assembly sequences in the rat hippocampus,” *Science*, vol. 321, no. 5894, pp. 1322–1327, 2008.
- [117] P. M. Itskov, E. Vinnik, C. Honey, J. W. H. Schnupp, and M. E. Diamond, “Sound sensitivity of neurons in rat hippocampus during performance of a sound-guided task,” *Journal of Neurophysiology*, Jan. 2012.

- [118] B. Young, G. Fox, and H. Eichenbaum, “Correlates of hippocampal complex-spike cell activity in rats performing a nonspatial radial maze task,” *The Journal of Neuroscience*, vol. 14, pp. 6553–63, Nov. 1994.
- [119] A. K. Lee, I. D. Manns, B. Sakmann, and M. Brecht, “Whole-cell recordings in freely moving rats.,” *Neuron*, vol. 51, no. 4, pp. 399–407, 2006.
- [120] J. Epsztein, M. Brecht, and A. K. Lee, “Intracellular determinants of hippocampal CA1 place and silent cell activity in a novel environment.,” *Neuron*, vol. 70, no. 1, pp. 109–120, 2011.
- [121] G. Katona, G. Szalay, P. Maák, A. Kaszás, M. Veress, D. Hillier, B. Chiovini, E. S. Vizi, B. Roska, and B. Rózsa, “Fast two-photon in vivo imaging with three-dimensional random-access scanning in large tissue volumes,” *Nature Methods*, vol. 9, no. 2, pp. 201–8, 2012.
- [122] A. Cheng, J. T. Gonçalves, P. Golshani, K. Arisaka, and C. Portera-Cailliau, “Simultaneous two-photon calcium imaging at different depths with spatiotemporal multiplexing.,” *Nature Methods*, vol. 8, no. 2, pp. 139–142, 2011.
- [123] K. K. Ghosh, L. D. Burns, E. D. Cocker, A. Nimmerjahn, Y. Ziv, A. E. Gamal, and M. J. Schnitzer, “Miniaturized integration of a fluorescence microscope.,” *Nature Methods*, vol. 8, pp. 871–8, Jan. 2011.
- [124] M. T. Myaing, D. J. MacDonald, and X. Li, “Fiber-optic scanning two-photon fluorescence endoscope.,” *Optics letters*, vol. 31, pp. 1076–8, Apr. 2006.
- [125] W. Göbel, J. N. D. Kerr, A. Nimmerjahn, and F. Helmchen, “Miniaturized two-photon microscope based on a flexible coherent fiber bundle and a gradient-index objective.,” *Optics letters*, vol. 29, pp. 2521–3, Nov. 2004.
- [126] Y. Ziv, L. D. Burns, E. D. Cocker, E. O. Hamel, K. K. Ghosh, L. J. Kitch, A. E. Gamal, and M. J. Schnitzer, “Long-term dynamics of CA1 hippocampal place codes.,” *Nature Neuroscience*, vol. 16, pp. 264–6, Mar. 2013.
- [127] J. R. Gray, V. Pawlowski, and M. A. Willis, “A method for recording behavior and multineuronal CNS activity from tethered insects flying in virtual space.,” *Journal of Neuroscience Methods*, vol. 120, no. 2, pp. 211–223, 2002.
- [128] M. Dill, R. Wolf, and M. Heisenberg, “Visual pattern recognition in *Drosophila* involves retinotopic matching.,” *Nature*, vol. 365, no. 6448, pp. 751–753, 1993.
- [129] K. A. Leighty and D. M. Fragaszy, “Primates in cyberspace: using interactive computer tasks to study perception and action in nonhuman animals.,” *Animal cognition*, vol. 6, pp. 137–9, Sept. 2003.

- [130] E. A. Gaffan and M. J. Eacott, “Spatial memory impairment in rats with fornix transection is not accompanied by a simple encoding deficit for directions of objects in visual space.,” *Behavioral Neuroscience*, vol. 111, no. 5, pp. 937–954, 1997.
- [131] H.-Y. Lee, M.-D. Kuo, T.-C. Chang, Y.-S. Ou-Yang, and J.-J. J. Chen, “Development of Virtual Reality Environment for Tracking Rat Behavior,” *Journal of Medical and Biological Engineering*, vol. 27, pp. 71–78, June 2007.
- [132] C. Hölscher, A. Schnee, H. Dahmen, L. Setia, and H. A. Mallot, “Rats are able to navigate in virtual environments.,” *Journal of Experimental Biology*, vol. 208, no. Pt 3, pp. 561–569, 2005.
- [133] D. Dombeck, C. Harvey, and L. Tian, “Functional imaging of hippocampal place cells at cellular resolution during virtual navigation,” *Nature Neuroscience*, vol. 13, no. 11, pp. 1433–1440, 2010.
- [134] J. K. Chapin and C. S. Lin, “Mapping the body representation in the SI cortex of anesthetized and awake rats.,” *Journal of Comparative Neurology*, vol. 229, no. 2, pp. 199–213, 1984.
- [135] M. C. Stüttgen, J. Rüter, and C. Schwarz, “Two psychophysical channels of whisker deflection in rats align with two neuronal classes of primary afferents.,” *Journal of Neuroscience*, vol. 26, no. 30, pp. 7933–7941, 2006.
- [136] M. C. Stüttgen, S. Kullmann, and C. Schwarz, “Responses of rat trigeminal ganglion neurons to longitudinal whisker stimulation.,” *Journal of Neurophysiology*, vol. 100, no. 4, pp. 1879–1884, 2008.
- [137] M. M. La Vail, “Survival of some photoreceptor cells in albino rats following long-term exposure to continuous light.,” *Investigative Ophthalmology*, vol. 15, no. 1, pp. 64–70, 1976.
- [138] G. H. Jacobs, G. A. Williams, and J. A. Fenwick, “Influence of cone pigment coexpression on spectral sensitivity and color vision in the mouse.,” *Vision Research*, vol. 44, no. 14, pp. 1615–22, 2004.
- [139] A. Hughes, “A schematic eye for the rat,” *Vision Research*, vol. 19, pp. 569–588, Jan. 1979.
- [140] C. R. Legg and S. Lambert, “Distance estimation in the hooded rat: experimental evidence for the role of motion cues.,” *Behavioural Brain Research*, vol. 41, no. 1, pp. 11–20, 1990.
- [141] D. Green, M. Powers, and M. S. Banks, “Depth of focus, eye size and visual acuity,” *Neuroscience*, vol. 20, no. 10, pp. 52–52, 1979.
- [142] P. Dean, “Visual acuity in hooded rats: effects of superior collicular or posterior neocortical lesions.,” *Brain Research*, vol. 156, no. 1, pp. 17–31, 1978.

- [143] R. R. Fay, “Comparative psychoacoustics.,” *Hearing Research*, vol. 34, no. 3, pp. 295–305, 1988.
- [144] D. Warfield, “The study of hearing in animals,” *Methods of Animal Experimentation*, vol. 4, pp. 43–143, 1973.
- [145] R. J. Blanchard, D. C. Blanchard, R. Agullana, and S. M. Weiss, “Twenty-two kHz alarm cries to presentation of a predator, by laboratory rats living in visible burrow systems.,” *Physiology & Behavior*, vol. 50, no. 5, pp. 967–972, 1991.
- [146] V. Cuomo, R. Cagiano, M. A. De Salvia, M. A. Maselli, G. Renna, and G. Racagni, “Ultrasonic vocalization in response to unavoidable aversive stimuli in rats: effects of benzodiazepines.,” *Life Sciences*, vol. 43, no. 6, pp. 485–491, 1988.
- [147] T. Tonoue, Y. Ashida, H. Makino, and H. Hata, “Inhibition of shock-elicited ultrasonic vocalization by opioid peptides in the rat: a psychotropic effect.,” *Psychoneuroendocrinology*, vol. 11, no. 2, pp. 177–184, 1986.
- [148] E. A. Antoniadis and R. J. McDonald, “Discriminative fear conditioning to context expressed by multiple measures of fear in the rat.,” *Behavioural Brain Research*, vol. 101, no. 1, pp. 1–13, 1999.
- [149] D. A. Thomas, L. K. Takahashi, and R. J. Barfield, “Analysis of ultrasonic vocalizations emitted by intruders during aggressive encounters among rats (*Rattus norvegicus*).,” *Journal of Comparative Psychology*, vol. 97, no. 3, pp. 201–206, 1983.
- [150] S. M. Brudzynski and D. Ociepa, “Ultrasonic vocalization of laboratory rats in response to handling and touch.,” *Physiology & Behavior*, vol. 52, no. 4, pp. 655–660, 1992.
- [151] J. T. Allin and E. M. Banks, “Functional aspects of ultrasound production by infant albino rats (*Rattus norvegicus*).,” *Animal Behaviour*, vol. 20, no. 1, pp. 175–185, 1972.
- [152] S. E. Carden and M. A. Hofer, “Effect of a social companion on the ultrasonic vocalizations and contact responses of 3-day-old rat pups.,” *Behavioral Neuroscience*, vol. 106, no. 2, pp. 421–426, 1992.
- [153] B. Knutson, J. Burgdorf, and J. Panksepp, “Anticipation of play elicits high-frequency ultrasonic vocalizations in young rats.,” *Journal of Comparative Psychology*, vol. 112, no. 1, pp. 65–73, 1998.
- [154] J. Burgdorf, B. Knutson, and J. Panksepp, “Anticipation of rewarding electrical brain stimulation evokes ultrasonic vocalization in rats.,” *Behavioral Neuroscience*, vol. 114, no. 2, pp. 320–327, 2000.
- [155] P. M. Hofman, J. G. Van Riswick, and A. J. Van Opstal, “Relearning sound localization with new ears.,” *Nature Neuroscience*, vol. 1, no. 5, pp. 417–421, 1998.

- [156] J. C. Makous and J. C. Middlebrooks, “Two-dimensional sound localization by human listeners.,” *Journal of the Acoustical Society of America*, vol. 87, no. 5, pp. 2188–2200, 1990.
- [157] H. E. Heffner and R. S. Heffner, “Sound localization in wild Norway rats (*Rattus norvegicus*).,” *Hearing Research*, vol. 19, no. 2, pp. 151–155, 1985.
- [158] G. L. Kavanagh and J. B. Kelly, “Midline and lateral field sound localization in the albino rat (*Rattus norvegicus*).,” *Behavioral Neuroscience*, vol. 100, no. 2, pp. 200–205, 1986.
- [159] N. Greene, “Environment Mapping and Other Applications of World Projections,” 1986.
- [160] A. Hayar, J. L. Bryant, J. D. Boughter, and D. H. Heck, “A low-cost solution to measure mouse licking in an electrophysiological setup with a standard analog-to-digital converter.,” *Journal of Neuroscience Methods*, vol. 153, no. 2, pp. 203–207, 2006.
- [161] R. Morris, “Developments of a water-maze procedure for studying spatial learning in the rat,” *Journal of Neuroscience Methods*, vol. 11, no. 1, pp. 47–60, 1984.
- [162] R. J. Sutherland and R. H. Dyck, “Place navigation by rats in a swimming pool,” *Canadian Journal of Psychology*, vol. 38, p. 322, 1984.
- [163] W. Truccolo, U. T. Eden, M. R. Fellows, J. P. Donoghue, and E. N. Brown, “A point process framework for relating neural spiking activity to spiking history, neural ensemble, and extrinsic covariate effects.,” *Journal of Neurophysiology*, vol. 93, no. 2, pp. 1074–1089, 2005.
- [164] G. Schwarz, “Estimating the Dimension of a Model,” *The Annals of Statistics*, vol. 6, pp. 461–464, Mar. 1978.
- [165] E. N. Brown, R. Barbieri, V. Ventura, R. E. Kass, and L. M. Frank, “The time-rescaling theorem and its application to neural spike train data analysis.,” *Neural Computation*, vol. 14, no. 2, pp. 325–346, 2002.
- [166] R. H. Haslinger, E. N. Brown, and G. Pipa, “Discrete Time Rescaling Theorem: Determining Goodness of Fit for Discrete Time Statistical Models of Neural Spiking,” *Neural Computation*, vol. 22, pp. 2477–2506, Oct. 2010.
- [167] B. Silverman, *Density estimation for statistics and data analysis*. London: Chapman & Hall, 1998.
- [168] E. Resnik, J. M. McFarland, R. Sprengel, B. Sakmann, and M. R. Mehta, “The effects of GluA1 deletion on the hippocampal population code for position.,” *The Journal of Neuroscience*, vol. 32, pp. 8952–68, June 2012.

- [169] K. Mizuseki, S. Royer, K. Diba, and G. Buzsáki, “Activity dynamics and behavioral correlates of CA3 and CA1 hippocampal pyramidal neurons,” *Hippocampus*, vol. 22, no. 8, pp. 1659–1680, 2012.
- [170] J. H. Zar, *Biostatistical Analysis*, vol. 4th. Prentice Hall, 1999.
- [171] D. P. Nguyen, M. A. Wilson, E. N. Brown, and R. Barbieri, “Measuring instantaneous frequency of local field potential oscillations using the Kalman smoother.,” *Journal of Neuroscience Methods*, vol. 184, pp. 365–74, Nov. 2009.
- [172] N. A. Russell, A. Horii, P. F. Smith, C. L. Darlington, and D. K. Bilkey, “Lesions of the vestibular system disrupt hippocampal theta rhythm in the rat.,” *Journal of Neurophysiology*, vol. 96, pp. 4–14, July 2006.
- [173] N. Burgess, “Grid cells and theta as oscillatory interference: theory and predictions,” *Hippocampus*, vol. 18, no. 12, pp. 1157–1174, 2008.
- [174] M. Hasselmo, L. Giocomo, and E. Zilli, “Grid cell firing may arise from interference of theta frequency membrane potential oscillations in single neurons,” *Hippocampus*, vol. 17, no. 12, pp. 1252–1271, 2007.
- [175] H. Blair, A. Welday, and K. Zhang, “Scale-invariant memory representations emerge from moire interference between grid fields that produce theta oscillations: a computational model,” *The Journal of Neuroscience*, vol. 27, no. 12, pp. 3211–3229, 2007.
- [176] K. Jezek, E. J. Henriksen, A. Treves, E. I. Moser, and M.-B. Moser, “Theta-paced flickering between place-cell maps in the hippocampus,” *Nature*, vol. 478, no. 7368, pp. 246–249, 2011.
- [177] E. Hellinger, “Neue begründung der theorie quadratischer formen von unendlichvielen veränderlichen.,” *Journal für die reine und angewandte Mathematik*, vol. 136, pp. 210–271, 1909.
- [178] C. Domnisoru, A. A. Kinkhabwala, and D. W. Tank, “Membrane potential dynamics of grid cells.,” *Nature*, vol. 495, pp. 199–204, Feb. 2013.
- [179] C. Schmidt-Hieber and M. Häusser, “Cellular mechanisms of spatial navigation in the medial entorhinal cortex.,” *Nature neuroscience*, vol. 16, pp. 325–31, Mar. 2013.
- [180] D. A. Dombeck, C. D. Harvey, L. Tian, L. L. Looger, and D. W. Tank, “Functional imaging of hippocampal place cells at cellular resolution during virtual navigation.,” *Nature neuroscience*, vol. 13, pp. 1433–40, Nov. 2010.
- [181] G. Chen, J. A. King, N. Burgess, and J. O’Keefe, “How vision and movement combine in the hippocampal place code.,” *Proceedings of the National Academy of Sciences of the United States of America*, vol. 110, pp. 378–83, Jan. 2013.

- [182] G. Iurilli, D. Ghezzi, U. Olcese, and G. Lassi, “Sound-driven synaptic inhibition in primary visual cortex,” *Neuron*, vol. 73, pp. 814–828, Feb. 2012.
- [183] S. Deshmukh and J. Knierim, “Representation of non-spatial and spatial information in the lateral entorhinal cortex,” *Frontiers in behavioral neuroscience*, vol. 5, p. 69, Jan. 2011.
- [184] T. T. G. Hahn, J. M. McFarland, S. Berberich, B. Sakmann, and M. R. Mehta, “Spontaneous persistent activity in entorhinal cortex modulates cortico-hippocampal interaction in vivo,” *Nature Neuroscience*, Oct. 2012.
- [185] T. Hahn, B. Sakmann, and M. Mehta, “Phase-locking of hippocampal interneurons’ membrane potential to neocortical up-down states,” *Nature Neuroscience*, vol. 9, no. 11, pp. 1359–1361, 2006.
- [186] K. Chung, J. Wallace, S.-Y. Kim, S. Kalyanasundaram, A. S. Andalman, T. J. Davidson, J. J. Mirzabekov, K. A. Zalocusky, J. Mattis, A. K. Denisin, S. Pak, H. Bernstein, C. Ramakrishnan, L. Grose, V. Gradinaru, and K. Deisseroth, “Structural and molecular interrogation of intact biological systems,” *Nature*, vol. advance on, Apr. 2013.